Technische Universität München
Ingenieurfakultät Bau Geo Umwelt
Lehrstuhl für Astronomische und Physikalische Geodäsie

SAR Imaging Geodesy – Towards Absolute Coordinates with Centimeter Accuracy

Christoph Gisinger

Vollständiger Abdruck der von der Ingenieurfakultät Bau Geo Umwelt der Technischen Universität München zur Erlangung des akademischen Grades eines

Doktor-Ingenieurs (Dr.-Ing)

genehmigten Dissertation.

Vorsitzender:	Prof. Dr.rer.nat. Thomas Kolbe
Prüfer der Dissertation:	1. Prof. Dr.techn. Roland Pail
	2. Hon.-Prof. Dr.rer.nat. Michael Eineder
	3. Prof. Dr.-Ing. Uwe Sörgel, Universität Stuttgart

Die Dissertation wurde am 14.02.2019 bei der Technischen Universität München eingereicht und durch die Ingenieurfakultät Bau Geo Umwelt am 03.05.2019 angenommen.

"Sie wissen, dass ich langsam schreibe, allein dies kommt hauptsächlich daher, weil ich mir nie anders gefallen kann, als wenn in kleinem Raum möglichst viel ist, und kurz zu schreiben viel mehr Zeit kostet als lang"

("You know that I write slowly. This is chiefly because I am never satisfied until I have said as much as possible in a few words, and writing briefly takes far more time than writing at length.")

Carl Friedrich Gauß, 1833, Brief an H.C. Schumacher

"At ubi materia, ibi Geometria."

("Where there is matter, there is geometry.")

Johannes Kepler, 1602, De fundamentis astrologiae certioribus

"Insofern sich die Sätze der Mathematik auf die Wirklichkeit beziehen, sind sie nicht sicher, und insofern sie sicher sind, beziehen sie sich nicht auf die Wirklichkeit"

("As far as the laws of mathematics refer to reality, they are not certain; and as far as they are certain, they do not refer to reality.")

Albert Einstein, 1921, Geometrie und Erfahrung

Zusammenfassung

Weltraumgestütztes Synthetic Aperture Radar (SAR) besitzt viele Gemeinsamkeiten mit den etablierten geodätischen Verfahren Global Navigation Satellite System (GNSS) und Satellite Laser Ranging (SLR), wodurch prinzipiell Geodäsie mit Hilfe von SAR-Bildern ermöglicht wird, beispielsweise für Anwendungen wie die genaue Positionierung von Punkten oder die Validierung der Bahnen der SAR-Satelliten. Die geometrische Qualität von SAR ist bereits aus der klassischen Radargrammetrie bekannt, jedoch wurde die Fähigkeit von SAR-Sensoren zur direkten Messung von Distanzen mit Genauigkeiten im Bereich von Zentimetern oder sogar Millimetern bisher nur wenig beachtet. Der Grund hierfür ist unter anderem die dazu notwendige ganzheitliche Systembeschreibung, welche die genaue Bahnbestimmung, die Eigenschaften der SAR-Hardware, die Aufnahmeprozedur verschiedener SAR-Modi, die Folgen der Bildberechnung mittels spektraler Methoden, die Störungen aus der Signalverzögerung in der Atmosphäre und der Geodynamik, sowie die geometrische Kalibrierung umfasst. Die erste Untersuchung eines SAR-Satelliten in diesem Detailgrad wird durch die stark wissenschaftlich getriebene Mission TerraSAR-X ermöglicht, welche Einblick in sämtliche genannte Aspekte bietet, und seit kurzem durch die Mission Sentinel-1, die von den mit TerraSAR-X gewonnen Erkenntnissen profitieren soll. Darüber hinaus benötigt die Systembeschreibung ein konsistentes Beobachtungsmodell für die verschiedenen Anwendungen, wodurch eine Beurteilung der Auswertung nach geodätischen Standards möglich ist.

Diese Arbeit basiert auf sechs Journal-Veröffentlichungen und dokumentiert die Beschreibung des Gesamtsystems SAR, welche mit TerraSAR-X entwickelt und in praktischen Experimenten getestet wurde. Die Tests erfolgten an den geodätischen Stationen Wettzell in Deutschland, Metsähovi in Finnland, und GARS O'Higgins in der Antarktis mit Hilfe der dort permanent installierten 0.7 und 1.5 m großen Corner Reflektoren (CRs), sowie mit dem Reflektor-Array in Queensland, Australien. Des Weiteren zeigen die Untersuchung für Sentinel-1 für das Array in Australien, wie die Methoden auf andere SAR-Missionen übertragen werden können. Die Auswertung nutzt als Beobachtungsmodell die Range-Doppler-Gleichungen in der Doppler-Null-Konfiguration. Die Lösung der Gleichungen erfolgt durch Linearisierung bezüglich der SAR-Beobachtungen Range und Azimut und der freien Parameter (Target-Koordinaten, Systemparameter) und anhand der Methode der *Kleinste-Quadrate-Ausgleichung nach Bedingungen*. Über die zusätzliche Schätzung der Varianzkomponenten der Beobachtungsgruppen liefert diese Lösung eine optimale Kombination der Messdaten, die sowohl die Analyse der Range- und Azimut-Beobachtungen als auch die absolute und differentielle Positionierung von Punktstreuern, zum Beispiel CRs, ermöglicht. Die *a priori* Korrektur der Messungen verwendet etablierte GNSS-Produkte, genauer die globalen Ionosphärenkarten und die gemessenen troposphärischen Zenitdelays einzelner GNSS-Empfänger, sowie die durch den International Terrestrial Reference Frame (ITRF) vorgegebenen geodynamischen Modelle. Die durch die Zeitgebung an Bord der SAR-Satelliten und durch die Methoden der Bildberechnung verursachten Artefakte werden entweder direkt bei der Generierung der Bilder (TerraSAR-X) oder nachträglich durch angepasste Korrekturen (Sentinel-1) reduziert.

Die Vergleiche von TerraSAR-X Messungen über einen Zeitraum von sechs Jahren mit den Referenzkoordinaten der Reflektoren zeigen eine Genauigkeit für die SAR-Messungen von 1.5 cm in Range und 2.0 cm in Azimut (1 Sigma, Einzelmessung), wenn das Gesamtsystem SAR modelliert wird und die ak-

tuell bestmöglichen Bahnlösungen der TerraSAR-X Mission verwendet werden. Die Analyse mit diesen experimentellen Bahnen zeigt eine Verbesserung von etwa 20 % in den SAR-Messungen gegenüber den mit den Bildern mitgelieferten Bahnen. Für die Sentinel-1 Messungen des Arrays in Australien ergibt sich eine Genauigkeit von 6 cm in Range und 26 cm in Azimut, wobei hier primär die Größe der Reflektoren in Relation zur Auflösung der Sentinel-1 Interferometric Wide Swath Standard-Produkte ein limitierender Faktor darstellt. Bei den Experimenten zur Positionierung, die mit TerraSAR-X durchgeführt wurden, ergibt die Validierung durch die terrestrische Referenzmessung eine Genauigkeit von 2-4 cm für SAR-Koordinaten. Die statistische Schätzung der Ungenauigkeiten bewegt sich bei einer Skalierung auf 95 % Konfidenzniveau in derselben Größenordnung. Zudem deuten weitere Experimente mit TerraSAR-X darauf hin, dass die Genauigkeit der Positionierung in Zukunft noch auf 1-2 cm verbessert werden kann, wenn spezielle Reflektoren oder aktive Transponder zur Kombination von SAR-Messungen von aufsteigenden und absteigenden Bahnen verwendet werden. Dies gilt auch für die differentielle Positionierung, welche die letzten noch verbleibenden Systematiken im SAR-System weiter reduziert beziehungsweise eliminiert. Zudem wurde gezeigt, dass das Verfahren auch für natürliche Punktstreuer funktioniert. Diese liefern in der Regel zwar weniger konsistente Messungen und damit eine um den Faktor 2-3 schlechtere Genauigkeit in der Positionierung, ermöglichen dafür aber die Auswertung einer Vielzahl von Punkten, was für viele Anwendungen von Interesse ist, zum Beispiel als Passpunkte für die Fusion und Geokodierung von Ergebnissen aus der SAR-Tomographie. Diese Ergebnisse und die vergleichende Diskussion zwischen SAR-Geodäsie, SLR und GNSS zeigen, dass absolute SAR-Messungen das Potential für ein eigenständiges globales geodätisches Beobachtungsverfahren haben, wenn die entwickelte Beschreibung des Gesamtsystems SAR angewendet wird. Speziell in Bezug auf die für lange Zeiträume ausgelegten SAR-Missionen wie Sentinel-1 ist dies von großem Interesse. Diese Möglichkeit sollte in Zukunft weiter untersucht werden.

Abstract

Spaceborne synthetic aperture radar (SAR) shares many similarities with the established space geodetic techniques of Global Navigation Satellite System (GNSS) and Satellite Laser Ranging (SLR). It offers the potential for SAR imaging geodesy in applications like precise point positioning or orbit analysis of the SAR satellites. The inherent geometric quality of SAR is well known in radargrammetric data processing, but the abilities of SAR sensors for centimeter or even millimeter level absolute ranging observations have not been fully exploited so far. The reason for this is the need of a comprehensive SAR systems approach, which addresses precise orbit determination, the properties of SAR hardware implementation, the acquisition process of different SAR modes, the implications of image processing by spectral methods, the perturbations of atmospheric path delays and geodynamic deformation, and the geometric calibration. The first investigation of a SAR satellite at this level of detail has become possible with the scientifically driven TerraSAR-X mission that provides access to all the system components, and more recently with the Sentinel-1 mission which aims to benefit from the lessons learned with TerraSAR-X. Moreover, the SAR systems approach requires a consistent observation model for the different applications that allows the assessment of the solution quality according to geodetic standards.

This work is based on six journal publications and presents the unified systems approach that was developed with TerraSAR-X. It was tested in experiments with the permanent corner reflectors (CRs) of 0.7 and 1.5 m dimension installed at the geodetic observatories of Wettzell, Germany, of Metsähovi, Finland, and of GARS O'Higgins in Antarctica, and with the reflector array located in Queensland, Australia. In addition, the results with Sentinel-1 for the Australian array show the transfer of the approach to other SAR missions. The processing uses the range-Doppler model in zero-Doppler configuration, which was rigorously linearized for the radar observations range and azimuth and the unknown parameters (target coordinates, system parameters) to match the least squares method *adjustment with conditions*. Along with variance component estimation for the observations, the processing determines an optimum data combination, which enables both the range and azimuth observation analysis and the absolute and differential positioning of point targets like the CRs. The *a priori* observation correction uses the well-defined GNSS products, i.e. global ionospheric maps and zenith tropospheric delays of single GNSS receivers, or tropospheric delays from weather model integration, and the geodynamic models associated with the International Terrestrial Reference Frame (ITRF). The artifacts related to SAR onboard timing hardware and image processing are either removed during image product generation (TerraSAR-X) or by dedicated post-processing corrections (Sentinel-1).

The comparisons of the CR reference coordinates with TerraSAR-X data for six years reveals the accuracy of the SAR observations with 1.5 cm in range and 2.0 cm in azimuth (1 sigma, single observation) when using the developed observation model and the best TerraSAR-X orbit solution presently available. The analysis also shows an improvement of approximately 20 % for this best experimental orbit solution over the precise science orbit annotated to the image products. For Sentinel-1, the numbers obtained at the Australian array read 6 cm in range and 26 cm in azimuth, which are mainly limited by the size of the CRs versus the spatial resolution of the Sentinel-1 Interferometric Wide Swath standard product. In terms of the positioning experiments carried out with TerraSAR-X, the validation with

the local ties confirm the accuracy of the SAR positions with 2-4 cm. The estimated positioning errors are at the same orders of magnitude when scaled to 95 % confidence level. Further experiments with TerraSAR-X indicate that improvements in the positioning accuracy down to 1-2 cm become attainable with reflectors or active SAR transponders that join ascending and descending pass geometries and with the differential approach that further reduces small remaining system biases. Finally, it was also demonstrated that the positioning is readily possible for opportunistic point scatters, which provide less consistent observations and have an estimated positioning accuracy of approximately 2-3 times worse than a CR. However, they give access to a large number of coordinate observations for various applications, such as ground control points to fuse and geocode the results of phase-based SAR tomography. These results together with the comparative discussion of SAR imaging geodesy, SLR, and GNSS confirm that absolute SAR observations using the developed systems approach have considerable potential for a self-contained space geodetic technique. This is of particular interest for long-term SAR missions like Sentinel-1, and this possibility should be investigated further.

Preface and Reader's Guide

This paper-based dissertation comprises three first-author publications (P-I, P-II, P-III) and three additional co-author publications (P-IV, P-V, P-VI) containing supplementary material. The publications are:

P-I C. Gisinger, U. Balss, R. Pail, X. X. Zhu, S. Montazeri, S. Gernhardt, M. Eineder, (2015) "Precise Three-Dimensional Stereo Localization of Corner Reflectors and Persistent Scatterers With TerraSAR-X", in: *IEEE Transactions on Geoscience and Remote Sensing*, vol. 53, no. 4, pp. 1782–1802. doi: 10.1109/TGRS.2014.2348859

P-II C. Gisinger, M. Willberg, U. Balss, T. Klügel, S. Mähler, R. Pail, M. Eineder, (2017) "Differential geodetic stereo SAR with TerraSAR-X by exploiting small multi-directional radar reflectors", in: *Journal of Geodesy*, vol. 91, no. 1, pp. 53–67. doi: 10.1007/s00190-016-0937-2

P-III C. Gisinger, A. Schubert, H. Breit, M. Garthwaite, U. Balss, M. Willberg, D. Small, M. Eineder, N. Miranda, (2019) "In-Depth Verification of Sentinel-1 and TerraSAR-X Geolocation Accuracy using the Australian Corner Reflector Array", in *IEEE Transactions on Geoscience and Remote Sensing*, accepted December 2019, in publication.

P-IV S. Hackel, C. Gisinger, U. Balss, M. Wermuth, O. Montenbruck, (2018) "Long-Term Validation of TerraSAR-X and TanDEM-X Orbit Solutions with Laser and Radar Measurements", in *Remote Sensing*, vol. 10, no. 5, pp. 1–20. doi: 10.3390/rs10050762

P-V U. Balss, C. Gisinger, M. Eineder, (2018) "Measurements on the Absolute 2-D and 3-D Localization Accuracy of TerraSAR-X", in *Remote Sensing*, vol. 10, no. 4, pp. 1–21. doi: 10.3390/rs10040656

P-VI X. X. Zhu, S. Montazeri, C. Gisinger, R. F. Hanssen, R. Bamler, (2016) "Geodetic SAR Tomography", in: *IEEE Transactions on Geoscience and Remote Sensing*, vol. 54, no. 1, pp. 18–35. doi: 10.1109/TGRS.2015.2448686

Throughout the text, these six papers are cited as P-I to P-VI, and dedicated elements like equations or figures are referred to in square brackets, for instance P-I [Fig. 2] or P-I [Eq. 3]. The details on the papers are given in chapter 5, which provides a short summary, the declaration of author's contributions, and the full-text digital copy of the paper as published in the journal.

The dissertation itself is composed of four chapters and is structured as follows:

The first chapter **Introduction** outlines the motivation and the scope of the research and discusses the dissertation in the context of existing literature on the subject of geodesy and SAR. In addition, the publications are presented describing their contributions to the research topic and the scientific questions addressed by the dissertation.

The second chapter **Methodology** provides a summary on SAR image formation and processing, mainly confined to the aspects concerning absolute SAR measurements. The major part of this chapter is devoted to the methodology of 2-D and 3-D absolute SAR processing, which comprises the steps of the solution with least squares parameter estimation and presents a comprehensive view of the methods applied in the experiments reported in the papers. The chapter also

contains short overviews on the SAR missions TerraSAR-X and Sentinel-1, which were used in the practical experiments discussed in this thesis.

The third chapter **Discussion and Analysis** reviews the findings of the publications in the context of the established geodetic methods SLR and GNSS. The chapter also deals with the future direction of the geodetic SAR method and its potential extension to new applications.

The fourth chapter **Summary and Future Directions** summarizes the dissertation and provides a concluding outlook.

List of Acronyms

CODE Center for Orbit Determination in Europe

CoM center-of-mass

CR corner reflector

DLR German Aerospace Center

DOP dilution of precision

DORIS Doppler Orbitography and Radiopositioning Integrated by Satellite

DEM digital elevation model

ECEF Earth-centered, Earth-fixed

ECMWF European Centre for Medium-Range Weather Forecasts

ECSF Earth-centered space-fixed

ESA European Space Agency

FM frequency modulation

GA Geoscience Australia

GARS German Antarctic Receiving Station

GNSS Global Navigation Satellite System

GPS Global Positioning System

GCP ground control point

ICRF International Celestial Reference Frame

IERS International Earth Rotation and Reference Systems Service

IGS International GNSS Service

ILRS International Laser Ranging Service

IPF Instrument Processing Facility

IRI international reference ionosphere

ITRF International Terrestrial Reference Frame

IW Interferometric Wide Swath

LOS line of sight

POD precise orbit determination

PPP precise point positioning

PPS pulse per second

PRF pulse repetition frequency

PRI pulse repetition interval

PS persistent scatterer

PSI Persistent Scatterer Interferometry

PSO Precise Science Orbit

PTA point target analysis

RCS radar cross section

RDOD reduced dynamic orbit determination

RMS root mean square

S1A Sentinel-1A

S1B Sentinel-1B

SAR synthetic aperture radar

SET solid Earth tides

SCR signal to clutter ratio

SIR Shuttle Imaging Radar

SLR Satellite Laser Ranging

SRTM Shuttle Radar Topography Mission

SSC single look slant range complex

TDX TanDEM-X

TEC total electron content

TMSP TerraSAR-X Multimode SAR Processor

TOPS Terrain Observation with Progressive Scan

TUM Technical University of Munich

TSX TerraSAR-X

USO ultra stable oscillator

UTC Coordinated Universal Time

UZH University of Zurich

VCE variance component estimation

VLBI Very Long Baseline Interferometry

VMF Vienna Mapping Function

Contents

1 Introduction

1.1 Synthetic Aperture Radar and Geodesy

The main objective of this thesis is the theoretical and experimental analysis of spaceborne synthetic aperture radar (SAR) to determine absolute geodetic coordinates from radar remote sensing. In order to achieve this goal, two different elements had to be brought together: the mathematical methods for effectively solving the geometric positioning problem in 3-D as well as the correction and calibration of the SAR observations. The latter comprise the sensor specific effects, which are related to SAR image formation and processing, and the external errors, which originate from the Earth's atmosphere and the solid Earth tidal deformations. Conceptually, such a systems approach is already well established for space geodetic techniques like Very Long Baseline Interferometry (VLBI) (Schuh and Böhm, 2013), Satellite Laser Ranging (SLR) (Combrinck, 2010), and Global Navigation Satellite System (GNSS) (Teunissen and Montenbruck, 2017). For these techniques, common standards for data reduction have been adopted in the course of the International Terrestrial Reference Frame (ITRF) determination. The modelling of observations and orbits is rigorously embedded in the 3-D framework of the ITRF (Petit and Luzum, 2010; Altamimi et al., 2016).

For SAR, however, a similar systems approach to improve the retrieval of accurate 3-D coordinates has not been established so far. A possible explanation for this could be that in the field of SAR the required elements (Fig. 1.1) are spread across different communities. On the one hand, the geometrical methods rather belong to the scientific application side and are closely related to radargrammetry, i.e. the discipline of extracting geometric information from radar remote sensing imagery (Leberl, 1990). Beyond the pure radargrammetric approach, the global geometric methods and correction standards are driven by space geodesy and the computation of the reference frames (Petit and Luzum, 2010). On the other hand, the calibration of the SAR payloads, the SAR data processing, and the orbit determination are commonly within the domain of the SAR satellite providers, where these tasks are often performed by engineers with backgrounds in electrical engineering or telecommunications. The different disciplines have their own priorities, standards and conventions, and bridging these two worlds was one of the challenges that had to be overcome to accomplish the aforementioned objective, as the proposed systems approach requires detailed knowledge of many aspects of a SAR mission.

The TerraSAR-X mission offered a unique opportunity, because the operational elements of this mission, i.e. the orbit determination, the monitoring and calibration of the SAR payload, and the processing of the SAR images, are all part of a single comprehensive ground segment, which is developed and maintained by the German Aerospace Center (DLR) in Oberpfaffenhofen, Germany (Werninghaus and Buckreuss, 2010; Breit et al., 2010). Even more important, modifications of these elements and SAR experiments are an inherent part of the TerraSAR-X mission concept. The investigation of the TerraSAR-X radar payload and the SAR images for their limits in geometrical quality (see Eineder et al., 2011; Schubert et al., 2012a) marked the starting point for the work presented in the thesis. Only this successful investigation of the SAR as a system with its geometrical and physical aspects ultimately paved the way for SAR imaging geodesy and the retrieval of 3-D coordinates.

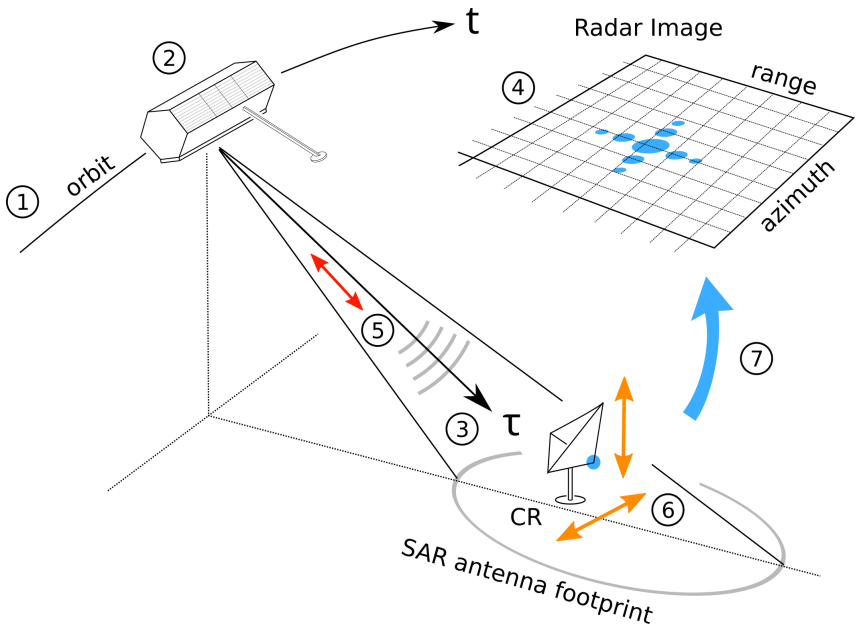

Fig. 1.1: SAR imaging geometry and elements of the SAR systems approach: (1) precise orbit determination, (2) SAR payload hardware, (3) image acquisition process, (4) image generation with SAR processor, (5) atmospheric path delays, (6) terrestrial reference frame and geodynamic displacements, and (7) observation equation for range and azimuth of a CR point target.

1.2 Background and Existing Work

In the introduction of his unique textbook on radargrammetry and geodesy, F.W. Leberl retraces the history of extracting geometric information from radar imagery (Leberl, 1990). He reports that this idea was already present in the very early beginnings of radar imaging technology around 1950. Operated in side-looking fashion and exploiting the synthetic aperture method, the radar payload generates images by active transmission and reception of microwave pulses. The SAR images appear to be similar to conventional optical grayscale images, but the gray values are arranged according to the Doppler in along-track direction and the signal travel time in the cross-track direction (Fig. 1.1). Therefore, the pixels effectively encode the timeline of the sensor trajectory, also termed slow time t or azimuth, and the slant distances to the ground, also termed fast time τ or range (Curlander, 1982; Leberl, 1990). Radar became a valuable tool for weather and daytime independent image gathering. For scientific Earth observation it was first restricted to airborne platforms (Leberl, 1990), but the situation changed with the launch of the Seasat satellite in 1978 (Stewart, 1988). For the first time, this satellite carried a side-looking SAR imaging payload for Earth observation with an average resolution of 25 m for scientific applications (Jordan, 1980).

The geometric possibilities of Seasat's time and distance coded radar images were immediately recognized, as they enabled a direct geocoding for the images when coupled with an *a priori* defined reference model of the Earth surface, for instance a reference ellipsoid (Curlander, 1982). However, for Seasat's single image geometric quality - today we would call this SAR geolocation - Leberl names $\pm$300 m when using one to two supportive ground control points (GCPs). No meaningful results could be achieved when using the data as it is, as recounted in Leberl (1990). He had to conclude with some frustration that the potential is certainly there, but without precise azimuth and range reference information and the support of an accurate orbit, the fairly good resolution of Seasat cannot be fully exploited (Leberl, 1990). Curlander (1982) was more successful in using the Seasat data without the need of control points and reported approximately 200 m geolocation accuracy when employing a fully digital processing chain along with the orbit ephemeris data. Because of these results, it is obvious why Curlander (1982) emphasizes the need for accurate orbit determination and tighter requirements for the on-board timing synchronization, and why Leberl (1990) names the signal propagation effects of the atmosphere negligible and advocates methods with reliable GCPs.

In terms of 3-D reconstruction, the two-step method of first refining the radargrammetric stereo model with GCPs and subsequently resolving the 3-D coordinates for the co-registered image pair was widely applied in these early days of spaceborne SAR (Leberl, 1990). The stereo results of different groups for the Seasat mission and the Shuttle Imaging Radar (SIR) experiments are summarized in Leberl (1990) and Dowman (1992), who report 3-D accuracies on the order of 50-100 m. It is interesting to note that the rigorous geometrical approach for directly intersecting the observation of point targets was in principle already laid out and documented at that time (Kobrick et al., 1986; Leberl, 1990). However, it received no detailed attention because of the limitations discussed above and was not extended beyond the standard stereo case consisting of two SAR images. Furthermore, the focus remained on the reconstruction of entire digital elevation models (DEMs) at the scale of the image pixels rather than accurate coordinate retrieval by exploiting the sub-pixel level precision of SAR. The direct computation of DEMs from SAR stereo configurations benefited from the advance in orbit computation and image resolution. It is still carried out on local scales, in particular for mountainous terrain to avoid the unwrapping of the ambiguous phase required for the interferometric methods (e.g., Chen and Dowman, 2000; Toutin and Chénier, 2009; Raggam et al., 2010a; Dong et al., 2018). For global scale DEM generation the interferometric method (InSAR; Bamler and Hartl, 1998), became the dominant approach, see for example the Shuttle Radar Topography Mission (SRTM; Farr et al., 2007) or the TanDEM-X mission (Krieger et al., 2007). To extend interferometry to areas with low spatial coherence, e.g., urban areas, point-wise methods like Persistent Scatterer Interferometry (PSI) or TomoSAR were introduced (Ferretti et al., 2001; Zhu and Bamler, 2010; Crossetto et al., 2016). These SAR methods rely on strong persistent scatterers (PSs) to estimate the height above a given topography and line of sight (LOS) deformations from repeat pass phase differences. The strength of InSAR and PSI lies in the very high sensitivity to deformation, whereas conversion to absolute heights needs the resolution of the phase ambiguities (phase unwrapping) as well as geocoding and an external datum (Bamler and Hartl, 1998; Crossetto et al., 2016; Mahapatra et al., 2017). Even for strong scatterers like corner reflectors (CRs), the height accuracy is limited to 1-2 m by the spatial extent of the perpendicular baseline (Dheenathayalan et al., 2016). Therefore, the interferometric methods cannot be considered as absolute 3-D methods to generate independent coordinates with SAR in the sense of the space geodetic techniques, which require the usage of SAR range and azimuth observations across different pass geometries, i.e. large baselines.

Notable work on absolute SAR coordinates was published for the ERS-1 mission by Chen and Dowman (1996), and continued and refined later for the RADARSAT-1 mission (Chen and Dowman, 2001). For the latter, the coordinate accuracy remained at approximately 50 m, mainly due to the limited orbit accuracy but also because of the pair-wise data processing that did not take full advantage of the selected least squares approach. Progress was made with the launch of the next generation SAR missions, most notably TerraSAR-X (Werninghaus and Buckreuss, 2010) and Cosmo-SkyMed (Coletta et al., 2007). They offer high resolution image products (up to 0.25 x 0.6 m) and an overall improved system accuracy when using the products as provided. Three-dimensional positioning results validated with ground truth data within 0.5 to 1.5 m are presented for natural features like lamp poles and purposefully installed CRs, see Raggam et al. (2010b); Koppe et al. (2012) for TerraSAR-X and Nitti et al. (2016) for Cosmo-SkyMed. These publications are also interesting because instead of single image pairs they make use of small ensembles of up to ten images across different pass geometries. However, except for a short comment on the atmospheric perturbation in Nitti et al. (2016), all computations neglect the perturbations additionally contained in the SAR data, i.e. the interaction of the SAR signal with the atmosphere and the implications of the ITRF and the solid Earth deformation. Therefore, these results can be considered as indicators for the limit of a purely geometric processing approach. In order to advance SAR to the centimeter-level, a more refined observation modelling is required.

Tab. 1.1: Geolocation accuracy requirements and the experimentally determined results of different SAR missions. For constellation missions the launch date refers to the first spacecraft; requirement refers to the highest resolution slant range image product; the achieved result is the standard deviation without the bias, see details in text.

Sensor	Launch	Req.	Achieved	Sources
Seasat	1978		200 m	Curlander (1982)
ERS-1/2	1991		6 m	Mohr and Madsen (2001)
Envisat ASAR	2002	10 m	0.8 m	Kult (2012); Small et al. (2004)
ALOS-1	2006	100 m	10 m	Shimada et al. (2009)
RADARSAT-2	2007	15 m	0.5 m	MDA (2016); Chabot et al. (2015)
Cosmo SkyMed	2007	3.75 m	0.8 m	Calabrese et al. (2018); Nitti et al. (2015)
TerraSAR-X	2007	1 m	0.5 m	Fritz and Eineder (2013); Schwerdt et al. (2010)
Sentinel-1	2014	2.5 m	0.2 m	Bourbigot et al. (2015); Schubert et al. (2015)

SAR observation modelling of range and azimuth is closely linked to the direct geolocation capability. It was already mentioned in the beginning of this section that many of the important aspects for spaceborne SAR geolocation were discussed for the early results of the Seasat mission (Curlander, 1982). With the advancement of the SAR missions, many of the satellite providers recognized the importance of assigning accurate geographic coordinates to the images for rapid mapping and straightforward usage with additional geospatial data, e.g., road networks or optical images. The assessment of the geolocation quality of SAR sensors with respect to ground truth coordinates of features like cross roads, stable CRs or active transponders is part of the geometric sensor calibration. This calibration was updated and refined during the lifetime of the first generation of spaceborne SAR missions and is now generally performed during the commissioning phase. Table 1.1 presents a summary of the geolocation accuracy across several spaceborne SAR missions. The achieved values refer to the geolocation standard deviation without the mean bias, because after confirming the stability of the biases they are applied as geometric calibration constants to center the data. Note that in the case of independent range and azimuth assessments, only the azimuth results are listed in the table, because the azimuth represents the upper geolocation limit of the SAR system[1].

Geolocation capabilities were not yet among the list of requirements of Seasat or ERS-1/2, but the latter took advantage from the long mission lifetime and the altimetry payload that demanded the most precise orbit solutions to observe global sea level changes (Duchossois and Zobl, 1995). Unlike the early work on 3-D stereo processing using only image pairs, the geolocation analysis of ERS-1/2 was performed on a product-by-product basis with multiple images acquired across different locations, different SAR imaging modes, and longer time spans (Mohr and Madsen, 2001). The results of approximately 6 m for the azimuth observations point out the limitations to accurately establish the Coordinated Universal Time (UTC) for the SAR instrument. Apart from optimizations regarding the on-board timing and instrument parameters, the computation was solely performed based on geometric considerations. Considerable progress was made with the Envisat mission, which achieved a sub-meter accuracy in dedicated experiments for the first time (Small et al., 2004). Again benefiting from the multi-payload design including an altimeter and the advancements made in precise orbit determination (POD) (Louet, 2001), the geolocation analysis now used purposefully installed point targets (i.e. CRs), sub-pixel level processing by image oversampling, and the removal of the bistatic azimuth delay. This reduced the azimuth standard deviation from 1.8 m to 0.8 m. The range standard

[1]This is because the azimuth is less accurately observed due to the coarser azimuth image resolution and the implementation of the on-board timing, as discussed later in chapter 2.

deviation achieved with Envisat was even better (about 0.5 m, Small et al., 2004). These results illustrate the very high system quality of the Envisat ASAR payload and the ability of SAR to geolocate point targets with strong signal returns with an accuracy better than 1 m for images which have only a resolution of 9 x 6 m. Still the atmospheric path delay was not yet considered as a correction, which would have accounted for most of the 2 m bias observed in range.

The following missions with SAR as primary payload (ALOS-1 PALSAR, RADARSAT-2, COSMO SkyMed) began to define requirements on geolocation (see Table 1.1), but the relatively moderate numbers[1] affected the accuracy requirements of the orbit product and the absolute timing for the SAR payload on board the satellites. Therefore, orbit and timing became limiting factors in the experimental analyses of the geolocation quality of these missions (Shimada et al., 2009; Schubert et al., 2012b; Chabot et al., 2015; Nitti et al., 2015), especially after additionally considering the atmospheric path delay which became common practice with the launch of TerraSAR-X in 2007. In contrast to the contemporary SAR missions, the TerraSAR-X mission was designed for a high geolocation accuracy to match the 1 m resolution of the high-resolution spotlight mode (Werninghaus and Buckreuss, 2010). The mission payloads, the realization of the on-board timing, the computation of the science orbit product, and the SAR image processor were all implemented to meet this tight geometric requirement (Yoon et al., 2009; Breit et al., 2010). The geometric calibration of the mission confirmed that the requirement was readily achievable if a standard atmosphere is assumed and barometrically scaled with respect to topography (Schwerdt et al., 2010). Thus these simple estimates of atmospheric delays became part of the TerraSAR-X image products (Fritz and Eineder, 2013).

However, apart from ensuring a geolocation at the level of the image product, range and azimuth were not considered as observables themselves. Even though this possibility had already been partly demonstrated by Envisat ASAR and it was known from theory that for a perfectly modelled SAR payload the range and azimuth observation accuracy ultimately is only dependent on the signal return with respect to background clutter and the image resolution (Bamler and Eineder, 2005). From the perspective of a SAR satellite provider, there was a certain need to develop an accurate SAR observation model for the range and azimuth observations to meet the geolocation requirement. Once the requirement was confirmed to be achieved, there was no immediate demand to further advance the modelling. Nevertheless, the work on TerraSAR-X continued on an experimental basis and because of the already demanding initial design, the mission eventually became the benchmark for SAR geolocation. Removing the path delays in range by applying a more precise pass-by-pass modelling of the atmosphere reduced the range and azimuth standard deviations down to 5-15 cm (Schubert et al., 2010). The remaining biases of up to 0.5 m were mainly attributed to differences in the reference frames of the SAR data and the surveyed ground truth, which could be confirmed by additional investigations (Schubert et al., 2012a). This was the point were SAR geolocation touched upon the subjects of space geodesy, and the TerraSAR-X geolocation analysis began to apply modelling techniques following the concepts of GNSS, which for the first time in SAR also included the deformations of the solid Earth tides (Eineder et al., 2011; Cong et al., 2012). The outcome was the removal of most of the remaining biases and an experimental geolocation accuracy of 5 cm with TerraSAR-X stripmap data, which was referred to as SAR imaging geodesy. Further assessment of these results by a mutual project of DLR and Technical University of Munich (TUM), which led to the first installation of a tightly controlled reference CR at Wettzell Geodetic Observatory (Balss et al., 2013), finally triggered the research addressed in this thesis.

The Sentinel-1 mission has transformed SAR into routine global monitoring with free and open data access (Torres et al., 2012; CSC Mission Management Team, 2018). The mission's geolocation requirement of 2.5 m demanded an implementation level comparable to TerraSAR-X, and the commissioning

[1] Note that the initially specified value for COSMO SkyMed was 15 m (ASI, 2007)

phase geolocation assessment managed to achieve an accuracy of 0.2 m by including precise atmospheric corrections and the solid Earth tides (Schubert et al., 2015). However, inconsistencies with the calibration biases and systematic distortion in the geolocation residuals were discovered in the subsequent analysis of the lower resolution Sentinel-1 standard product (Schubert et al., 2017). The investigations of these inconsistencies became part of this thesis, because they had to be addressed in order to transfer the developed methods and align Sentinel-1 with TerraSAR-X. The solutions found for these artefacts made important contributions to the Sentinel-1 SAR observation model and emphasized several crucial steps of SAR image processing that are already considered during the TerraSAR-X product generation.

In summary, substantial research on geolocation and SAR calibration was carried out in this thesis to achieve the final goal, i.e. the determination of accurate SAR-based 3-D coordinates. This led to the successful combination of geodetic standards with radargrammetric concepts and to the definition of a comprehensive SAR systems approach.

1.3 Discussion of Publications and Thesis Objectives

The systems approach for SAR and the evaluation of its possibility as a geodetic technique can be decomposed into several research aspects, which were addressed by the six publications P-I to P-VI. The publications are organized in Fig. 1.2 with respect to their contributions to the overall approach.

On a large scale they can be distinguished whether their focus remains on the SAR slant range and azimuth observations (2-D) or if the SAR observations are combined to perform 3-D positioning. The horizontal dimensions of the boxes indicate whether the publication is considered as a contribution to the development of the methodology or is oriented towards application, or both. The publications P-I, P-II, P-III and P-V introduce different aspects of SAR imaging geodesy and the observation model. Moreover, they include examples and results addressing potential applications (P-I, P-III), while P-IV and P-VI mainly deal with applications. The content of the publications can be briefly summarized as follows (for further details, see chapter 5):

P-I C. Gisinger, U. Balss, R. Pail, X. X. Zhu, S. Montazeri, S. Gernhardt, M. Eineder, (2015) "Precise Three-Dimensional Stereo Localization of Corner Reflectors and Persistent Scatterers With TerraSAR-X", in: *IEEE Trans. Geosci. Remote Sens.*, 53(4), pp. 1782–1802.

The publication introduces the absolute 3-D positioning method along with the observation modelling to generate the unbiased observation inputs for the positioning. The development is motivated by the experience gained with TerraSAR-X during the data analysis (see previous section 1.2). The core part is the least squares positioning methodology, which is related to the radargrammetric methods but required considerable modifications to allow direct positioning with given orbits and the inclusion of advanced statistical techniques like variance component estimation. Moreover, the observation model can be readily adapted to other needs like the geometric calibration. The method is verified with TerraSAR-X using more than 150 image acquisitions of the four permanent CRs installed at the geodetic observatories Wettzell and Metsähovi, and at the German Antarctic Receiving Station (GARS) O'Higgins. The consistent combination of SAR data at observation level is demonstrated by solving various geometric configurations ranging from single repeat pass geometries to multiple ascending and descending pass geometries. Precision estimates (confidence ellipsoids) form an integral part of the results and allow to assess the solution quality. Additional comparisons with the CR reference coordinates verify the positioning accuracy with better

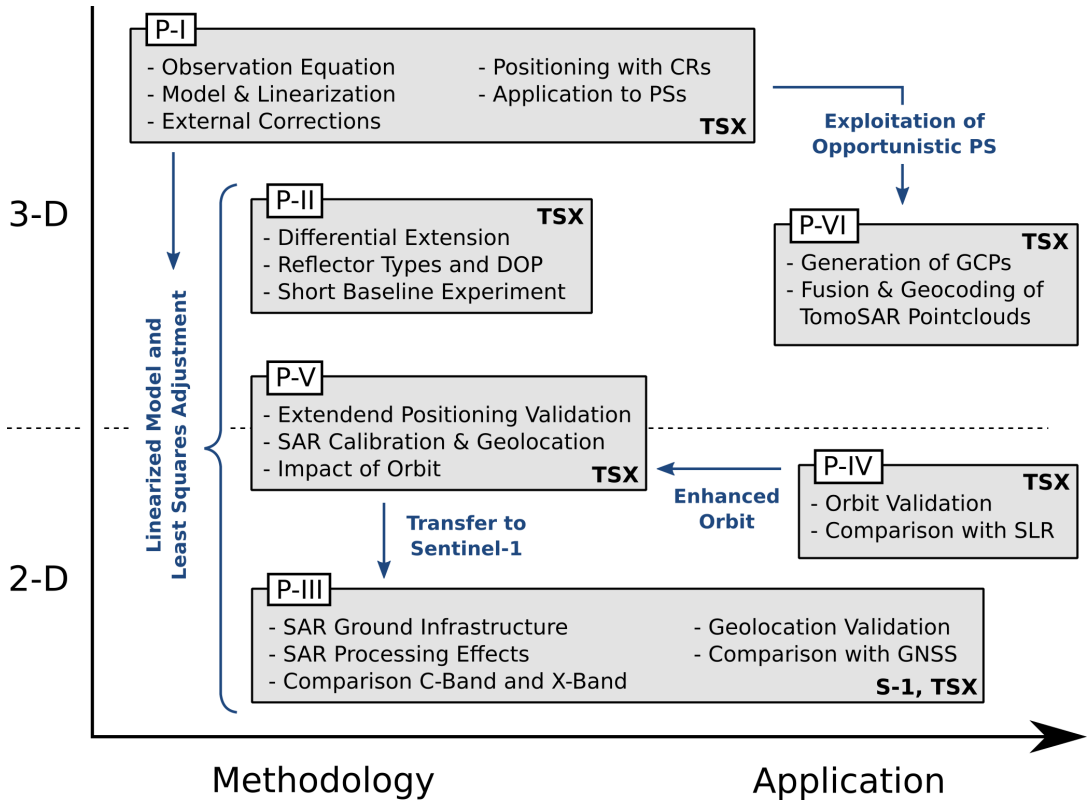

Fig. 1.2: Schematic relationship of the journal publications P-I to P-VI and their contributions to the methods and applications of SAR imaging geodesy. (TSX ... TerraSAR-X, S-1 ... Sentinel-1)

than 5 cm. The positioning method is also applicable to opportunistic PS, which is shown for selected scatterers in the city of Berlin. These PS contributed to the SAR tomography study published in P-VI.

P-II C. Gisinger, M. Willberg, U. Balss, T. Klügel, S. Mähler, R. Pail, M. Eineder, (2017) "Differential geodetic stereo SAR with TerraSAR-X by exploiting small multi-directional radar reflectors", in: *J. Geod.*, 91(1), pp. 53–67.

The publication reports on an experiment with four small multi-directional reflectors carried out with TerraSAR-X at the Wettzell Geodetic Observatory. The aim is to investigate differential positioning with SAR, which is known from GNSS and can be used to further increase the positioning accuracy. The drivers for the SAR positioning quality are the restricted intersection geometry when using conventional CRs, the accuracy of the atmospheric path delay corrections, unknown biases, and the observation noise. The first part of the paper deals with the properties of SAR reflectors and their visibility in the imagery as defined by the signal to clutter ratio (SCR), and the differential positioning is derived by modifying the equations of P-I. The experiment confirms the usability of the differential method for small distances (100 m) without applying any external corrections and the advantage of the multi-directional reflectors in combination with the very high resolution data of TerraSAR-X. The small number of only twelve TerraSAR-X scenes available for this experiment limits the more general interpretation of the results. However, the 3-D positioning accuracy of 2-3 cm achieved for the differential case indicates the potential advantages of such configurations for SAR positioning.

P-III C. Gisinger, A. Schubert, H. Breit, M. Garthwaite, U. Balss, M. Willberg, D. Small, M. Eineder, N. Miranda, (2019) "In-Depth Verification of Sentinel-1 and TerraSAR-X Geolocation Accuracy using the Australian Corner Reflector Array", in *IEEE Trans. Geosci. Remote Sens.*, accepted December 2019, in publication.

The paper is dedicated to the comparative analysis of TerraSAR-X and Sentinel-1 regarding geolocation and the quality of the range and azimuth observations. Although the processing following the developed SAR observation model has been verified for TerraSAR-X to be accurate at the low centimeter-level, the application to other SAR missions requires additional considerations. This is because of the implications associated with the different SAR imaging modes and the algorithms generating the images from raw data. The unique array of permanently installed CRs in Australia allows a detailed investigation of SAR products. The requirements for such ground infrastructure and the SAR geolocation computation are documented as a comprehensive step by step procedure. While TerraSAR-X products with different SAR modes confirm the analysis method and the accuracy of the CRs surveyed by differential GNSS, the detailed assessment of Sentinel-1 finally managed to resolve the geometric distortion discovered in earlier Sentinel-1 results (see section 1.2). The effects embedded in the images are caused by the satellite movement during an acquisition and can be removed in post-processing by corrections derived from SAR theory, as outlined in the paper. The equations are successfully validated by the Sentinel-1 results independently computed by research groups of DLR and University of Zurich (UZH). With the additional corrections Sentinel-1 can achieve an observation accuracy of 6 cm and 25 cm in range and azimuth, respectively. This is comparable to the corresponding TerraSAR-X products when accounting for the differences in radar wavelength and image resolution. A data combination is now readily possible, which is demonstrated by the joint analysis of the CR reference coordinates using the range residuals of both missions.

P-IV S. Hackel, C. Gisinger, U. Balss, M. Wermuth, O. Montenbruck, (2018) "Long-Term Validation of TerraSAR-X and TanDEM-X Orbit Solutions with Laser and Radar Measurements", in *Remote Sens.*, 10(5), pp. 1–20.

The publication presents a comparative analysis between the operational orbit product and a new experimental orbit solution of the TerraSAR-X mission. The knowledge of the orbit is essential to perform accurate positioning with SAR because the method requires the combination of observations across time spans of months or years according to the datum defined by the orbit. Conversely, accurate SAR range and azimuth observations of known positions are sensitive to different orbit solutions. Together with an extensive SLR validation, the analysis spanning six years of data points out the advantage of the experimental orbit solution applying ambiguity fixing for the on-board GPS and a more refined handling of the non-conservative forces. The operational TerraSAR-X orbit is confirmed to be consistent with the observations within 1.7 cm, which can be improved by another 20 % when substituting the enhanced orbit solution.

P-V U. Balss, C. Gisinger, M. Eineder, (2018) "Measurements on the Absolute 2-D and 3-D Localization Accuracy of TerraSAR-X", in *Remote Sens.*, 10(4), pp. 1–21.

The publication provides a summary of the long-term activities of monitoring the TerraSAR-X absolute observation accuracy (geolocation) and the absolute SAR positioning quality. Based on the almost 1000 images that were in total acquired for the five CRs at the three test sites of Wettzell, Metsähovi and GARS O'Higgins, the paper forms the continuation of the earlier work on geolocation and the positioning first presented in P-I. The stability of the SAR observations of both spacecraft of the TerraSAR-X mission are confirmed by the close agree-

ment between the geolocation analysis results across the different measurement series. The SAR observation modelling and the careful geometric re-calibration result in standard deviations of 1.2-1.8 cm and 1.8-2.4 cm for range and azimuth, respectively. The biases are on the same order of magnitude and thus the positioning results are found to be equally accurate. The large number of observations reduce the 95 % confidence level of the 3-D solutions to 1-3 cm. However, because of the confined observation geometry of single trihedral CRs there remain differences between the individual coordinate components.

P-VI X. X. Zhu, S. Montazeri, C. Gisinger, R. F. Hanssen, R. Bamler, (2016) "Geodetic SAR Tomography", in: *IEEE Trans. Geosci. Remote Sens.*, 54(1), pp. 18–35.

The paper illustrates a first application for absolute SAR-based coordinates. The ability to generate global coordinates for PS points that can also be used as scatterers in the phase-based method is particularly useful for multi-pass PSI and tomographic setups. The relative phase-based methods have the drawback to require at least one *a priori* coordinate to define a datum and usually different points have to be used for different viewing geometries. Already the usage of one absolute PS point available in all four geometries processed with the TomoSAR method considerably improved the geocoding and the fusion of the results from four individual stacks of the city of Berlin. To evaluate the quality of the result, the consistency of building footprints now composed of multi-angle data is presented as well as a comparison with an independent laser scanning model. The latter indicates a horizontal accuracy of approximately 20 cm and a typical height accuracy of a few meters. The latter is caused by the limited precision of phase-based methods like TomoSAR in the perpendicular cross-range direction and is not related to the reference point generated with SAR positioning.

The annotation listed in Figure 1.2 for each publication highlight the inputs to the overall scheme, but one should be aware that all publications deal with the entire systems approach, and therefore the annotations were assigned according to the emphasis given to specific elements. P-I forms the core of the thesis because it formulates the SAR range and azimuth observation equations along with the first iteration of the comprehensive observation model. All the further developments are based on these initial concepts, which is indicated by the bracket next to the remaining five publication (Fig. 1.2). The different ways of processing the SAR data (absolute and differential positioning; geolocation analysis; orbit analysis) all belong to a common set of equations that can be solved by least squares methods. The only difference lies in the setup of the parameter vector (see section 2.4). The additional publications dealing with the 3-D positioning are P-II (differential arrangement of the observation equations), parts of P-V (update on the TerraSAR-X positioning experiments at the geodetic observatories), and P-VI (application to opportunistic PS to define a datum). The major part of P-V is dedicated to the long-term analysis of the TerraSAR-X range and azimuth observations and emphasizes the importance of a careful geometric calibration. The same data is used for the TerraSAR-X orbit validation in P-IV, which relies on the calibrated observations to assess the enhanced orbit solution. In turn the enhanced orbit is also discussed in the outlook of P-V. Finally, P-III extends the observation model of P-I for the geometric requirements of SAR image processors to retain the accuracy provided by the payloads and to generalize the model for other missions. This is shown using the example of Sentinel-1. The remaining 2-D geolocation residuals can be used as a measure to independently assess the consistency of the GNSS survey of the Australian CR array with both SAR missions TerraSAR-X and Sentinel-1. These first tests performed in P-III point out the usefulness of such absolute SAR observations for the straightforward combination of different SAR sensors and GNSS results.

In summary, the work carried out in this thesis has addressed several research questions about SAR as a geodetic technique. The answers given below refer to the journal publications and the remaining chapters of the thesis, which contain the comprehensive outline of the theory developed for SAR imaging geodesy (chapter 2) and the comparison of the method with the existing space geodetic techniques SLR and GNSS (chapter 3). As a whole, the thesis answers the following questions:

Q1: What are the components of SAR as a comprehensive geodetic system?

The end-to-end model of SAR can be decomposed into (1) the satellite orbit defining the datum, (2) the on-board timing system, (3) the processing of the raw data, (4) the SAR observation equation of range and azimuth, (5) the handling of observation errors, and (6) the geodetic SAR ground infrastructure. The orbit (1) is addressed in P-IV. The elements (2-5) are discussed in a cohesive manner in chapter 2, but were initially developed in P-I and extended later in P-II and P-III. The details of (6) are given in P-II and P-III.

Q2: What is the accuracy limit of the absolute SAR observations and what are the limiting factors?

For ideal setups, the observations of TerraSAR-X can attain 1-2 cm (1σ standard deviation). The limiting factors are the uncertainties in the atmospheric corrections, the accuracy of the orbit, and the realization of the absolute time on board of the satellite (P-III; P-V; chapter 2). On a global scale, the trade-offs between ground coverage and resolution lead to error contributions from the SCR, even in the case of large size reflectors. The atmospheric corrections inferred from global models instead of complementary GNSS observations are also expected to contribute to the uncertainty in range (P-III; chapter 3).

Q3: Which are the observation equations of SAR imaging geodesy?

The two-way ranging equation and the Doppler equation in zero-Doppler configuration accurately describe the geometry of the range and azimuth observations in an Earth-centered frame. Along with the requirements and corrections of the SAR observation model, the equations enable a unified approach for SAR imaging geodesy (P-I; P-II; P-III; chapter 2).

Q4: What accuracy is attainable with SAR positioning?

The drivers for the positioning accuracy are the quality of the corrected observations, the number of images, the orbit accuracy, and the geometric configuration. For the best case setups with TerraSAR-X that use several tens of images, the 3-D accuracy is on the order of 3 cm for trihedral CRs (P-V). Improvements in the positioning accuracy approaching the 1 cm level should become possible with geometric configurations that combine ascending and descending acquisitions to determine the target position (P-II; chapter 3). A differential setup offers additional possibilities to increase the positioning accuracy (P-II).

Q5: What are possible future applications for SAR imaging geodesy?

The SAR-based positions of PS can be used as GCPs for phase-based PSI and TomoSAR results (P-VI), but also for other remote sensing data like optical imagery (chapter 3). Further applications include, e.g., the precise positioning to monitor areas or features of interest, the validation of orbit solutions, and possibly even contributions to the ITRF computation (chapter 3; P-IV).

2 Methodology

2.1 SAR Image Formation and Observables

SAR remote sensing uses the transmission and reception of pulsed signals in side-looking orientation to form a radar image of the Earth surface. The image acquisition is independent of the time of day because of the active illumination by the payload, while the usage of microwave signals (generally between 1-10 GHz) gives the SAR all-weather capability (Curlander and McDonough, 1991).

The key element of SAR is the coherent system governed by a stable oscillator that preserves the time and the phase of the transmitted pulses, which allows the formation of a synthetic aperture along the sensor trajectory, even with moderately sized antennas. Otherwise a real aperture system would require antennas with an extent of several kilometers to achieve meter resolution in the microwave frequency regime at the distance of near Earth orbits (Curlander and McDonough, 1991). The coherent data acquisition, however, gives computational access to an along-track separation of the signal returns by exploiting the Doppler shift caused by the sensor movement and the variation of the sensor-to-target geometry. Consequently, the along-track resolution (or azimuth resolution) of SAR is proportional to the time a target remains in view of the radar beam. It can be shown that the resolution limit ρ_a of a conventional SAR in stripmap mode approaches half the length of the SAR antenna L_a (Curlander and McDonough, 1991):

$$\rho_a = \frac{L_a}{2}. \tag{2.1}$$

The resolution of SAR in the side-looking range direction is defined as the minimum separation of two objects in the radar echo, which is governed by the length of the transmitted radar pulse. Achieving a useful meter-level resolution would require very short pulses (about 10 nanoseconds) that in turn would limit the signal-to-noise ratio of the pulse echo. Therefore, range compression of long phase-coded pulses is applied, for which the resolution ρ_r becomes a function of the transmitted bandwidth B_r (Curlander and McDonough, 1991):

$$\rho_r = \frac{c}{2 \cdot B_r}, \tag{2.2}$$

with c denoting the speed of light in vacuum. From Eq. 2.2 it can be concluded that a bandwidth of 100 MHz is sufficient to support a range resolution of 1.5 m. The independence of the range and azimuth resolution from both the radar wavelength and the distance to the objects is peculiar to SAR. There are technical and regulatory constraints for an arbitrary increase of the bandwidth and the SAR antenna requires a certain size to provide the gain for a sufficient signal-to-noise ratio and to prevent overlaps in the range echos (Curlander and McDonough, 1991). Within these boundaries, however, the SAR concept enables the design of highly versatile imaging instruments.

The transmission of the pulses is performed with a selected pulse repetition frequency (PRF; on the order of kilohertz). The backscattered echoes of the area covered by the antenna footprint are recorded between two transmission events, when the SAR is temporarily switched to receive mode (Cumming

and Wong, 2005). The echoes are time-tagged with an absolute receive time information (in modern SAR provided by the on-board GNSS) and stored as individual packages for downlink. On ground, the SAR processor arranges the echoes of an acquisition in a two-dimensional data matrix, with one dimension referring to the two-way round trip time and the other to the receive time label (azimuth). This raw data matrix already resembles the basic structure of the later SAR image, but the signals have to be focussed in order to produce the fully resolved image. To generate and annotate the final image, a convention has to be assumed for the instant of time for which the raw data are processed for. In many ways the instant of zero-Doppler has become the most convenient choice, because the data are converted to an orthogonal 2-D representation naturally associated with an image (Cumming and Wong, 2005). It is important to note that the transmission and reception is performed by a constantly moving sensor and that both dimensions range and azimuth are coupled by the measurement process (Cumming and Wong, 2005). Therefore, a decoupling needs to be done on top of the focussing to generate an image output with the desired zero-Doppler geometry (P-III). Moreover, one has to deal with complex signals stemming from the demodulation process that removes the high-frequency carrier from the real transmitted signal (Cumming and Wong, 2005). The signal structure along with the coupling of both dimensions require careful considerations in the spectral signal processing operations performed by the SAR processor.

In the time domain, the focussing operation corresponds to a convolution with known replicas of the signal structure in both data dimensions (Cumming and Wong, 2005). The computation for the range dimension is relatively straightforward as the transmitted pulse signal is precisely defined. Obviously, the process can be vastly accelerated when the operation is performed in the frequency domain by applying fast convolution to each range line. This is equivalent to pulse compression with a matched filter (Cumming and Wong, 2005). The azimuth, however, is more challenging as the signal structure varies according to the sensor-to-ground geometry and the returns from each location are moving across the range lines because of the change in distance during acquisition (known as range cell migration). This characteristic prevents the usage of a single 1-D filter for accurate azimuth focussing. Overcoming these difficulties and maintaining the computational efficiency of frequency domain operations has led to the development of several focussing algorithms, which represent different levels of trade-offs between accuracy and efficiency (Cumming and Wong, 2005). The details of these algorithms are of no immediate concern to SAR imaging geodesy, as long as the algorithmic implementations are aware of the implications for geometric quality of the focussed SAR image (see section 2.3.3). If this holds true, the processor generates a proper orthogonal matrix of complex numbers (pertaining magnitude and phase), for which each range line refers to a single zero-Doppler time and the location within the line is the two-way round trip time. This first usable SAR product is referred to as the level 1 single look slant range complex (SSC) image. It forms the basic input for SAR imaging geodesy and is usually provided for each SAR mode offered by the sensor.

The most used acquisition modes over land of current spaceborne SAR missions are stripmap, ScanSAR, spotlight SAR and the Terrain Observation with Progressive Scan (TOPS) mode (for details see Curlander and McDonough, 1991; Cumming and Wong, 2005; de Zan and Guarnieri, 2006). In terms of the image products, the main differences are the azimuth resolution and the coverage on ground. The key properties of the SAR modes are as follows:

- **Stripmap:** The orientation of the antenna is kept fixed and the selected radar beam sweeps the ground according to the antenna footprint and the movement of the platform. The azimuth resolution is driven by the length of the antenna, and in principle the sensor can acquire a permanent stream of data that seamlessly covers the defined swath as the sensor progresses along the trajectory. Practical limitations for the acquisition length are data storage and data downlink, as well as the power demand.

- **ScanSAR:** The configuration is identical to stripmap, but to achieve wider coverage in the range direction, the sensor acquires multiple swaths in parallel by toggling the beams in cross-track direction to measure short bursts. Overlaps in the beams ensure the seamless ground coverage. The resolution in azimuth is reduced because for each of the areas on the ground the pulses forming the synthetic aperture are lessened by the number of selected subswaths. Therefore, the best possible azimuth resolution of ScanSAR corresponds to the azimuth resolution of the equivalent stripmap mode times the number of the used subswaths.

- **Spotlight:** The spotlight mode increases the resolution in azimuth at the cost of giving up seamless ground coverage. The beam is steered to counter the sensor movement and to increase the dwell time over an area which extends the synthetic aperture. The speed of the steering controls the along-track coverage and can be defined as sliding spotlight, where the beam is still allowed to progress with the sensor movement (but slower than non-steered stripmap), or as staring spotlight, where the illuminated area is kept fixed.

- **TOPS:** The TOPS mode avoids the slicing of the antenna footprint used in ScanSAR to cover the parallel subswaths by steering the beam in along-track direction in addition to the platform movement. This is a reversal of the spotlight mode. While the spotlight mode increases the azimuth resolution, the TOPS mode deliberately decreases the azimuth resolution and uses the time saved to scan bursts of adjacent swaths. The sweeping of the beam in along track achieves a constant weighting of the antenna amplitude pattern and a more homogeneous signal-to-noise-ratio for the targets on ground. This avoids the elaborate amplitude calibration required to remove the periodic amplitude variations in ScanSAR data (scalloping effect; de Zan and Guarnieri, 2006).

Regardless of the underlying SAR mode, the processed level 1 SSC image preserves the two-dimensional grid of range and azimuth radar coordinates, which allow the extraction of features at sub-pixel level. These coordinates are the basic observables in imaging geodesy, for which the image acts as a search space to obtain the measurements. Single isolated scatterers like the trihedral CRs represent the impulse response of the SAR (Cumming and Wong, 2005). They appear as sinc-like functions that spread over several pixels in cross-shaped signatures and can be accurately localized in the image grid, see Fig. 2.1. The process is termed point target analysis (PTA), which does not only yield the pixel position, but can be also used to derive quality parameters like the impulse response width (a measure for the image resolution) or the peak sidelobe ratio (a measure for the contrast) (Cumming and Wong, 2005).

Assuming a given image resolution of 1 m and aiming at a SAR measurement accuracy on the order of 1 cm, then the PTA must provide the peak location with about 1/1000 of a pixel. An efficient way to achieve such a precision is the application of spectral zero padding for the image subset containing the point target signature. This corresponds to an oversampling of the complex data using a sinc-like interpolator (Cumming and Wong, 2005). The oversampling factor is equivalent to the number of inserted zeros, but large numbers of 1024 or 2048 lead to a computationally expensive inverse Fourier transformation of the padded spectrum. This can be overcome by applying a two step procedure that first performs a moderate oversampling of 32, and then localizes the peak by fitting an analytical paraboloid surface to the central peak area (P-III; Stein, 1981; Balss et al., 2012). An example is shown in Fig. 2.1.

The PTA can be configured to produce arbitrarily fine results. However, the physical precision limit $\sigma_{r,a}$ of the sub-pixel extraction in range and azimuth is linked to the amount of signal returned by

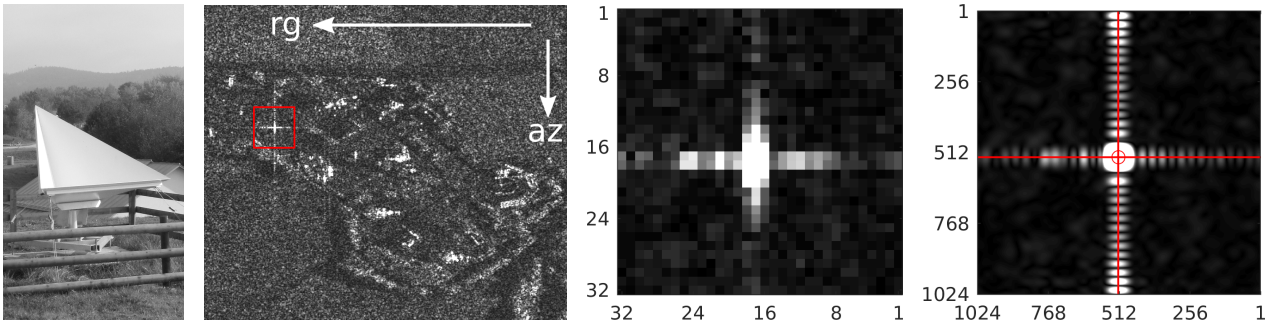

Fig. 2.1: Point target analysis to extract the range and azimuth observations at the sub-pixel level. Corner reflector with 1.5 m edge size at Wettzell geodetic observatory (a), TerraSAR-X high-resolution spotlight image of Wettzell (b), close-up of CR impulse response (c), and detected peak location after zero padding with a factor 32 and the fit of a paraboloid surface (d). The images show the amplitude of the SSC product (clipped for visualization).

the target versus the background clutter, i.e. the SCR, and the resolution $\rho_{r,a}$ of the image product (Stein, 1981; Bamler and Eineder, 2005):

$$\sigma_{r,a} = \frac{\sqrt{3}}{\pi\sqrt{2}} \frac{1}{\sqrt{SCR}} \cdot \rho_{r,a}. \tag{2.3}$$

In theory, the SCR is described as the ratio between the target radar cross section (RCS) and the RCS of the background (Freeman, 1992). The RCS of the background is governed by the surface type (e.g., asphalt, grass, ...), the radar wavelength, and the selected polarization (Ulaby and Dodson, 1989). For trihedral targets, the RCS increases with the fourth-power of the edge defining the corner and the square of the radar frequency (e.g., Doerry, 2008). Therefore, SAR payloads designed for high resolution and shorter wavelengths (= higher radar frequencies) have a distinctive advantage in SCR and can make use of smaller targets to achieve high observation precision (see the small targets used with TerraSAR-X staring spotlight in P-II). For a given image, the SCR of a point target can be estimated by computing the intensity of the background surrounding the impulse response and the intensity of the peak itself (Rosich and Meadows, 2004). A discussion of experimentally determined SCR values of CRs with different sizes in different image products of TerraSAR-X and Sentinel-1 is given in P-III. Based on the experience of the experiments, a SCR on the order of 25-30 dB should be envisaged for SAR image products with a resolution of 2-3 m to ensure a range and azimuth observation precision at the centimeter-level (P-II; P-III). In accordance with this requirement, triangular trihedral CRs with an edge length of 1.5 m have been installed at the geodetic observatories Wettzell and Metsähovi, and at the Australian CR array.

Furthermore, trihedral CRs have a moderate decrease of the RCS with respect to the ideal boresight, which enables measurements with a fairly homogeneous quality within $\pm 20\,^\circ$ of the boresight direction (Doerry, 2008). A properly aligned trihedral CR remains visible in all pass geometries acquired by a spaceborne SAR sensor. It is important to note that the CR does not only remain precisely detectable, but also the location of the signal return (the CR phase center) is stable, provided that the reflector has been manufactured with tight tolerances (Doerry, 2008; Garthwaite, 2017). This property is of crucial importance as it ensures measurements that can be reliably extracted by the PTA from the SSC images and the combination of these measurements to retrieve the coordinates with SAR positioning.

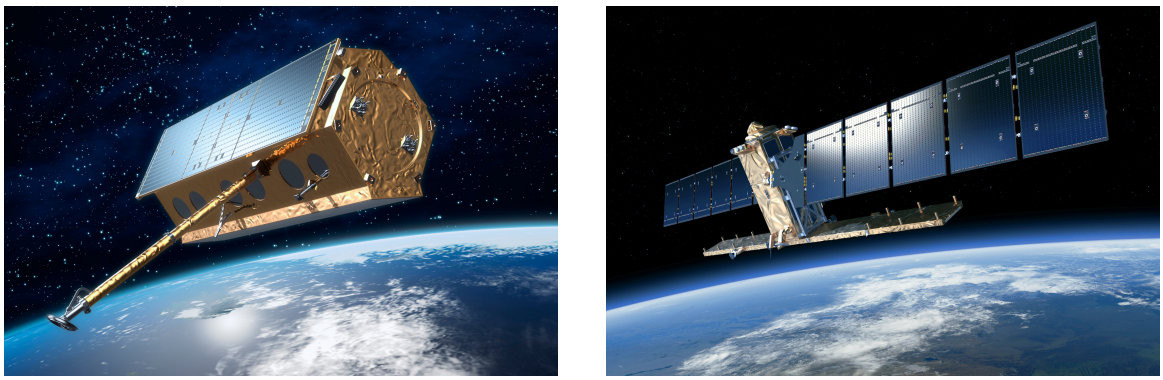

Fig. 2.2: Artist impression of TerraSAR-X (left) and Sentinel-1 (right) in space. The missions became the drivers for the development of SAR imaging geodesy and provided the data for the research of this thesis. (Image credits: DLR / EADS Astrium; ESA / ATG medialab)

2.2 TerraSAR-X and Sentinel-1

The TerraSAR-X mission developed and operated by DLR as well as the Sentinel-1 mission managed by the European Space Agency (ESA) in the framework of the EU Copernicus programme provided the experimental data to investigate and test the methods of SAR imaging geodesy (Fig. 2.2). The key figures of both missions are summarized in Table 2.1. The focus of TerraSAR-X on scientific and technical developments in SAR methodology is a key asset of the mission design (Buckreuss et al., 2018), which triggered the development of SAR imaging geodesy (Eineder et al., 2011). Thus the majority of the work reported in this thesis was carried out with TerraSAR-X (see Fig 1.2). The mission concept of Sentinel-1 is tailored to deliver SAR as a service (Torres et al., 2012). However, the global scale data acquisition, the open data policy, the transparent processing methods, and the geodetic grade payloads make it an obvious choice to transfer the knowledge gained with the TerraSAR-X mission (P-III).

The TerraSAR-X mission consists of two spacecraft, TerraSAR-X (TSX) and TanDEM-X (TDX), which were launched in 2007 and 2010, respectively. They are operated in close formation in a near-polar sun-synchronous orbit, which has an altitude of 514 km and a repeat cycle of 11 days (Werninghaus and Buckreuss, 2010; Buckreuss et al., 2018). The satellite separation is only on the order of a few hundred meters and was selected for bistatic interferometry to generate the primary scientific product: a global DEM with a resolution of 12 x 12 m and a height accuracy of 10 m (Wessel, 2018). The orbit is tightly controlled within a radius of 250 m with respect to the defined reference trajectory and the POD is of crucial importance for the primary mission goal and the related SAR applications. Therefore, both spacecraft are equipped with geodetic dual-frequency GPS receivers and optical retro-reflectors for SLR orbit validation. While the single satellite science orbit has an accuracy requirement of 20 cm, the tight requirement of 1 mm for the baseline between the satellites demands meticulous care for the reduced-dynamic POD approach (Montenbruck et al., 2011). The emphasis on the mission's orbit also proved beneficial for the TerraSAR-X science orbit product. Already during the first commissioning of TSX, the science orbit was found to be better than 4 cm when compared to the SLR observations (Yoon et al., 2009), whereas the long-term analysis of the science orbit confirmed the accuracy with better than 2 cm (P-IV; Hackel et al., 2017). This ranks TSX and TDX among the most accurately determined low Earth satellites for geodesy (Arnold et al., 2018). Ongoing research on the dynamic models and the fix of the GPS ambiguities to integer values has been further improving the orbit accuracy towards the 1 cm level. This TerraSAR-X orbit product is presently only available on an experimental basis (P-IV; Hackel et al., 2017).

Tab. 2.1: Key specifications of the SAR missions TerraSAR-X and Sentinel-1 (Buckreuss et al., 2018; Fritz and Eineder, 2013; Torres et al., 2012; Bourbigot et al., 2015)

	TerraSAR-X	**Sentinel-1**
Spacecraft (launch)	TSX (2007); TDX (2010)	S1A (2014); S1B (2016)
Orbit type	sun-synchronous[1]	sun-synchronous[1]
Repeat cycle	11 days	12 days
Inclination	97.4 °	98.2 °
Orbit height	514 km	712 km
Absolute orbital tube	250 m radius	50 m radius
Payload(s) for POD	dual-frequency GPS; SLR	dual-frequency GPS
Geodetic datum[2]	IGS14	IGS14
Orbit accuracy[3]	20 cm / 2 cm	5 cm / < 5 cm
Radar frequency	9.65 GHz	5.405 GHz
Antenna size	5.0 x 0.8 m	12.3 x 0.8 m
Transmit bandwidth	up to 300 MHz	up to 100 MHz
Polarization	HH / VV / HV / VH	HH / VV / HV / VH
Access range[4]	20 °–55 °	20 °–45 °
Nominal view[5]	right-looking	right-looking
Geolocation requirement[6]	1 m	2.5 m
SAR modes[7]		
Stripmap:	1.2 x 3.3 m @ 30 x 50 km	2.5 x 4.5 m @ 80 x ... km
Interferometric Wide Swath (3 beams):		3.1 x 22.0 m @ 250 x ... km
Extra Wide Swath (5 beams):		12.5 x 43.0 m @ 375 x ... km
ScanSAR (4 beams):	1.2 x 18.5 m @ 100 x 150 km	
Wide ScanSAR (6 beams):	2.5 x 40.0 m @ 220 x 200 km	
Spotlight:	1.2 x 1.7 m @ 10 x 10 km	
High-resolution spotlight:	0.6 x 1.1 m @ 10 x 5 km	
Staring spotlight:	0.6 x 0.24 m @ 7 x 3 km	

[1] Dusk-dawn configuration; ascending equator crossing at approximately 18:00 local time
[2] Defined by the IGS GNSS products (orbits, clocks); Hackel et al. (2017), Peter et al. (2017)
[3] Required vs. achieved, see Yoon et al. (2009); P-IV; Peter et al. (2017)
[4] Incidence angles accessible by the SAR; exact values depend on the chosen SAR mode
[5] Orientation of the SAR payload in nominal operation with respect to satellite heading
[6] According to the product with the highest resolution
[7] Resolution of single polarization SSC product; slant range x azimuth @ scene size on ground

The payload of TerraSAR-X operates in X-band with a carrier frequency of 9.65 GHz and can use a bandwidth of up to 300 MHz that results in the best possible slant range resolution of approximately 0.6 m. The payload was designed and carefully calibrated according to the geometric requirements of 2 m[1] (Schwerdt et al., 2010). The same applies to the TerraSAR-X Multimode SAR Processor (TMSP) generating the images for the different SAR acquisition modes (Breit et al., 2010). Aside from the common stripmap mode with a good balance of resolution and ground coverage, the mission offers two flavors of the ScanSAR mode for wide-area acquisition, two sliding spotlight modes (spotlight and high-resolution spotlight), and the staring spotlight mode with an extremely high resolution of 0.5 x 0.24 m (see Table 2.1).

[1] The initial goal was 2 m but the product specification was changed to 1 m (Breit et al., 2010; Fritz and Eineder, 2013)

In general, the data access is order driven and commercially organized, but access is granted to scientific users at moderate pricing after the acceptance of a science data proposal (Werninghaus and Buckreuss, 2010). Except for fast data delivery in case of an emergency (e.g., natural disasters like floods or earthquakes), all the image products are generated by the TMSP with final science grade auxiliary products, most importantly the orbit (Fritz and Eineder, 2013). Any re-ordering invokes the reprocessing of the images from the raw data with the latest TMSP version, which ensures consistent products across the whole TerraSAR-X archive.

In order to continue Europe's SAR satellite series in the C-band (ERS-1, ERS-2, Envisat), the Sentinel-1 programme was established as one of the missions of the Copernicus Earth observation programme funded by the European Commission (formerly known as Global Monitoring for Environment and Security - GMES; Torres et al., 2012). The first satellite S1A was launched in 2014 and was joined in 2016 by a second identical satellite S1B. Like in the case of the TerraSAR-X mission, the Sentinel-1 satellites operate in a sun-synchronous low Earth orbit (nominal height 712 km; see Table 2.1) but with a slightly larger repeat cycle of 12 days. The spacecraft are placed in the same orbit but separated by 6 days. Because of the tight orbit requirement for accurate repeat pass interferometry, the absolute orbit control is maintained within 50 m of the reference trajectory (Torres et al., 2012). The POD relies on the dual-frequency GPS as key payload of both satellites. However, without the additional SLR payload, the orbit validation of the Sentinel-1 mission is based on internal consistency checks and the comparison of solutions computed by different analysis centers, which confirm the orbit accuracy to be better than 5 cm (Peter et al., 2017).

The SAR instrument uses a radar frequency of 5.405 GHz and supports a bandwidth of up to 100 MHz (equivalent to 1.5 m slant range resolution). The mission is operated as a continuous data service, providing a coverage of Europe and other priority regions within every three days, and a global coverage with different temporal resolutions of 6 to 24 days according to monthly acquisition plans (CSC Mission Management Team, 2018). Data access is free of charge after registration at the Sentinel open access hub[1]. The primary SAR mode of Sentinel-1 is the interferometric wide swath mode, i.e. the implementation of the TOPS mode (see section 2.1), for which the burst pattern on ground is kept fixed within an absolute pointing limit of 50 m and is closely repeated for each acquisition. In addition, there is a stripmap mode used at selected monitoring sites (chiefly volcanic islands) and a wide area version of the Interferometric Wide Swath (IW) mode with five beams used for ice monitoring in the polar regions (CSC Mission Management Team, 2018). The image generation is performed by the processor of the Instrument Processing Facility (IPF) according to a 24 h data distribution strategy. This demands a processing using auxiliary data as available at the time of acquisition, e.g., the so-called restituted orbit product, and the storage in the archive for rapid data dissemination. The archived images do not undergo any reprocessing and homogenization after updates in the auxiliary files or of the IPF itself. Therefore, long-term analysis will contain images of different processing setups. However, maintaining the continuity of product series governs the changes made in the IPF, and to keep the process transparent for the user, the configuration files of the IPF as specified in the product annotation are accessible via the Sentinel-1 quality control website[2]. The website also includes the final precise orbit ephemerides with a latency of 22 days with respect to acquisition, which can be used to substitute the restituted orbit annotated to the image products. Because of the long-term monitoring concept and the successors of S1A and S1B already in preparation (Spataro et al., 2018), the Sentinel-1 mission will build up an unprecedented archive of consistent SAR imagery in the upcoming decade. This provides considerable potential for future applications in SAR imaging geodesy.

[1] https://sentinel.esa.int/web/sentinel/sentinel-data-access
[2] https://qc.sentinel1.eo.esa.int/

2.3 SAR Observation Model

The geometry of a SAR image acquisition (see section 2.1) is accurately described in an Earth-centered, Earth-fixed (ECEF) frame by two equations: an equation for the along-track component linked to the Doppler shift and an equation for the range corresponding to the two-way signal time of flight. These equations are coupled by the movement of the sensor and are often referred to as the range-Doppler equations (Leberl, 1990; Curlander and McDonough, 1991). When additionally accounting for the observation errors associated with the SAR imaging process, the equations provide a comprehensive model, which relates the two-dimensional SAR observations range and azimuth to a point in 3-D space. Therefore, the range-Doppler equations are well-suited to form the basis of the envisaged observation model and can be interpreted as the fundamental SAR observation equations, very much like the pseudorange equation of GNSS (Teunissen and Montenbruck, 2017). The following sections shortly introduce the equations and the error models and discuss the linearization along with the least squares solution methods for the applications SAR calibration and SAR positioning.

2.3.1 Range-Doppler Equations

Assuming a satellite position vector $\mathbf{X}_S = [x_S, y_S, z_S]^T$ and a target position vector $\mathbf{X}_T = [x_T, y_T, z_T]^T$ in the ECEF frame, the slant range ρ observed by the SAR system can be stated as

$$\begin{aligned} \rho &= |\mathbf{X}_S - \mathbf{X}_T| \\ &= \sqrt{(x_S - x_T)^2 + (y_S - y_T)^2 + (z_S - z_T)^2}. \end{aligned} \tag{2.4}$$

This general type of equation is well-known from other geodetic techniques providing range observations, see SLR (Combrinck, 2010) or the code observations of GNSS (Teunissen and Montenbruck, 2017). Internally, SAR payloads operate with a stable oscillator and the transmission and reception of compressible pulses (see section 2.1). Consequently, the SAR slant range is equivalent to a distance measurement with a single clock, for which the two-way signal travel time τ_r and the geometric range ρ are related by the simple conversion

$$\tau_r = \frac{2 \cdot \rho}{c}. \tag{2.5}$$

The observation equation for the azimuth is derived from the Doppler shift induced by the movement of sensor, which forms the fundamental principle of SAR imaging, because the different Doppler shifts enable the echo data separation in along-track direction (see section 2.1). Using the above notation, the Doppler shift f_D of the radar signal recorded for a target $\mathbf{X}_T$ is defined as (Curlander and McDonough, 1991):

$$f_D = \frac{2}{\lambda} \cdot \frac{\dot{\mathbf{X}}_S \cdot (\mathbf{X}_T - \mathbf{X}_S)}{|\dot{\mathbf{X}}_S| \cdot |\mathbf{X}_S - \mathbf{X}_T|}. \tag{2.6}$$

The λ is the wavelength of the radar carrier signal, and $\dot{\mathbf{X}}_S$ denotes the satellite velocity vector associated with the satellite position $\mathbf{X}_S$. From the latter, the coupling with the range (Eq. 2.4) is immediately perceived, because range and Doppler shift are defined for the same instant of time represented by the orbital state vector. From a geometric point of view, the Doppler shift can be also expressed by a Doppler cone described as a function of the squint angle α, i.e. the angle between

the plane perpendicular to the velocity vector and the sensor boresight vector (Cumming and Wong, 2005). The conversion between Doppler shift and squint angle is given by (Leberl, 1990):

$$\sin(\alpha) = \frac{\lambda \cdot f_D}{2}. \tag{2.7}$$

However, for SAR data accurately processed for zero-Doppler, the squint angle vanishes and the Doppler-cone is reduced to the zero-Doppler plane, which solely depends on the sensor-to-target geometry at the instant of zero-Doppler:

$$0 = \frac{\dot{\mathbf{X}}_S \cdot (\mathbf{X}_T - \mathbf{X}_S)}{|\dot{\mathbf{X}}_S| \cdot |\mathbf{X}_S - \mathbf{X}_T|}. \tag{2.8}$$

Finally, if we identify the azimuth as the absolute time t linked to the orbital state as $\mathbf{X}_S(t)$ and $\dot{\mathbf{X}}_S(t)$ for the time of zero-Doppler $t = t_a$, Eq. 2.4 and Eq. 2.8 provide a system of equations that relates the SAR observations t_a and τ_r with the 3-D target $\mathbf{X}_T$.

The solution of the SAR observation equations for the target coordinates by means of least squares adjustment will be discussed in detail in section 2.4. Conceptually, the method aims at minimizing the squared residuals between observations and the model, which requires a given orbit from POD and ideally the modelling of all other systematic errors present in the SAR system. The topic of POD was not in the scope of this thesis, because the precise science orbit of TerraSAR-X already provides a very high accuracy and is fully compliant with the geodetic standards (Yoon et al., 2009; Montenbruck et al., 2011; Hackel et al., 2017). Therefore, the orbit is considered known, and the implications of this assumption are addressed in the subsequent section 2.3.2.

The observation errors of a SAR system consist of the SAR-specific effects related to hardware and the processing of the raw data, and of the atmospheric perturbations described by the tropospheric and ionospheric path delays. Schematically written, the recorded SAR range and azimuth observations t_a and τ_r include the following error contributions:

$$\begin{aligned} t_a &:= t_a + \Delta t_{sys} + \Delta t_{ion} + \Delta t_e \\ \tau_r &:= \tau_r + \Delta\tau_{sys} + \Delta\tau_{tro} + \Delta\tau_{ion} + \Delta\tau_e \end{aligned} \tag{2.9}$$

where

$\Delta\tau_{sys}, \Delta t_{sys}$ comprise the SAR-related effects, e.g., the on-board timing or the residual effects associated with SAR data processing,

$\Delta\tau_{ion}, \Delta t_{ion}$ are the impacts of the path delay of the dispersive ionosphere,

$\Delta\tau_{tro}$ is the tropospheric path delay of the neutral atmosphere in range, and

$\Delta\tau_e, \Delta t_e$ account for unmodelled systematic errors and the random errors, including noise.

In addition, there are the displacements of the solid Earth surface caused by tidal-related deformations and tectonic processes. They are accounted for by modelling the target coordinates $\mathbf{X}_T$ according to the standards of the ITRF (Petit and Luzum, 2010; Altamimi et al., 2016). The following sections provide an overview of the different methods to reduce these errors. At present, SAR mainly relies on *a priori* models and complementary observations, but in order to account for biases and unmodelled errors, the systematic parts of τ, t_e are estimated in dedicated calibration experiments (see P-V for TerraSAR-X). As for the random parts of τ, t_e, they comprise the uncertainties of the corrections, the random error of the orbit, the finite precision of the PTA because of the SCR (cf. section 2.1), and other random error contributions. The entity of random errors defines the accuracy of the SAR

observations, which can be empirically quantified from the residuals of the geometric calibration experiments. Furthermore, a differential setup relying on reference coordinates can eliminate or mitigate most of the systematic errors. These two topics, the calibration and the differential approach, will be addressed in the solutions of the least squares algorithm in section 2.4.

2.3.2 Orbit Requirements

In order to use an orbit as a datum for accurate measurements in an ECEF frame, the solution of the POD carried out in a quasi-inertial Earth-centered space-fixed (ECSF) frame has to be transformed to the ECEF frame. The standards and models underlying this transformation are subject to global reference frame determination (Petit and Luzum, 2010). The same standards and models also apply to the observations taken on-board the SAR satellite (GNSS, star trackers) or the measurements taken from ground stations to the satellite (SLR), which require consistent background products (orbits, clocks, station coordinates) and models for data reduction as input to the POD processing (Montenbruck et al., 2011; Arnold et al., 2018).

The most accurate solutions for the ECEF and ECSF frames and the transformation parameters are the ITRF and the ICRF (International Celestial Reference Frame), with the latest solutions given by the ITRF2014 (Altamimi et al., 2016) and the ICRF2 (Fey et al., 2009), respectively. The frames are the collaborative work of geodetic, geophysical and astronomical associations, and are released under the umbrella of the International Earth Rotation and Reference Systems Service (IERS) (Dick and Thaller, 2016). These realizations involve conventions and specifications which deal not only with the aforementioned transformation, but also include the models required to remove the tidal-related signals of the solid Earth in terrestrial ITRF coordinates. For the latest release of these conventions see the IERS conventions 2010 (Petit and Luzum, 2010). Note that the geodynamic models form the basis for the corrections discussed in section 2.3.5.

The outcome of an ITRF realization is a consistent set of globally distributed coordinates for the GNSS, SLR, VLBI, and DORIS stations contributing measurements to the ITRF determination (Altamimi et al., 2016). Because the station coordinates contain the temporal evolution of the additionally estimated linear velocities[1], the stations can be defined for arbitrary epochs in time. They are used by geodetic services, e.g., the IGS, to derive products like orbits, clocks or atmospheric delays that are consistent with the ITRF (Villiger and Dach, 2018). Therefore, the orbit of a SAR satellite becomes a derivative of the ITRF, if these products and the IERS conventions are applied for the POD as it is the case for TerraSAR-X and Sentinel-1 (Montenbruck et al., 2011; Arnold et al., 2018). In other words: the daily sets of position and velocity vectors of the SAR satellite can provide a consistent datum for the absolute SAR techniques.

The level of consistency of an orbit accurately determined in the ITRF is illustrated by the SLR analysis carried out for TSX and TDX (P-IV; Arnold et al., 2018). Even for the slightly less accurate TerraSAR-X science orbit distributed with the SAR products, the SLR residuals across 11 stations show less than 20 mm standard deviation, and the monthly position offsets derived for radial, along-track and across-track directions remain below 12 mm (P-IV). The Sentinel-1 POD follows the same standards and procedures, and although the independent assessment of the orbit is limited by the lack of a SLR retro-reflector, it is safe to assume an orbit accuracy of better than 50 mm (Peter et al., 2017). Thus, for both missions the orbit solutions are on a par with the measurement accuracy presently achievable with the SAR instrument. As a general requirement, the orbit needs to be predetermined in the ITRF with an accuracy not limiting the absolute SAR observations.

[1]Note that seasonal components were estimated for a few selected stations in the latest release (Altamimi et al., 2016)

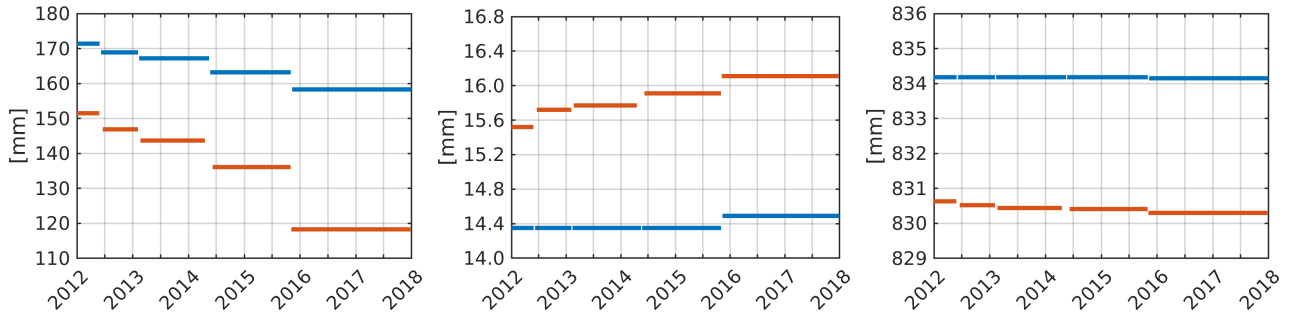

(a) Mech frame X **(b)** Mech frame Y **(c)** Mech frame Z

Fig. 2.3: Time series of the SAR antenna phase center offset for TerraSAR-X (blue) and TanDEM-X (red) as annotated in the SAR products. The vectors refer to the satellite mechanical coordinate frame (Kahle, 2012).

Another important aspect closely related to POD is the difference between the satellite center-of-mass (CoM) and the reference point of the SAR antenna. Already for the POD, the offsets to the SLR retro-reflector or the on-board GNSS antenna have to be taken into account when reducing the data for the satellite CoM. This requires knowledge of the spacecraft attitude and calibrated offset vectors between CoM and the payload reference points (Yoon et al., 2009; Peter et al., 2017). The same procedure applies for the SAR payload and the range and azimuth measurements. Furthermore, the CoM of a satellite will likely change over mission lifetime due to fuel consumption which causes changes in the different payload offset vectors. For the TerraSAR-X mission, the fuel consumption is accounted for during orbit determination (see P-IV), and the varying SAR antenna offset vector is already considered as piece-wise update in the orbit state vectors annotated to the TerraSAR-X image products (Fritz et al., 2007). Therein, the dedicate offset vector is listed as well. The temporal evolution of the SAR antenna phase center offset for TSX and TDX is visualized in Fig. 2.3. The total offset is on the order of 0.85 m, and changes of a few centimeters occur in the X-component which approximately corresponds to along-track orbit direction (Kahle, 2012). In the case of Sentinel-1, the orbit is only provided at the CoM which requires the additional consideration of the antenna offset. However, the offset vector for the SAR antenna is not available in the annotation distributed with the image products (Bourbigot et al., 2016). The effect is partly compensated for by the Sentinel-1 range and azimuth calibration constants, but proper correction is desirable. Therefore, the provision of the SAR antenna phase center offset should be considered an additional requirement for the SAR orbit annotated to the image products.

2.3.3 SAR-related Effects

The SAR-related effects comprise several errors which are either related to the design of SAR hardware itself or arise from approximations introduced to efficiently process the SAR raw data by spectral methods (P-I; P-III). The hardware effects may not necessarily apply to all SAR satellites to the same degree, but the effects discussed here are likely encountered in most of today's missions. They can be identified in level 1 SSC SAR products as deviations from the orthogonal zero-Doppler geometry, which contradict the SAR observation model and are thus considered errors. Some of the processing effects only occur for specific SAR imaging modes. With the future use of highly sophisticated imaging modes involving digital beam forming techniques (Villano et al., 2014), the investigation of such effects will become even more important and challenging.

From a hardware point of view, the following effects have been encountered so far:

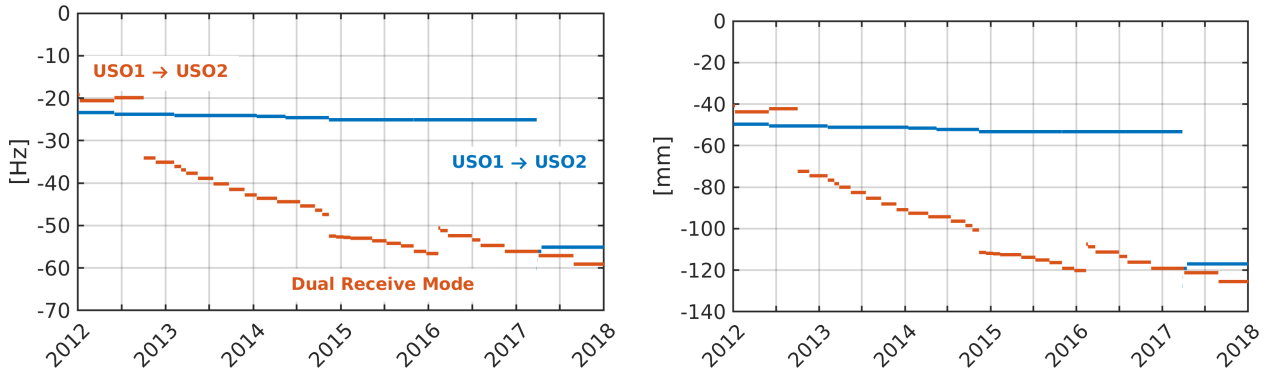

(a) A/D converter frequency updates **(b)** Impact on measured ranges

Fig. 2.4: Temporal progression of the A/D converter frequencies for TerraSAR-X (blue) and TanDEM-X (red) showing the aging of the ultra stable oscillator (USO). Frequency updates with respect to the nominally specified A/D converter frequency (a) and the equivalent changes in the range observations (b). Both satellites are now operating on the backup USOs. During 2015, TanDEM-X was temporarily switched to dual receive mode that altered the payload ambient temperature.

- **Oscillator drift:** Like other oscillators driving precise clocks and signal electronics, the ultra stable oscillator (USO) of a SAR payload experiences long-term aging effects, which change the nominal frequency and thus the overall timing system. Without the monitoring and updating of the frequency, long-term drifts will become visible in the range measurements if the nominal frequency is retained throughout mission lifetime (see Fig. 2.4). For TerraSAR-X, the frequency is verified with dedicated calibration data takes. The instrument performs a continuous receive-only acquisition that covers more than 10 minutes in orbit, for which the duration measured with the USO is compared to the duration defined by the pulse per second (PPS) of the on-board GPS (Balss et al., 2014). The procedure is applicable to any other SAR mission employing GNSS for absolute timing. Deviations of 23 Hz and 38 Hz with respect to the nominal 329.65 MHz sampling frequency of the analog to digital converters, which are governed by the USOs, were found during the first evaluation of TSX and TDX carried out in August 2013 (Balss et al., 2014). The update in the frequencies shifted the range measurements by about 50 mm and 80 mm as shown in Fig. 2.4b. Consequently, the USOs of TSX and TDX are now monitored on a regular basis, and their values are updated if the deviation is larger than 1 Hz (equivalent to about 2 mm).

- **Absolute time synchronization:** For modern SAR satellites, absolute time (e.g., Coordinated Universal Time UTC) on board the spacecraft is usually given by a GNSS receiver as a PPS, which is used to time tag the radar echoes controlled by the USO. The quality of this link determines the azimuth observation accuracy because, after completion of image formation, the zero-Doppler azimuth time is computed and annotated by the processor based on these time tags (section 2.1). GNSS receivers can provide a real-time realization of the UTC of 1 µs or better (Teunissen and Montenbruck, 2017), which is equivalent to 7 mm in azimuth when assuming a velocity of 7500 m/s for a SAR satellite in low Earth orbit. For TerraSAR-X, however, the implementation of the link is only equivalent to 18.6 µs, introducing an error of up to ±6.5 cm (P-I). A mitigation was therefore put in place, which combines the limited time tags during one PPS with the highly accurate interval information of the PRF of the SAR (Balss et al., 2014). Theoretically, this restores the UTC to better than 1 µs and the experimental results confirm the improvement by an overall azimuth error of ±2 cm (P-V). Other SAR satellite providers

have not disclosed this information for the SAR instruments, but it is expected that their level of synchronization is at best similar to the original implementation of TerraSAR-X.

- **Electronic delays:** The circuits of the SAR electronics and the cables connecting devices and antenna elements introduce small signal delays, which cause shifts in the range and azimuth measurements. Although the SAR instrument is precisely characterized and tested on ground before launch, the final estimation of these delays is performed as part of the geometrical calibration during the commissioning of the satellite (Schwerdt et al., 2010). Using CRs with known positions distributed across the swath, the range and azimuth values inferred from the orbit are compared with the measurements of the SAR instrument. After removing the known errors listed in Eq. 2.9, the average offset (t_e, τ_e) is computed from the residuals and the values are introduced into the SAR processor as calibration constants to center the measurements. Because of this experimental calibration approach, the calibration constants do not only include the electronic delays but also any other biases of the overall SAR system. Therefore, they have to be re-determined if elements of the observation model, e.g the atmospheric corrections, are modified. In the case of TerraSAR-X, an average range delay is already considered by the TMSP. It is tailored to a simplified atmospheric path delay correction and distributed with the products together with the azimuth delay calibration constant (Schwerdt et al., 2010). Both the range delay and the azimuth delay had to be refined because of the extensions of the SAR observation model (P-V). For Sentinel-1, the IPF applies the delays as specified in the applicable instrument auxiliary data file (Piantanida, 2017). This will require modifications to match the improved SAR observation modelling (P-III).

The effects introduced by the spectral SAR processing methods are ideally compensated for when generating the image from the raw SAR data, because all the parameters required to rectify image and time annotation for the zero-Doppler geometry are available at this stage. Furthermore, the spectral methods used to generate the image offer efficient means to correct the effects with minimal computational burden (P-III). This approach is pursued by the TMSP of TerraSAR-X, while in the case of the Sentinel-1 IPF processor, the computation needs to be performed by the user in post-processing. In principle, the corrections could also be implemented to the IPF, but the changes would break the continuity of the interferometric stacks if the archived data is not reprocessed. It was therefore decided to keep the IPF unchanged and to document the correction methods for the post-processing. Three different effects have to be taken into account (for the details see P-III):

- **Bistatic azimuth effects:** The movement of a low Earth SAR satellite between pulse transmission and reception of the radar echo approximately amounts to 30-40 m. This quasi-bistatic situation is commonly neglected in digital SAR processing when focussing the raw image data with spectral methods that require a 2-D data arrangement for fast time τ and slow time t (Cumming and Wong, 2005). In reality, both timings are strictly interdependent, but the processor inserts the sampled echo data into a data matrix using only the single receive time event for each echo which is derived from the PPS of the GNSS receiver. Therefore, neither the raw data arrangement nor the raw data timing annotations account for the bistatic situation. This is equivalent to the stop-and-go approximation: it is assumed that the satellite stops during transmission and reception of a single pulse and only moves after each event. The stop-and-go approximation is beneficial for efficient SAR image processing, but the implications have to be carefully considered in order to generate SAR images of rigorous zero-Doppler geometry with orthogonal (t, τ) annotations (see P-III). The TMSP accounts for both the raw data arrangement and the timing annotation of the stop-and-go approximation, whereas the Sentinel-1 IPF only applies a simple shift (referred to as "bulk correction") to define the azimuth timing annotation. This is sufficient to meet the mission geolocation requirements of 7 m (Bourbigot et al.,

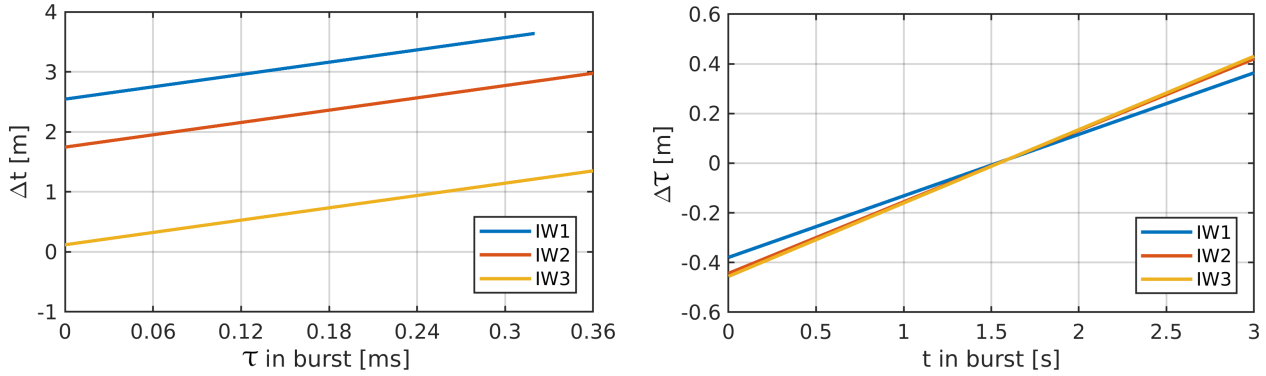

(a) Bistatic azimuth correction, Eq. 2.10 **(b)** Range correction for Doppler shifts, Eq. 2.11

Fig. 2.5: Post-processing corrections for the IPF-annotated timings of Sentinel-1 IW products across the subswaths IW1, IW2, and IW3. The τ=0.36 ms and t=3 s mark the average extent of a single IW-burst.

2015), but leads to sub-pixel distortions and shifts of 2-4 m in the azimuth measurements with Sentinel-1 IW products (Fig. 2.5a). Therefore, the correction of the stop-and-go artefacts in Sentinel-1 data requires an additional post-processing of the provided t_{IPF} (P-III [Eq. 20]):

$$t_{zero-Doppler} = t_{IPF} + \frac{\tau_{mid}}{2} + \frac{\tau}{2} - rank \cdot \Delta t_{PRI} \tag{2.10}$$

The τ_{mid} denotes the fast time for the middle of the central swath (IW2 or EW3, see section 2.2), the *rank* is the number of travelling pulses, and Δt_{PRI} is the pulse repetition interval (PRI; inverse of the PRF). The correction changes significantly when computed across the entire IW swath (see Fig. 2.5a), as the Sentinel-1 sensor adapts the *rank* and the PRF according to the slant range distance of the swaths IW1, IW2 and IW3.

- **Doppler shifts in range:** The movement of the satellite also affects the range measurements, because the transmitted pulses experience the frequency shift of the Doppler effect. While progression of the sensor along the trajectory defines the synthetic aperture in azimuth direction and thus the fundamental principle of SAR (Curlander and McDonough, 1991; Cumming and Wong, 2005), the actual Doppler shift associated with the velocity is usually ignored by the processing. This is also because the effect cancels almost completely for SAR modes with azimuth spectra close to zero-Doppler, e.g., stripmap SAR with zero-Doppler steering. However, for SAR modes like ScanSAR or TOPS, which generate data with large Doppler centroid variations across the bursts (Cumming and Wong, 2005; de Zan and Guarnieri, 2006), the impact of the Doppler shift becomes significant, especially towards the edge of the bursts where the Doppler effect is largest. During spectral range compression the Doppler shift causes a proportional shift in the location of the focussed peak. This cannot be handled by the matched filter, because at this stage the pulse echo data contain all the superimposed Doppler shifts of the entire swath. Therefore, the shifts have to be removed later in the process when the data is represented in the spectral azimuth domain. For Sentinel IW data, the effect is not considered by the IPF, and the Doppler-induced shifts become as large as 0.4 m towards the edge of the bursts (P-III and Fig. 2.5b). The post-processing correction requires the reconstruction of the Doppler centroid f_{DC} depending on the location (t, τ), which is not a straightforward computation because of the

additional beam steering carried out in the TOPS mode. Once the Doppler centroid frequency f_{DC} is known, the correction is added to the fast time generated by the IPF (P-III [Eq. 27]):

$$\Delta\tau(t,\tau) = \frac{f_{DC}(t,\tau)}{K_r}, \tag{2.11}$$

where K_r is the frequency modulation (FM)-rate of the range chirp as annotated in the products. Because of the adaptation of the antenna steering rate and the varying azimuth FM-rate, the slope of the correction changes across the IW subswaths (see Fig. 2.5b).

- **Shifts due to FM-rate mismatch:** Spectral focussing of the azimuth signal requires the reconstruction of the Doppler FM-rate which is driven by the sensor-to-ground geometry. While the change with distance (range) is generally modelled with sufficient detail when defining the matched filter, the effective velocity parameter underlying the FM-rate computation is usually kept constant during the processing of large azimuth blocks. These blocks can comprise up to several seconds in azimuth dimension (e.g., the 3 s burst size of Sentinel-1 TOPS; Piantanida, 2017). In the case of SAR imaging modes with azimuth spectra centered close to zero-Doppler, the effect of the mismatch (also called quadratic phase error; Cumming and Wong, 2005) is mainly a blurring of the image (defocussing), whereas for TOPS and other modes with large Doppler centroids the outcome is a shift in azimuth direction (Cumming and Wong, 2005; Rodriguez-Cassola et al., 2015). For Sentinel-1 IW products, azimuth shifts of up to 1 m were found when the CRs is located at the very edge of a burst and the height in the computation of the FM-rate deviates on the order of 1000 m. This was already theoretically predicted in Rodriguez-Cassola et al. (2015). Similar to the correction of the Doppler shifts in range, the correction of the FM-rate mismatch in azimuth requires the computation of the Doppler centroid $f_{DC}(t,\tau)$. Furthermore, it requires the computation of the FM-rate $k_{a,IPF}$ used by the IPF and the true FM-rate $k_{a,geo}$ given by an accurate DEM. The correction accounts for the mismatch in the FM-rates and has to be subtracted from the azimuth time annotated to the Sentinel-1 product (P-III [Eq.30]):

$$\Delta t = f_{DC}(t,\tau) \cdot \left(\frac{1}{-k_{a,IPF}} - \frac{1}{-k_{a,geo}} \right). \tag{2.12}$$

Strictly speaking, also relativistic effects (Einstein, 1907) play a role in the SAR measurements: the Shapiro delay that modifies the time of propagation for range observations (Petit and Luzum, 2010; Combrinck, 2013), the effect of time dilation of a clock (oscillator) moving in orbit (Combrinck, 2013), and the gravitational redshift due to the gravitational potential difference between satellite altitude and Earth surface level (Combrinck, 2013). For a SAR payload in low Earth orbit, the combined effects amount to less than 1 mm for the measured ranges and are thus negligible. However, for the on-board GNSS the compensations for time dilation and gravitational redshift are of crucial importance and need to be considered in the processing the GNSS observations (Teunissen and Montenbruck, 2017).

2.3.4 Atmospheric Path Delays

Electromagnetic signals travelling through the Earth's atmosphere experience propagation effects that have to be accounted for when converting a signal travel time to a distance using the speed of light in vacuum (see Eq. 2.5). For space geodetic techniques, the removal of these effects is critical to ensure consistent geometric observations on a global spatio-temporal scale and among the different observation techniques using optical signals (SLR) and microwave signals (GNSS, VLBI, DORIS).

Therefore, the study of the propagation effect and their correction in observations is well established in the field of geodesy and a comprehensive summary can be found in Böhm and Schuh (2013).

The carrier signals of currently operating spaceborne SAR sensors range from L-band (1.2 GHz, e.g., ALOS-2; Suzuki et al., 2009) to X-band (9.65 GHz, e.g., TerraSAR-X). This is also the frequency regime covered by GNSS (L-band; Teunissen and Montenbruck, 2017) and VLBI (X-band and S-band; Schuh and Böhm, 2013). This allows straightforward adaptation of the geodetic correcting methods for SAR, and the usage of atmospheric products derived from the geodetic observation networks (P-I; P-III; P-V).

The propagation of a microwave signal through the Earth's atmosphere is driven by the refractive index of the medium, which causes the group velocity of the modulated signal (e.g., GNSS ranging codes or phase-coded SAR pulses) to be less or equal the speed of light in vacuum (Alizadeh et al., 2013; Nilsson et al., 2013). When measuring the time of propagation of microwave signals, the refractive index of the atmosphere causes a time delay and therefore an increase in the distance as inferred from Eq. 2.5. In accordance with the geodetic methods, the atmospheric delay is divided into the contributions stemming from the neutral part (referred to as troposphere[1], about 0-100 km altitude) and the ionized part (termed ionosphere, about 60-1600 km altitude) (Böhm and Schuh, 2013). This separation was already introduced for SAR by the range error model using $\Delta\tau_{tro}$ and $\Delta\tau_{ion}$ (see Eq. 2.9).

Different methods to remove the ionospheric and tropospheric delays in the SAR range observations were studied in the publications P-I, P-III, and P-V. The following paragraphs summarize the theory and the usage of these methods.

- **Troposphere:** For the troposphere, the refractive index is driven by the gas composition of the atmosphere and can be modelled as a function of temperature, pressure, and humidity (Essen and Froome, 1951; Nilsson et al., 2013). Regarding microwave signals of up to 15 GHz, the refractive index and the corresponding tropospheric delay can be considered independent of the frequency (Hofmann-Wellenhof et al., 2008; Nilsson et al., 2013); thus the delay is identically observed in all the microwave techniques including the SAR.

  The impact of the tropospheric delay converted to units of distance is on the order of 2.4 m (Fig. 2.6a) and may become as large as 4.2 m when scaled for spaceborne SAR observations with an incidence angle of approximately 55 ° (see section 2.2). The modelling of the tropospheric delay in observations benefits from the fact that the refractive index (or refractivity when expressed in units of ppm) can be decomposed into hydrostatic and wet parts (Nilsson et al., 2013), defining the hydrostatic and wet path delays, respectively. The hydrostatic delay comprises about 90 % of the total delay and is purely pressure driven (Eq. 40; Nilsson et al., 2013). This allows robust modelling using surface pressure data (Saastamoinen, 1973; Davis et al., 1985) and results in a direct correlation with Earth topography (Fig. 2.6a). The wet delay is driven by water vapor and is much more difficult to model because of the water vapor's strong spatio-temporal variation, particularly so in the tropical regions. Therefore, geodetic techniques like GNSS and VLBI rely on *a priori* modelling of the hydrostatic delays and the estimation of the wet delays from the observations (Petit and Luzum, 2010; Böhm and Schuh, 2013).

  The estimation requires a reduction of the slant range observations for consistent path delays in zenith direction, which is accomplished by dedicated mapping functions for the hydrostatic and wet delays (Böhm and Schuh, 2013). The Vienna Mapping Function (VMF) marks the latest development in tropospheric mapping functions (Böhm et al., 2006; Landskron and Böhm, 2018).

[1] Strictly speaking this also includes the stratosphere, but the term troposphere is commonly used in geodesy for the neutral atmospheric delay (Nilsson et al., 2013).

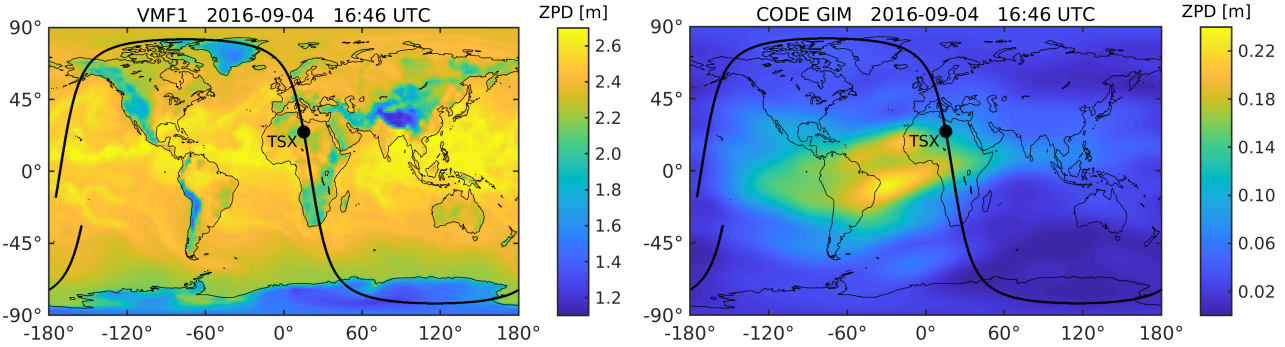

(a) Total tropospheric zenith delay **(b)** Ionospheric zenith delay in X-band (9.65 GHz)

Fig. 2.6: Global distribution of the total tropospheric delay given by the VMF (a) and the ionospheric delay given by the vertical TEC maps of CODE (b) at September 4^{th}, 2016. The ground track of TerraSAR-X (black) covers ± 45 minutes with respect to the satellite location marked at 16:46 UTC.

It is based on integrated path delays computed from the operational Integrated Forecast System (IFS) of the European Centre for Medium-Range Weather Forecasts (ECMWF) weather model which are used to derive the coefficients of the mapping functions. Both the integrated path delays and the coefficients of the VMF are provided as products with global coverage (resolution 2 ° x 2.5 °; longitude x latitude) and a six hours temporal sampling following ECMWF (00h, 06h, 12h, 18h UTC)[1]. The combination of the zenith integrated path delays and the VMF already offers an efficient method to directly correct the tropospheric path delays on a global scale with an accuracy on the order of 2 cm (Kouba, 2007). Figure 2.6a shows an example of the global distribution of the total tropospheric zenith path delay as provided by the VMF. The method was used to correct the SAR data for the study presented in P-III.

More accurate means of correcting the tropospheric delay are given by the GNSS-based estimates of the total delay that use the hydrostatic path delay of the VMF as a background model. The estimation is performed on a daily basis as a service for global or regional permanent GNSS networks, e.g., the network of the IGS (Villiger and Dach, 2018) or the European EUREF network (Bruyninx et al., 2017). In the case of the IGS solution computed by U.S. Naval Observatory, the zenith delays are estimated with a 5 minute temporal resolution along with a gradient model accounting for the anisotropy (Byram et al., 2011). The error as inferred from the least squares solution is annotated in the IGS products and is usually better than 5 mm. In the long-term studies of TerraSAR-X carried out for the CRs at the different geodetic observatories (P-I; P-IV; P-V), these products were determined to be the most accurate source for correcting the tropospheric path delay in SAR range observations, which makes them the preferred correction method when performing the geometrical calibration of a SAR system.

As an alternative to the very precise but station-based solutions of permanent GNSS and the zenith integration of weather models with additional slant range mapping, which can lead to systematic errors when using a smoothed orography (Zus et al., 2015), there are also ray-tracing techniques that aim for the direct slant path integration of the observation geometry (Nilsson et al., 2013). These computationally expensive methods are studied in detail for interferometric SAR methods (e.g., Hobiger et al., 2010; Cong et al., 2018), and are presently considered the most suitable approach to correct the tropospheric delay in SAR imaging geodesy for global application. The comparison of different correction techniques, however, was not in the scope

[1]Vienna University of Technology: http://ggosatm.hg.tuwien.ac.at/delay.html (accessed October 2018)

of this thesis and the publications PI-PVI relied either on the GNSS-based IGS products or the VMF product. The experiments with the CRs at the geodetic observatories made use of the readily available IGS products, whereas the study at the Australian CR array involved the VMF product because there is no nearby IGS reference station.

- **Ionosphere:** The refractive index of the ionosphere depends on the frequency and is described by the electron density which accounts for the dispersive nature of the medium (Eq. 20; Alizadeh et al., 2013). The frequency dependency needs to be considered to correct the path delay in the observations of different SAR payloads. There is also a difference in the group velocity (applying to the time-of-flight observations) and the phase velocity (applying to phase-based observations) caused by the dispersion (e.g., Hofmann-Wellenhof et al., 2008), but the phase velocity can be neglected for this work as it is only concerned with the SAR timing observations. A description of the ionospheric effects in phase-based SAR interferometry is found in Gomba et al. (2017). While the geodetic microwave techniques use two or more carrier frequencies that can be combined to eliminate the impact of the ionosphere, the single carrier frequency of SAR requires external sources like physical models (e.g., the international reference ionosphere model IRI; Bilitza and Reinisch, 2008) or the ionospheric maps inferred from GNSS (Hernández-Pajares et al., 2009).

  The vertical extent of the ionosphere up to approximately 1600 km altitude allows a single GNSS receiver to probe a much larger region (about 3000 km in diameter; Schaer, 1999), and therefore the global IGS network can be used to measure the global electron distribution. The results are global ionospheric maps with a resolution of 5 ° x 2.5 ° x 2h (latitude x longitude x time) of the vertically condensed total electron content (TEC) that are made available as daily data cubes dating back as far as 1998 (Hernández-Pajares et al., 2009). Spatio-temporal interpolation of the vertical TEC for the time and location of the SAR measurement and the conversion to slant range delay enables the correction for the ionospheric delay on a global scale (Fig. 2.6b). In the studies with TerraSAR-X and Sentinel-1 (P-I; P-III), the TEC solution computed by Center for Orbit Determination in Europe (CODE) was used, because the applied least squares approach also provides estimated RMS maps to assess the precision (Schaer, 1999; Mannucci et al., 1998; Dach et al., 2018).

  Across the different frequencies used in SAR, the impact of a typical TEC of 20 TEC units (1 TECU = 10^{16} electrons) results in zenith delays of 0.09 m (X-band), 0.32 m (C-band), and 5.60 m (L-band). The ionization of the upper atmosphere is driven by solar radiation, which means not only diurnal and seasonal variations, but also a significant increase of the effect (up to a factor of 2) during the periods of maximum solar activity (i.e. the 11.1 years solar cycle; Böhm et al., 2013). Therefore, even for a SAR measurement series in X-band the variability of the ionospheric delay can become as large as the tropospheric delay variation related to water vapor. For C-band or L-band SAR observations, the ionosphere becomes the dominating source of error. The TEC maps offered by CODE have an estimated RMS of 0.5 TECU or better, but for regions only sparsely covered by the IGS network (central and northern Africa, central Asia) the error may increases to several TECUs (Mannucci et al., 1998; Hernández-Pajares et al., 2009; Teunissen and Montenbruck, 2017). An error of 2 TECUs translates into uncertainties of 0.008 m, 0.032 m, and 0.560 m for the ionospheric path delay in X-band, C-band, and L-band, respectively. For X-band, this is acceptable, and also for the presently best achievable ranging accuracy in C-band with Sentinel-1, the impact is on par with the other errors. However, for L-band SAR different methods should be envisaged, e.g., the split-spectrum techniques as developed for SAR interferometry (Gomba et al., 2016, 2017).

  While the medium Earth orbits of GNSS allow the observation of the total integrated TEC, the low Earth orbits of SAR missions like TerraSAR-X and Sentinel-1 are still within the ionized

region of approximately 1600 km altitude considered as ionosphere (Böhm et al., 2013). The 3-D structure and the dynamics of the ionosphere exhibit considerable geospatial variations (van Barneveld et al., 2009). To account for the situation in a first approximation, a constant scaling factor of 75 % was introduced for TerraSAR-X (P-I; P-V), which is based on IRI profile analysis and the evaluation of TerraSAR-X on-board GPS data (Balss et al., 2012; Gisinger, 2012). For the higher orbit altitude of Sentinel-1 (see section 2.2), a similar factor of 90 % is proposed in P-III. The simple scaling factors have the advantage of preserving the smooth continuous structure of the ionospheric TEC maps. Further improvements could be achieved in future by adapting the factors with respect to latitude and the temporal variations as inferred from physical ionospheric models.

The correction of the ionosphere in the SAR ranges, as presented in the publications P-I to P-VI, considers the first order ionospheric effect, which follows the recommendation given in the IERS conventions for high-frequency techniques such as VLBI (and thus X-band SAR; TerraSAR-X). But even for observations in C-Band, the combined second and third order terms do not exceed a few millimeters (Petit and Luzum, 2010, Table 9.2). Aside from the path delay in range, the ionosphere can also introduce shifts in azimuth if there is a horizontal TEC gradient on the order of 0.001 TECU/km along the synthetic aperture of a target (Gomba et al., 2017). The shift is stated in the azimuth error (Eq. 2.9) but it has not been considered in the processing so far. For mid-latitude and high-latitude test sites, the impact of a 0.001 TECU/km gradient amounts to 5 mm and 10 mm for TerraSAR-X and Sentinel-1, respectively, as computed from the equation given in Gomba et al. (2017). This is less than the presently achievable azimuth observation accuracy of both missions (2 cm and 26 cm, P-III; P-V). Near the geomagnetic equator, the local gradients can increase by factors of 5 to 10 (Fig. 2.6b). Therefore, the effect will become significant when analyzing SAR data at a global scale, and it should be considered in future implementations, especially if other azimuth error sources (along-track orbit accuracy, on-board timing control) are further reduced.

2.3.5 Solid Earth Displacements

The solid Earth undergoes periodic and secular deformations, which are directly and indirectly related to the tidal dynamics as well as geodynamic processes like plate tectonics, hydrological cycles or diurnal heating of the Earth's atmosphere (Petit and Luzum, 2010). In accordance with the IERS conventions and the methods of the ITRF (Petit and Luzum, 2010), all periodic signals should be corrected from reference markers in order to obtain coordinates that can be specified at any epoch within the ITRF by additionally estimating linear station velocities. This procedure lies at the core of the ITRF determination (Altamimi et al., 2016), and in turn these ITRF coordinates enable the orbit determination and validation with ground-based or space-based observations (SLR, DORIS, GNSS; Combrinck, 2010; Teunissen and Montenbruck, 2017). Consequently the SAR observation modelling has to comply with these methods to determine 3-D coordinates or to perform the geometrical calibration based on CRs with known ITRF coordinates. In accordance with Petit and Luzum (2010), the target coordinate at the epoch of a SAR observation t_a can be stated as follows:

$$\mathbf{X}_T(t_a) = \mathbf{X}_T(t_0) + \dot{\mathbf{X}}_T \cdot (t_a - t_0) + \sum \Delta\mathbf{X}(t_a), \tag{2.13}$$

where $\mathbf{X}_T(t_0)$ is the position in ITRF at a selected reference epoch t_0 (e.g., the fundamental epoch of an ITRF solution or the epoch of the first SAR observation in given data series), $\dot{\mathbf{X}}_T$ denotes the linear station velocity in the ITRF, and $\Sigma\Delta\mathbf{X}(t_a)$ comprises the non-linear displacement models evaluated at the epoch of the observation.

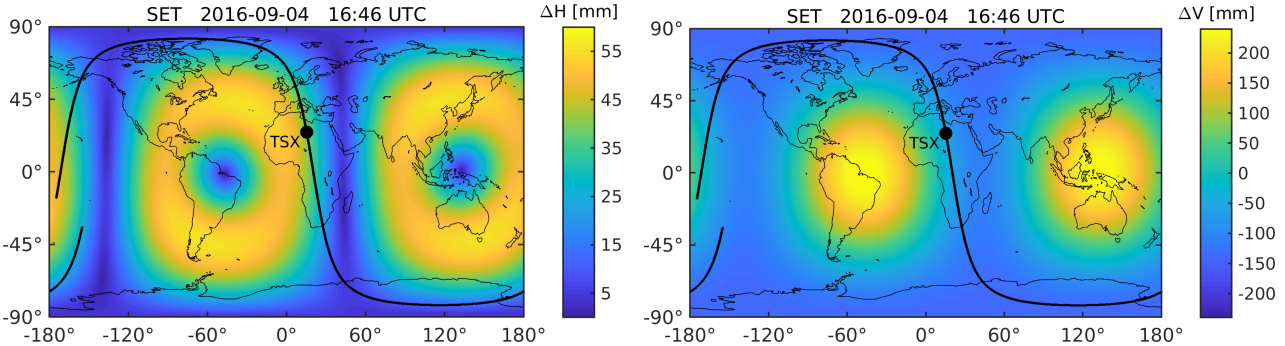

(a) Local horizontal displacement $\sqrt{\Delta_n^2 + \Delta_e^2}$ **(b)** Local vertical displacement Δ_v

Fig. 2.7: Global solid Earth tide deformation at September 4^{th}, 2016 (close to a new Moon constellation). The ground track of TerraSAR-X (black) covers ± 45 minutes with respect to the satellite location marked at 16:46 UTC.

The dominant periodic displacement signals are caused by the direct tides of Sun and Moon, which lead to diurnal deformations of the Earth's crust on the order of 60 mm in horizontal and 250 mm in vertical direction (Fig. 2.7). These solid Earth tides (SET) vary with the constellation of Sun, Earth and Moon. The modulation of the bulge structure is governed by the approximately 28 days revolution period of the Moon. Because of the sun-synchronous dusk-dawn orbit configuration, TerraSAR-X and Sentinel-1 observations experience the maximum negative deformation during new Moon (or full Moon) constellations (Fig. 2.7b). For half Moon constellations, the sensed deformation is positive as the ground track will cross the local maximum of the Moon tide. Therefore, long-term SAR measurements from sun-synchronous orbits nearly include the entire signal amplitude of the SET. The conventional model to compute the SET deformation is described in full detail in the IERS conventions and contains all the signal contributions that exceed the 1 mm level (Petit and Luzum, 2010). Note that the model also removes the permanent crust deformation of the tides, resulting in conventional tide free coordinates. The additional correction for restoring this permanent deformation is not considered for SAR, which is in line with the ITRF and the space geodetic techniques (Petit and Luzum, 2010).

Further periodic solid Earth deformation signals are: the ocean tidal loading caused by the tidal redistribution of the Earth's water masses weighing on the coastal regions, the atmospheric tidal loading caused by the daily temperature variation in the atmosphere, and the back-coupling effects of momentum changes of the Earth's rotational axis. The latter has a direct effect on the solid Earth (pole tides) as well as an indirect effect through the ocean water masses (ocean pole tide loading). The horizontal and vertical magnitudes of these effects are listed in Tab. 2.2. The computation and the underlying background data can be found in the IERS conventions (Petit and Luzum, 2010). Furthermore, there are non-tidal deformation signals of continental hydrology and local weather, which are not yet part of the conventional corrections. Data driven models are available, e.g., for the atmospheric pressure loading (Petrov and Boy, 2004), but for the latest ITRF 2014 solution it was decided to estimate seasonal signals rather than to introduce additional models (Altamimi et al., 2016). Finally, there are the secular deformations mainly related to plate tectonics, which are either estimated from long-term observation or substituted for *a priori* values. The values can be obtained from the nearest ITRF reference marker located on the same tectonic plate or computed from the tectonic models inferred from the ITRF solutions (e.g., Altamimi et al., 2017).

The currently achievable SAR observation accuracy mainly requires the correction of the SET. Depending on the observation site, the ocean tidal loading also has to be considered, see for instance

Tab. 2.2: Order of magnitude of the solid Earth effects as given by the IERS conventions Petit and Luzum (2010).

Solid Earth Effect	**Horizontal** [mm]	**Vertical** [mm]
Solid Earth tides	±60.0	±250.0
Ocean tidal loading[1]	±10.0	±50.0
Pole tides	±1.5	±6.0
Atmospheric tidal loading	±0.2	±1.5
Ocean pole tide loading	±0.3	±0.5
Secular trends, up to	100 mm/y	15 mm/y

[1] Based on the FES2004 Lyard et al. (2006)

GARS O'Higgins on the Antarctic peninsula (P-I). Nevertheless, all the conventional models were implemented and used in studies presented in the publications, along with experimental testing of the atmospheric pressure loading and *a priori* plate tectonics from nearby ITRF reference markers.

2.4 Linearization of SAR Observation Model and Least Squares Solution

The solution of the SAR range-Doppler equations (Eq. 2.4 and 2.6) represents an optimization problem that involves observation errors as well as several unknown parameters. After the removal of any remaining artefacts related to SAR processing and the correction of the atmospheric delays and the geodynamic displacements by introducing *a priori* information, there still remain unknown biases in the range and azimuth observations. These are mainly the electronic delays and the potential bias contributions from the data reduction models, but also the random errors (noise; uncertainties of corrections), which have to be accounted for during the observation analysis. In addition, the target coordinates have to be resolved when using the SAR for 3-D positioning. By introducing the coordinate model for the target as stated in Eq. 2.13, the dependencies within the range-Doppler equations in zero-Doppler configuration can be given as:

$$f_r(\tau_r, \Delta\tau_e, \mathbf{X}_S(t_a, \Delta t_e), \mathbf{X}_T(t_0), \dot{\mathbf{X}}_T) = 0 \tag{2.14}$$

$$f_a(\mathbf{X}_S(t_a, \Delta t_e), \dot{\mathbf{X}}_S(t_a, \Delta t_e), \mathbf{X}_T(t_0), \dot{\mathbf{X}}_T) = 0. \tag{2.15}$$

A method for the rigorous solution of such type of optimization problems under the L_2-norm is outlined by the *adjustment of conditions with additional parameters* (Mikhail and Ackermann, 1976). Unlike GNSS and SLR which are based on the simpler range equation (Combrinck, 2010; Teunissen and Montenbruck, 2017), the observation of the Doppler in SAR requires this general least squares approach in order to derive a solution that can make use of the SAR azimuth observable confined to the orbit trajectory. Afterwards, the linearized equations can be transformed to an ordinary Gauss-Markoff model (e.g. Koch, 1999). This reduces the computational effort and improves the numerical stability of the implementation.

Following Mikhail and Ackermann (1976), f_r and f_a are interpreted as condition equations demanding a zero result which fit the linear scheme

$$\mathbf{B} \cdot (\mathbf{l} + \mathbf{v}) + \mathbf{A} \cdot \mathbf{x} = \mathbf{0}. \tag{2.16}$$

The symbols in Eq. 2.16 comprise the observations $\mathbf{l}$ for a number of n images, the observation residuals $\mathbf{v}$, and the design matrix $\mathbf{A}$ of the unknown parameters $\mathbf{x}$:

$$\begin{aligned}\mathbf{l} &= \begin{bmatrix}\tau_{r_1} & t_{a_1} & \dots & \tau_{r_n} & t_{a_n}\end{bmatrix}^T \\ \mathbf{v} &= \begin{bmatrix}v_{r_1} & v_{a_1} & \dots & v_{r_n} & v_{a_n}\end{bmatrix}^T \\ \mathbf{x} &= \begin{bmatrix}\Delta\tau_e & \Delta t_e & x_T & y_T & z_T & \dot{x}_T & \dot{y}_T & \dot{z}_T\end{bmatrix}^T.\end{aligned} \tag{2.17}$$

With the substitution of $\mathbf{B} \cdot \mathbf{l} = \mathbf{w}$ in Eq. 2.16, the final scheme for the *adjustment of conditions with additional parameters* is obtained:

$$\mathbf{B} \cdot \mathbf{v} + \mathbf{A} \cdot \mathbf{x} + \mathbf{w} = \mathbf{0}, \tag{2.18}$$

where the vector $\mathbf{w}$ contains the contradictions. By using the contradictions to evaluate the state of the system, both the observation residuals and the parameters can be jointly resolved by introducing the L_2-norm as additional boundary condition for the residuals: $\mathbf{v}^T\mathbf{P}\mathbf{v} \rightarrow \min$. The $\mathbf{P}$ is the weight matrix that corresponds to the inverse of the variance-covariance matrix of the observations, i.e. $\mathbf{P} = \mathbf{Q}^{-1}$. A solution of Eq. 2.18 by means of Lagrange multipliers is readily possible (Mikhail and Ackermann, 1976). However, the given case of the SAR range-Doppler equations offers an alternative solution strategy, which avoids the computational inversion of $\mathbf{BQB}^T$ otherwise needed to estimate the $\mathbf{x}$ in the generalized approach.

The definition of Eq. 2.18 for the range-Doppler equations requires their linearization and thus the partial derivatives with respect to the observations and the unknown parameters:

$$\begin{aligned}\begin{bmatrix}\frac{\partial f_r}{\partial \tau_r} & \frac{\partial f_r}{\partial t_a} \\ \frac{\partial f_a}{\partial \tau_r} & \frac{\partial f_a}{\partial t_a}\end{bmatrix} \cdot \begin{bmatrix}v_r \\ v_a\end{bmatrix} + \begin{bmatrix}\frac{\partial f_r}{\partial \Delta\tau_e} & \frac{\partial f_r}{\partial \Delta t_e} & \frac{\partial f_r}{\partial \Delta x_T} & \frac{\partial f_r}{\partial \Delta y_T} & \frac{\partial f_r}{\partial \Delta z_T} & \frac{\partial f_r}{\partial \Delta \dot{x}_T} & \frac{\partial f_r}{\partial \Delta \dot{y}_T} & \frac{\partial f_r}{\partial \Delta \dot{z}_T} \\ \frac{\partial f_a}{\partial \Delta\tau_e} & \frac{\partial f_a}{\partial \Delta t_e} & \frac{\partial f_a}{\partial \Delta x_T} & \frac{\partial f_a}{\partial \Delta y_T} & \frac{\partial f_a}{\partial \Delta z_T} & \frac{\partial f_a}{\partial \Delta \dot{x}_T} & \frac{\partial f_a}{\partial \Delta \dot{y}_T} & \frac{\partial f_a}{\partial \Delta \dot{z}_T}\end{bmatrix} \dots \\ \cdot \begin{bmatrix}\Delta\tau_e & \Delta t_e & x_T & y_T & z_T & \dot{x}_T & \dot{y}_T & \dot{z}_T\end{bmatrix}^T + \begin{bmatrix}w_r \\ w_a\end{bmatrix} = \mathbf{0}\end{aligned} \tag{2.19}$$

All the partial derivatives are stated in full in the appendix of P-I and are thus not repeated here. The analytical derivatives of the azimuth are computed from a short-arc orbit interpolation model, which can be obtained from a least squares fit of the orbit state vectors annotated to the SAR image product (see section 2.3.2). Ordinary polynomials of the shape

$$\mathbf{X}_S = \sum_{i=0}^{N} \begin{bmatrix}a_i \\ b_i \\ c_i\end{bmatrix} \cdot (t_a + \Delta t_e)^i \tag{2.20}$$

are used to model the short orbit arcs covering the synthetic aperture. A degree of $N = 6$ was found to be sufficient when comparing the interpolation results from the annotated orbit data with 10 s sampling and POD solutions using an increased sampling of 1 s. The derivatives with respect to the azimuth t_a contained in the $\mathbf{B}$ matrix are computed by applying the chain rule:

$$\begin{aligned}\frac{\partial f_r}{\partial t_a} =& \frac{\partial f_r}{\partial x_S} \cdot \frac{\partial x_S}{\partial t_a} + \frac{\partial f_r}{\partial y_S} \cdot \frac{\partial y_S}{\partial t_a} + \frac{\partial f_r}{\partial z_S} \cdot \frac{\partial z_S}{\partial t_a} \\ \frac{\partial f_a}{\partial t_a} =& \frac{\partial f_a}{\partial x_S} \cdot \frac{\partial x_S}{\partial t_a} + \frac{\partial f_a}{\partial y_S} \cdot \frac{\partial y_S}{\partial t_a} + \frac{\partial f_a}{\partial z_S} \cdot \frac{\partial z_S}{\partial t_a} + \frac{\partial f_a}{\partial \dot{x}_S} \cdot \frac{\partial \dot{x}_S}{\partial t_a} + \frac{\partial f_a}{\partial \dot{y}_S} \cdot \frac{\partial \dot{y}_S}{\partial t_a} + \frac{\partial f_a}{\partial \dot{z}_S} \cdot \frac{\partial \dot{z}_S}{\partial t_a}.\end{aligned} \tag{2.21}$$

Be aware that these derivatives are identical to the partial derivatives of the azimuth calibration $\partial f_r/\partial \Delta t_e$ and $\partial f_a/\partial \Delta t_e$ required in the design matrix $\mathbf{A}$.

For the parameters $\mathbf{x}$, the observation equations (two per image) are accumulated in $\mathbf{A}$, whereas the observation residuals v_r and v_a are independently defined for each equation, which leads to a quadratic block-diagonal structure in $\mathbf{B}$. In general, the inverse of quadratic block-diagonal matrix is equivalent to the inverse of the individual blocks (Mikhail and Ackermann, 1976). The inverse of the 2 by 2 blocks in $\mathbf{B}$ can be computed analytically. It is driven by the determinant which reads

$$\det(\mathbf{B}) = \frac{1}{\left(\frac{\partial f_r}{\partial \tau_r} \cdot \frac{\partial f_a}{\partial t_a} - \frac{\partial f_r}{\partial t_a} \cdot \frac{\partial f_a}{\partial \tau_r}\right)} = \frac{1}{\left(-\frac{c}{2} \cdot \frac{\partial f_a}{\partial t_a}\right)}. \tag{2.22}$$

The partial derivative $\partial f_a / \partial \tau_r$ is zero, the partial derivative $\partial f_r / \partial \tau_r$ is simply $-c/2$ (see Eq. 2.5), and the partial derivative $\partial f_a / \partial t_a$ is effectively the time derivative of the orbital state vector (see Eq. 2.21), which is non-zero. Hence it can be concluded that the inverse of $\mathbf{B}$ exists, which allows the transformation of the problem as follows:

$$\mathbf{v} + \underbrace{\mathbf{B}^{-1} \cdot \mathbf{A}}_{-\bar{\mathbf{A}}} \cdot \mathbf{x} + \underbrace{\mathbf{B}^{-1} \cdot \mathbf{w}}_{\bar{\mathbf{l}}} = \mathbf{0} \tag{2.23}$$

The Eq. 2.23 defines an ordinary Gauss-Markoff least squares adjustment

$$\bar{\mathbf{l}} + \mathbf{v} = \bar{\mathbf{A}} \cdot \mathbf{x} \tag{2.24}$$

that can be solved for the parameters $\hat{\mathbf{x}}$ and their corresponding variance-covariance matrix $\Sigma(\hat{\mathbf{x}})$ by using the well known least squares formalism (e.g., Mikhail and Ackermann, 1976):

$$\begin{aligned} \hat{\mathbf{x}} &= \left(\bar{\mathbf{A}}^T \cdot \mathbf{P} \cdot \bar{\mathbf{A}}\right)^{-1} \cdot \bar{\mathbf{A}}^T \cdot \mathbf{P} \cdot \bar{\mathbf{l}} \\ \Sigma(\hat{\mathbf{x}}) &= \left(\bar{\mathbf{A}}^T \cdot \mathbf{P} \cdot \bar{\mathbf{A}}\right)^{-1} \cdot \frac{\left(\bar{\mathbf{A}} \cdot \hat{\mathbf{x}} - \bar{\mathbf{l}}\right)^T \cdot \mathbf{P} \cdot \left(\bar{\mathbf{A}} \cdot \hat{\mathbf{x}} - \bar{\mathbf{l}}\right)}{2n - m}. \end{aligned} \tag{2.25}$$

The n denotes the number of available images and the m is the number of estimated parameters in $\mathbf{x}$. Because of the linearization, the solution has to be computed by iteration, which requires initial values for $\mathbf{x}$. The process is terminated once the additions to the parameter vector $\hat{\mathbf{x}}$ become negligible (sub-mm level). It is important to note that both the $\mathbf{B}$ and $\mathbf{A}$ matrix become updated during each iteration step. Regarding the initial values, the solution process and the overall method were found to be very robust. Even a coarse initialization of the target location using the approximately known center of the acquired SAR scenes achieves convergence after 4-5 iteration steps for SAR positioning.

The least squares solution of the SAR observation model enables the combination of arbitrary range and azimuth measurements of the same target across different SAR imaging modes and even across different SAR missions, which raises the question of how to define the weights in the $\mathbf{P}$ matrix. This aspect is already important for the range and azimuth observations themselves, as they have a different accuracy due to the in general non-square resolution of the SSC image products (see section 2.1) and the on-board time synchronization limiting the precision of the azimuth observation (see section 2.3.3). A frequently applied method to handle such differences between groups of observations is the variance component estimation (VCE) (Koch, 1999; Koch and Kusche, 2002). The VCE performs the estimation of data driven variances $\hat{\sigma}_i^2$ from the observation residuals for the observation groups as part of the iterative least squares solution process. After completing an iteration in the parameter estimation, the redundancies r_i of predefined observation groups i are inferred according to their contributions to the overall normal equation system. The redundancies are then used to scale the observation residuals of each group:

$$
\begin{aligned}
r_i &= n_i - \operatorname{trace}\left(\bar{\mathbf{A}}_i^T \mathbf{P}_i \bar{\mathbf{A}}_i (\bar{\mathbf{A}}^T \mathbf{P} \bar{\mathbf{A}})^{-1}\right) \\
\hat{\sigma}_i^2 &= \frac{(\bar{\mathbf{A}}_i \hat{\mathbf{x}} - \bar{\mathbf{l}}_i)^T \mathbf{P}_i (\bar{\mathbf{A}}_i \hat{\mathbf{x}} - \bar{\mathbf{l}}_i)}{r_i}.
\end{aligned} \tag{2.26}
$$

Finally, the $\mathbf{P}$ matrix becomes updated for the estimated variances $\hat{\sigma}_i^2$. This marks the start of next iteration.

Because of the statistical evaluation of the residuals, the usage of VCE requires a certain number of observations. Four images were found to give meaningful results, but at least 10 images are recommended to obtain a more reliable representation of the observation precision. Once this requirement is fulfilled, the VCE is very effective because the independent range and azimuth observations as stipulated by the zero-Doppler configuration are adequately represented by using only variances (i.e. co-variances are not required). Aside from the different weighting of range and azimuth observations (P-I), further separations can be made, e.g., for different image products, which retain the higher accuracy of products with higher resolution and lead to an optimal data combination (P-II). In addition, the combination of observations from different SAR missions becomes possible.

In summary, the described least squares approach including the VCE offers a very flexible tool to process SAR range and azimuth observations. The SAR systems approach ensures the consistency of the observations, and the least squares solution provides a unified method to estimate the geometric calibration constants and to generate accurate ITRF coordinates with SAR positioning. Depending on the envisaged application, the design matrix $\mathbf{A}$ and the linearized equation system (Eq. 2.19) can be modified accordingly.

2.4.1 SAR Geometric Calibration and Geolocation Analysis

The geometric calibration of the range and azimuth bias constants ($\Delta\tau_e, \Delta t_e$) is performed with CRs with known ITRF coordinates. To estimate the values with the least squares method, the design matrix $\mathbf{A}$ is reduced to the two bias parameters

$$
\mathbf{x} = \begin{bmatrix} \Delta\tau_e & \Delta t_e \end{bmatrix}^T. \tag{2.27}
$$

Image series with different geometries and acquisition modes can be combined for an estimation of the best fitting calibration constants. A number of 20 to 30 SAR images is proposed to obtain accurate calibration values, providing that the experimental setup of CRs and image products ensure a sufficient level of SCR for accurate SAR observations (see section 2.1).

For TSX and TDX, the refinement of the geometrical calibration was carried out with high-resolution spotlight images acquired for the permanent reflectors at the geodetic stations of Wettzell, Metsähovi, and GARS O'Higgins. Finally, only the observations of the CR at Metsähovi (more than 200 images) were selected for the calibration update, because this CR is directly attached to stable bedrock and the range and azimuth observations have the smallest variances of all three test sites (P-V). Using only a single site for geometrical calibration also enables the straightforward assessment of the calibration constants with the remaining test sites. With the careful *a priori* correction of all the known error sources in Eq. 2.9, the constants are expected to be largely independent of the test site. This could be confirmed by the experiments, especially when using the enhanced TerraSAR-X orbit product (P-IV; P-V). However, an average geometrical calibration across the three test sites would be readily possible by combining the observations in a joint adjustment. Regarding the Sentinel-1 mission, the current

geometrical calibration is already applied by the IPF processor (see section 2.3.3), but recalibration tests based on the data of the Australian reflector array indicate that updates of up to 20 cm will be required to match the SAR observation modelling (P-III).

Once the geometrical calibration is known, the accuracy of range and azimuth observations can be analyzed in the 2-D slant range image geometry. The procedure is generally identical to the geometrical calibration with known reflectors. When the calibration constants are removed from the parameter model, the design matrix **A** disappears (see Eq. 2.19) and the least squares estimation becomes an adjustment of observations with respect to the SAR observation model (cf. *adjustment of observations only;* Mikhail and Ackermann, 1976). This is equivalent to the analysis presented in P-III. The observation residuals of the adjustment can be further analyzed for long-term trends in the overall SAR system or residual errors introduced by the spectral SAR image processing (P-III,P-V), or they can be used to assess the impact of different orbit solutions (P-IV). Therefore, geometrical SAR calibration, SAR geolocation analysis, and the SAR-based orbit validation (termed SAR ranging in P-IV) all belong to the same processing scheme that assumes the ITRF coordinates to be known. They enable the determination of remaining system biases, the analysis of residual effects, and the assessment of orbit solutions.

2.4.2 SAR Positioning

The SAR positioning assumes a calibrated SAR system and uses the observations from a set of images to estimate the target coordinates. The design matrix **A** now only contains the ITRF coordinates which involve the linear velocity vector. Consequently, the model amounts to six unknown parameters (Eq. 2.19):

$$\mathbf{x} = \begin{bmatrix} x_T & y_T & z_T & \dot{x}_T & \dot{y}_T & \dot{z}_T \end{bmatrix}^T . \tag{2.28}$$

In theory, three images (corresponding to six range and azimuth observations) are sufficient to solve for the six parameters, but a reliable estimation of a velocity of a few centimeters per year as carried out for the ITRF stations requires long measurement series that comprise at least three years of data (Altamimi et al., 2017). Therefore, the more common parameter setup for SAR positioning is using only the three coordinate components, while the velocity may be neglected for short timespans (e.g., 1-2 months), or alternatively modelled based on *a priori* data (see section 2.3.5). In this case, a stereo dataset of two images is required to solve for the three target coordinates. This already defines an overdetermined problem demanding a parameter adjustment, but the advantage of the least squares method lies in the combination of all SAR images from arbitrary viewing geometries that provide range and azimuth observations for the same target. It is now proposed to refer to this method as SAR positioning rather than (geodetic) stereo SAR used earlier in the publications (P-I; P-II; P-VI), because stereo is often only associated with image pairs and radargrammetric methods (e.g., Leberl, 1990).

A fundamental requirement for reliably determining the coordinates is a spatial separation in the geometry of the acquired images. It is generally possible to use only images from repeat pass acquisitions, which vary in the zero-Doppler position because of the envelope allowed to the absolute satellite orbit (e.g., 50-250 m, see section 2.2). A solution with TerraSAR-X using only images from repeat pass acquisitions of one of the CRs at the Geodetic Observatory Wettzell is presented in P-I. The least squares solution can be reliably estimated, but the positioning accuracy and the estimated precision are severely limited by the small baseline. This is confirmed by the variance-covariance matrix showing errors of more than 7 m.

Images from two or three adjacent passes (only ascending or only descending) represent the most often used configuration in SAR positioning, because a conventional CR is only accessible within its boresight direction and the currently operating SAR missions acquire the images with a given view orientation (usually right-looking with respect to satellite heading) (P-III). The same applies to opportunistic PS for which objects that behave like a trihedral reflector are more common than objects with multi-directional backscatter originating from approximately the same phase center (e.g., a singular lamp pole surrounded by a smooth surface; P-I, P-VI). Nevertheless, the ITRF positions of CRs measured with single-sided configurations can be retrieved with an accuracy of 3-5 cm (95 % confidence level) when using the accurate observation modelling, as it was demonstrated with TerraSAR-X (P-I, P-V). For usable opportunistic PS, the estimated accuracy is reduced by factors of 2 to 3 when compared to CRs observed with similar configurations (P-I,P-VI). The main reasons are the amount of signal backscatter (usually lower because purposefully oriented CRs define the best case) and small variations of the phase center with respect to the different viewing geometries (not the case for tightly manufactured CRs) resulting in a less consistent observations for the positioning.

The ideal SAR positioning configuration combines ascending and descending acquisitions. This leads to intersection geometries of nearly 90 ° for the measured ranges and thus to a very isotropic error distribution for the estimated coordinates. Even with the high measurement accuracy of large trihedral CRs, the confined geometry of a single-sided configuration is only partially compensated. Scatters measured with lower range and azimuth accuracy but captured from two sides can still achieve an overall more accurate positioning solution, as pointed out for the experiment reported in P-II. Suitable scatterers can be established by placing special reflectors with multi-directional backscatter for a common phase center, e.g. reflectors composed of eight small CRs in a diamond-shaped arrangement termed octahedron reflectors (P-II). Opportunistic scatterers with similar characteristics are lamps, traffic signs or other isolated structures that involve straight poles. Candidates can be automatically detected by introducing external knowledge (road networks to constrain the search; very high-resolution optical data for direct identification), but first tests indicate that even for X-band and the high-resolution spotlight modes of TerraSAR-X the number of usable multi-directional scatterers remains low (Montazeri et al., 2018). For C-band SAR and medium resolution products, such scatterers can be created by installing active transponders. These devices record, amplify, and return the signals of the SAR, and can be constructed to support both ascending and descending pass directions (Mahapatra et al., 2014). However, further research is required on how to model a common phase center for these devices.

2.4.3 Differential SAR Positioning

Forming the difference between observations is a well-established procedure in the field of GNSS to eliminate system biases and to reduce the impact of atmospheric perturbations, orbit errors and other systematic errors (Teunissen and Montenbruck, 2017). The effectiveness depends on the correlation of observation errors for different locations. For instance, within spatial distances less than 1 km, it is safe to assume identical atmospheric conditions, and if the height difference between two locations is moderate (e.g., 100 m), one can even neglect the atmospheric corrections (Teunissen and Montenbruck, 2017). For these cases, a differential setup is expected to improve the positioning accuracy and the computation of the atmospheric and geodynamic corrections is not required, but the differential computation introduces the need for a reference location to provide a datum. A typical configuration could use a CR co-located with a GNSS receiver and several other CRs distributed in the surroundings. If all CRs are contained in each of the images, the baselines with respect to the reference location can be determined by forming the differences of the simultaneously acquired observations. The principles and the experimental validation of such a setup with TerraSAR-X is presented in P-II.

From a mathematical point of view, the derivation of the method is straightforward when using the linearized scheme as outlined in Eq. 2.19. Applying the difference operator to the observation equations of two targets yields the differential range and azimuth observations as well as the differential baseline vector between both targets. Denoting the reference target with index 0 and any other target with index k, the differential observations read

$$\begin{aligned} \Delta t_a^{0,k} &= t_a^0 - t_a^k + \Delta t_e^{0,k} \\ \Delta \tau_r^{0,k} &= \tau_r^0 - \tau_r^k + \Delta \tau_{tro}^{0,k} + \Delta \tau_{ion}^{0,k} + \Delta \tau_e^{0,k}. \end{aligned} \tag{2.29}$$

There potentially remain differential biases introduced by the atmospheric delays and the artefacts related to the SAR processing (section 2.3.3). However, differential observations of targets with small spatial separation can be assumed free of systematic errors and there remain only the random errors primarily driven by the SCR). Hence, for sufficiently large CRs and high-resolution SAR image data, the random errors of differential observations should be on the order of a few millimeters in range, and better than 1 cm in azimuth. The latter is presently limited by the quantization in the absolute time annotation within the SAR payload (see section 2.3.3).

The parameter vector $\mathbf{x}$ of the differential configuration contains the baseline between target 0 and target k

$$\mathbf{x} = \begin{bmatrix} \Delta x_T^{0,k} & \Delta y_T^{0,k} & \Delta z_T^{0,k} \end{bmatrix}^T. \tag{2.30}$$

Any other component of the position model (Eq. 2.13) cancels, because for otherwise stable targets the global ITRF velocity is identical and the periodic geodynamic deformations usually have high spatial correlations of several tens of kilometers (Petit and Luzum, 2010). If the stability of a target k is not confirmed, an additional relative velocity vector could be estimated. However, it is assumed here that only the difference vector $\Delta \mathbf{X}_T^{0,k}$ needs to be solved for by the least squares estimation:

$$\mathbf{X}_T^k = \mathbf{X}_T^0 + \Delta \mathbf{X}_T^{0,k}. \tag{2.31}$$

Applying the difference operator for the linear system of equations (Eq. 2.18) results in a linear combination of lines, which does not alter the overall properties of the linear equation system. Consequently, the solution process as outlined for the standard positioning remains the same for the differential case: the $\mathbf{B}$-matrix can still be inverted, the solution again becomes an ordinary least squares adjustment, and the residuals of the differential observations can be used for the VCE.

A first practical experiment for differential SAR positioning was performed with TerraSAR-X and four reflectors at the Wettzell geodetic observatory (P-II). Although the data composed of four staring spotlight scenes and eight high-resolution spotlight scenes was not ideal (there were conflicts with other TerraSAR-X orders at that time), the results still can confirm most of the theoretical considerations. In particular for the staring spotlight measurements, the VCE results show an improvement by approximately a factor of two for the differential range and azimuth observation errors when compared to the undifferenced observations, but because of the small reflector size (0.23 m) the average errors of the differential range and azimuth observations are 0.7 cm and 1.8 cm, respectively. For the noisier high-resolution spotlight data, the results are less decisive as only one of the differential setups decreases in observation error, but with the VCE accounting for the different imaging modes all the observations are optimally combined. The reduction of biases in differential SAR configurations is confirmed by the removal of the 5 cm height offset found in the comparison of the standard SAR positioning results and the local ties. The results of the differential positioning are therefore more accurate and differ only by 2-3 cm from the ground truth coordinates. The experiment was successfully carried

out for a small number of twelve images. However, the image number and the short baselines of less than 100 m between the targets limit the more general interpretation of the method for SAR. The Australian CR array provides the possibility for a wide-area verification with larger reflectors. This could be used in future to further investigate the differential positioning capabilities of SAR.

3 Discussion and Analysis

SAR imaging geodesy as presented in the previous chapter shares many elements of the well-established space geodetic techniques GNSS and SLR. The following sections discuss advantages and disadvantages for the applications SAR positioning (P-I; P-V) and SAR ranging (P-IV) with respect to these existing techniques.

3.1 SAR Positioning versus GNSS

The early developments of GNSS began in the 1980s and the technique reached full operational capability in 1995 with the first global systems GPS (USA) and GLONASS (Russia). Since then, the satellite-based positioning technique has been further improved and extended into a permanent and all-weather capable service supporting a multitude of applications, e.g., terrestrial survey and mapping, marine, air and land navigation, orbit determination, or atmospheric science (Teunissen and Montenbruck, 2017). With the addition of Galileo (Europe) and BeiDou (China), there are now four actively maintained systems that provide global coverage and additional regional systems and geostationary augmentation systems. All these systems transmit microwave signals between 1.1-1.6 GHz for space-based radio navigation (Teunissen and Montenbruck, 2017). Summarized under the name of GNSS, the signals can be used in many different configurations to serve a wide range of applications with positioning, timing, and navigation. Notable features of GNSS application configurations are the type of observations (pseudoranges versus phase), the processing (real-time versus post-processing) and the positioning setup (absolute versus differential; static versus kinematic). The possibility to arbitrarily combine these elements provides GNSS with the flexibility to achieve optimal results in the different applications.

In the case of GNSS and scientific geodesy, the aim is for very high accuracy in positioning. This requires phase-based observations, elaborate post-processing, stable configurations for long-term monitoring, and either single receiver solutions or the joint inversion of entire receiver networks. At the core of global geodetic GNSS activities lies the GNSS-based realization of the ITRF, which is carried out under the guidance of the IGS and this realization also contributes to the final multi-technique reference frame solution (Villiger and Dach, 2018; Altamimi et al., 2016). The latest GNSS-based frame is named IGS14 and was adopted on 29 January 2017 as the new datum for the precise GNSS products, most notably the satellite orbits and the modelling of the satellite clocks (Villiger and Dach, 2018). These products enable positioning solutions for a single receiver with centimeter or even millimeter accuracy when applying precise point positioning (PPP) (Kouba et al., 2017). The method assumes the GNSS orbits and the satellite clocks as fixed and uses the undifferenced dual-frequency observations for the estimation of the receiver position (Zumberge et al., 1997; Kouba et al., 2017). The PPP is therefore very similar to the concepts used in the absolute SAR positioning of a single CR, which makes the PPP a useful benchmark for a general discussion of the SAR method.

Regarding the *a priori* data reduction, the only major differences are the effects stemming from the individual techniques. SAR may require corrections for the residual focussing effects, the on-board timing (oscillator frequency, time synchronization), and the delay calibration. For PPP, the impacts

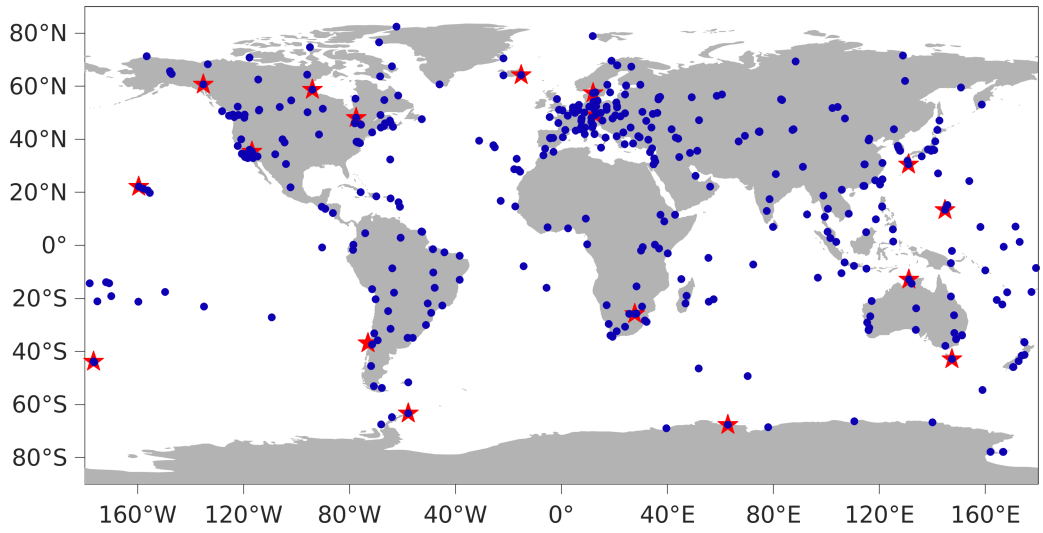

Fig. 3.1: GNSS stations contributing to the global IGS network (January 2019). The stations marked in red were used in the PPP analysis discussed in text.

of the antenna phase center variations (satellite and receiver), the phase wind-up, and the differential code biases have to be considered (cf. Table 25.1; Kouba et al., 2017). All other elements, i.e. the satellite center of mass, the antenna offset vector, the atmospheric path delays, and the dynamic Earth signals are generally identical for both techniques. GNSS operates with multiple frequencies in the L-band for which the ionospheric delays can be eliminated by forming linear combinations and taking into account the higher order error terms of the ionospheric delay (Kouba et al., 2017). While the hydrostatic tropospheric delay is modelled with the VMF product (see section 2.3.4), the PPP additionally estimates the wet tropospheric delay and horizontal tropospheric gradients. The continuous tracking of the GNSS satellites enables the decorrelation of the atmospheric delay with respect to the other GNSS estimation parameters (receiver clock, ambiguities, receiver position), which results in accurate receiver-based tropospheric delay products distributed, e.g., by the IGS (Byram et al., 2011; Villiger and Dach, 2018). Multiple GNSS systems can be combined in the PPP, providing that the *a priori* products (orbits, satellite clocks) have a consistent datum and intersystem biases are known.

The accuracy achieved with PPP can be demonstrated by processing data from the IGS stations[1] contributing to the ITRF solution (Fig. 3.1). The position of these receivers is determined in the ITRF for any given epoch because the reference coordinates were estimated as part of the global frame solution. Consequently, PPP solutions computed in daily static configurations can be validated against the given reference coordinates. In Kouba et al. (2017), such a validation was performed at 17 globally distributed IGS stations using one year of GNSS observations for the period January 2012 to February 2013 (Fig. 3.1). The PPP solutions were computed on a daily basis and compared to the reference positions to obtain residuals in north, east, and height direction. Ambiguity fixing was not applied in the analysis, because for undifferenced GNSS observations this is not a straightforward process (Kouba et al., 2017). However, the authors consider the impact on the result statistics to be small because of the daily static processing configuration. The float ambiguities are only noticed in the the slightly larger error of the east component. With the final IGS orbit and clock products, the RMSs of the GPS-only solution across the 17 stations read 2.8 mm, 3.9 mm, and 7.5 mm in north, east, and height, respectively (Table 25.4; Kouba et al., 2017). In comparison, a joint GPS and GLONASS solution using the orbit and clock products of ESA yields RMS results of 3.6 mm, 3.7 mm, and 7.6 mm.

[1]For the current status of the IGS network see: http://www.igs.org/network

Because of common residual systematic effects in both GNSS systems, the additional GLONASS observations do not improve the positioning. Nevertheless, the close agreement between the GPS-only results and the combined results confirms the applicability of the PPP method. Furthermore, both results show the ratio of horizontal versus height precision common to GNSS which is caused by the positioning geometry (i.e. dilution of precision (DOP), Hofmann-Wellenhof et al., 2008; Teunissen and Montenbruck, 2017). In summary, the positioning accuracy of PPP applying ITRF standards is noted to be on the order of 3-4 mm horizontally and 7-8 mm vertically.

For SAR imaging geodesy, the most accurate positioning solutions were achieved with TerraSAR-X for the five CRs at the geodetic stations when using the experimental TerraSAR-X orbit solutions (P-V [Table 10]). Computing the RMSs of the remaining offsets to the known ITRF coordinates, as it was done for the PPP study, yields 8.9 mm, 15.3 mm, and 8.4 mm in north, east, and height, respectively. Due to the small number of samples of only five CRs, the estimated positioning accuracy scaled to 95 % confidence is considered a more reliable criterion than the RMS to judge the results. The average values across the CRs read 7.9 mm, 19.1 mm, and 16.1 mm (north, east, height; P-V [Table 10]). In comparison to GNSS PPP, the results indicate quality differences of a factor 2-3 for the positioning accuracy. However, it is important to note that the SAR results of these CRs only involve geometric configurations of two or three adjacent passes with equal heading, which has a considerable impact on the positioning error. The four multi-directional reflectors positioned with observations from ascending and descending passes achieve an average estimated positioning error of 29.2 mm, 25.3 mm, and 28.6 mm in north, east, and height (95 % confidence level; P-II [Table 5]). The absolute level of the positioning error is larger, because the small size of the reflectors degrades the observation precision, but the distribution of the error across the coordinate components has become much more homogeneous. Therefore, a combination of accurate observations and multiple ascending and descending pass geometries should be able to attain a positioning accuracy that approaches the level of GNSS PPP.

In order to provide a more detailed analysis of the impact of the geometry in SAR positioning, global simulations were computed for two configurations of TerraSAR-X and Sentinel-1. The first configuration assumes a single CR oriented for ascending passes, whereas the second configuration simulates the combination of ascending and descending passes. The latter could be achieved by installing two CRs next to each other and calibrating the local tie between their phase centers. Assuming one spacecraft for each mission and using the precise orbit solution of one repeat cycle (11 days and 12 days), the available passes are analyzed for each location on the Earth's surface. Both missions have nominal right-looking views and the accessible ground swaths are defined according to the sensor specifications (see Table 2.1): 20-56 ° for TerraSAR-X (access range of the high-resolution spotlight mode) and 25-41 ° for Sentinel-1 (fixed swath of the IW mode; Bourbigot et al., 2015). The computations are performed for a global grid spanning -80 ° to 86 ° latitude with an equal spacing of 0.5 ° for both longitude and latitude. The coverage in latitude is reduced because for the access range allowed by the sun-synchronous orbits there remain blind areas at the poles. The poles can still be sensed by exceeding the full performance access range and additionally rotating the satellite to left-looking to cover the South Pole region, but this was not considered for this nominal operation analysis. The usage of a single orbit repeat cycle ensures that all possible pass geometries at a location are considered in the prediction of the positioning solution.

After resolving the zero Doppler geometry for each pass fulfilling the geometric constraints, the stochastic positioning error (variance-covariance matrix) is estimated by evaluating the system of normal equations:

$$\Sigma(\hat{\mathbf{x}}) = \left(\bar{\mathbf{A}}^T \cdot \mathbf{P} \cdot \bar{\mathbf{A}}\right)^{-1}. \tag{3.1}$$

The matrix $\bar{\mathbf{A}}$ is rigorously defined by the sensor-to-ground geometry at zero Doppler (see section 2.4). The weight matrix $\mathbf{P}$ requires assumptions for the standard deviations of the range and azimuth observations. In the case of TerraSAR-X, common values as determined for the high-resolution spotlight data are assumed, i.e. ± 1.5 cm for the range and ± 2.5 cm for the azimuth measurements (P-V). For Sentinel-1, the assumed standard deviations read ± 5 cm and ± 25 cm (P-III). These values define plausible random error budgets for SAR observations of trihedral CRs with an edge-size of 1.5 m. Therefore, they allow a direct comparison of the results for both missions and the assumed products. To enable a straightforward global interpretation, the results as obtained with Eq. 3.1 were rotated to local north, east, and height (e.g., Hofmann-Wellenhof et al., 2008), which provides s_N, s_E, and s_H at each location.

The number of potentially available TerraSAR-X acquisitions for the ascending configuration is shown in Fig. 3.2a. At the equator the access range of 20-45 ° of the SAR instrument allows positioning solutions with at least two adjacent observation geometries for every point. When moving away from the equator the tracks start to converge and gradually give access to a third adjacent pass geometry, but only at 45 ° latitude this becomes possible at every location. The numbers further increase with latitude and reach 7-8 usable passes at 75 ° latitude. Beyond this latitude, there is a sharp increase as the ground tracks start to intersect. Close to the North Pole almost every ascending pass can be used because of the right-looking sensor orientation, whereas towards the South Pole the blind area becomes visible at 79 ° southern latitude. At low latitudes, the solution for the north coordinate is mainly driven by the along-track azimuth observation. Therefore, the resulting positioning error is approximately the given azimuth standard deviation divided by the square root of the number of azimuth observations, and the error becomes smaller with latitude as the number of passes increases (Fig. 3.2c). The range observations chiefly resolve the east and height coordinates. The east coordinate is generally less accurately estimated because there are no range observations below 56 ° incidence angle. However, depending whether two steeper or shallower incidence angles are being combined the situation can become reversed. Moreover, the converging tracks gradually reduce the spatial separation of the pass geometries and the quality starts to degrade with latitude until the next adjacent geometry becomes accessible. This creates the intricate sub-patterns visible in Fig. 3.2e and Fig. 3.2g. Overall, the predicted errors for the ascending only configuration with 2-5 SAR acquisitions are on the order of 1-2 cm for the north coordinate, and 3-5 cm for east and height coordinates. The configuration is most sensitive to the north coordinate, which confirms the experimental results obtained with TerraSAR-X.

The combination of ascending and descending pass geometries effectively doubles the number of accessible geometries for each location (Fig. 3.2b). Consequently, the error estimated for the north coordinate follows the aforementioned law of averaging and is further reduced by the square-root of the number of the additional passes (Fig. 3.2d). The impact of the additional geometries on east and height coordinates is even more pronounced and the simulation predicts a four times more reliable estimate for these coordinates (Fig. 3.2f and Fig. 3.2h). This is comparable to the scaling of the DOP in GNSS which is driven by the constellation of the measured GNSS satellites and contributes to the overall error of GNSS positioning (Hofmann-Wellenhof et al., 2008; Teunissen and Montenbruck, 2017). For the given SAR simulation, the positions are therefore estimated with errors of 1.2 cm or better across all coordinates, of which the height coordinate has the smallest error budget.

For the TerraSAR-X configurations, the analysis illustrates the general possibilities of global SAR positioning with accurate observations. In practice, the mission is confined to selected test sites, because the operational time of the SAR payload was designed to support approximately 5 minutes of acquisitions during one 90 minutes orbit cycle. With this constraint it would take at least some

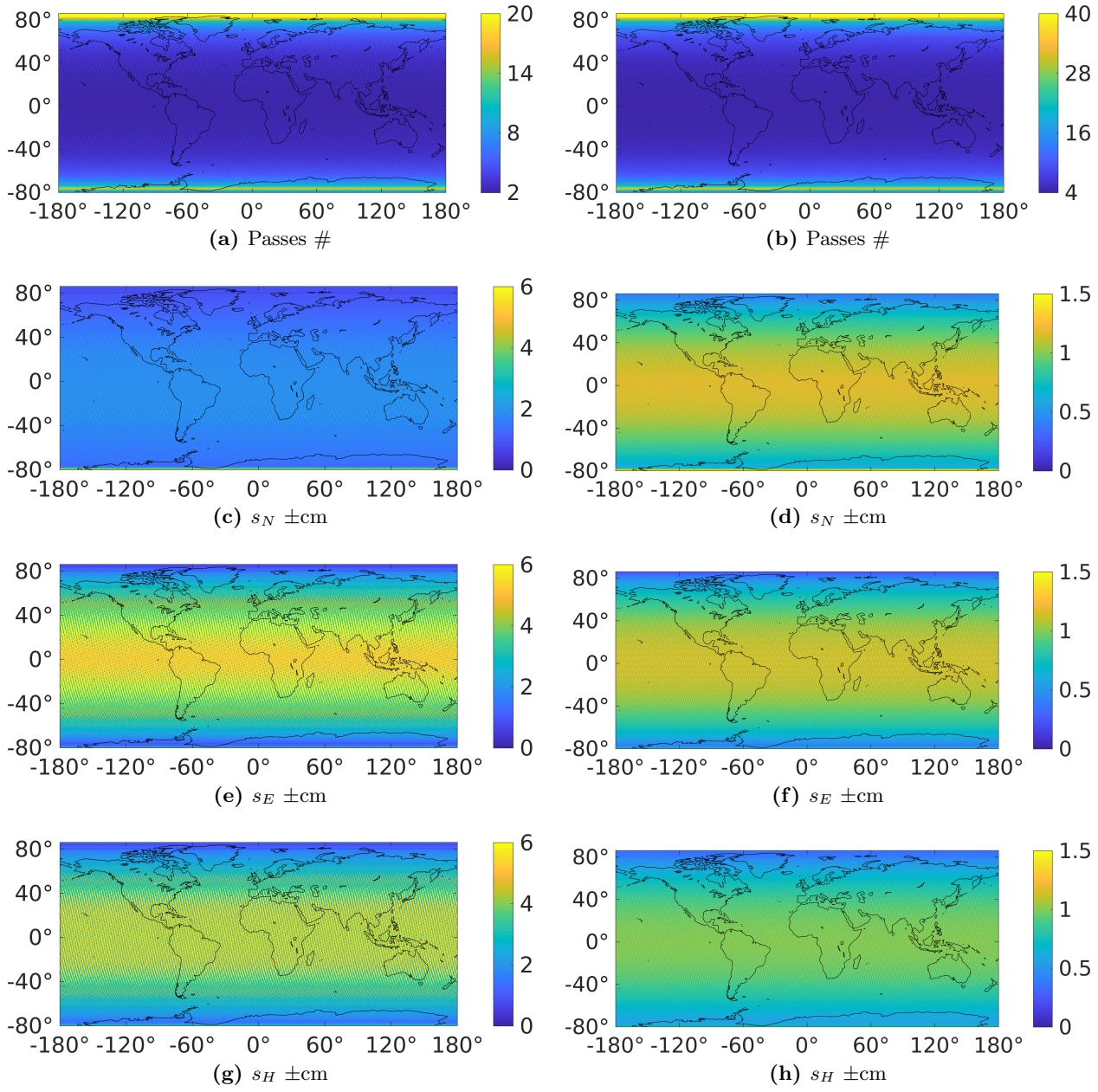

(a) Passes # **(b)** Passes # **(c)** s_N ±cm **(d)** s_N ±cm **(e)** s_E ±cm **(f)** s_E ±cm **(g)** s_H ±cm **(h)** s_H ±cm

Fig. 3.2: Simulation of TerraSAR-X positioning errors (1σ) for the accessible observations of a single 11 days orbit repeat cycle. Assumed observation standard deviations: 1.5 cm (range) and 2.5 cm (azimuth). Results for ascending passes only (left) and the combination of ascending and descending passes (right). Note different colour scales.

330 cycles (or about 10 years)[1] to cover all the Earth's land surface with the high-resolution spotlight mode and achieve the coverage shown in Fig. 3.2b. Such a timeframe is of course not useful in practice. However, by trading resolution for ground coverage, increasing the payload duty cycle, and adding further spacecraft the regular global acquisition has become attainable with SAR.

[1] This coarse estimate was derived as follows: 90/5/3 yields the cycles to achieve operation over one third of a revolution assumed for land; 550/10 cycles are needed to cover the accessible 550 km ground range at each location with the 10 km supported by the high-resolution spotlight mode; the outcome is about 330 orbit cycles or nearly 10 years

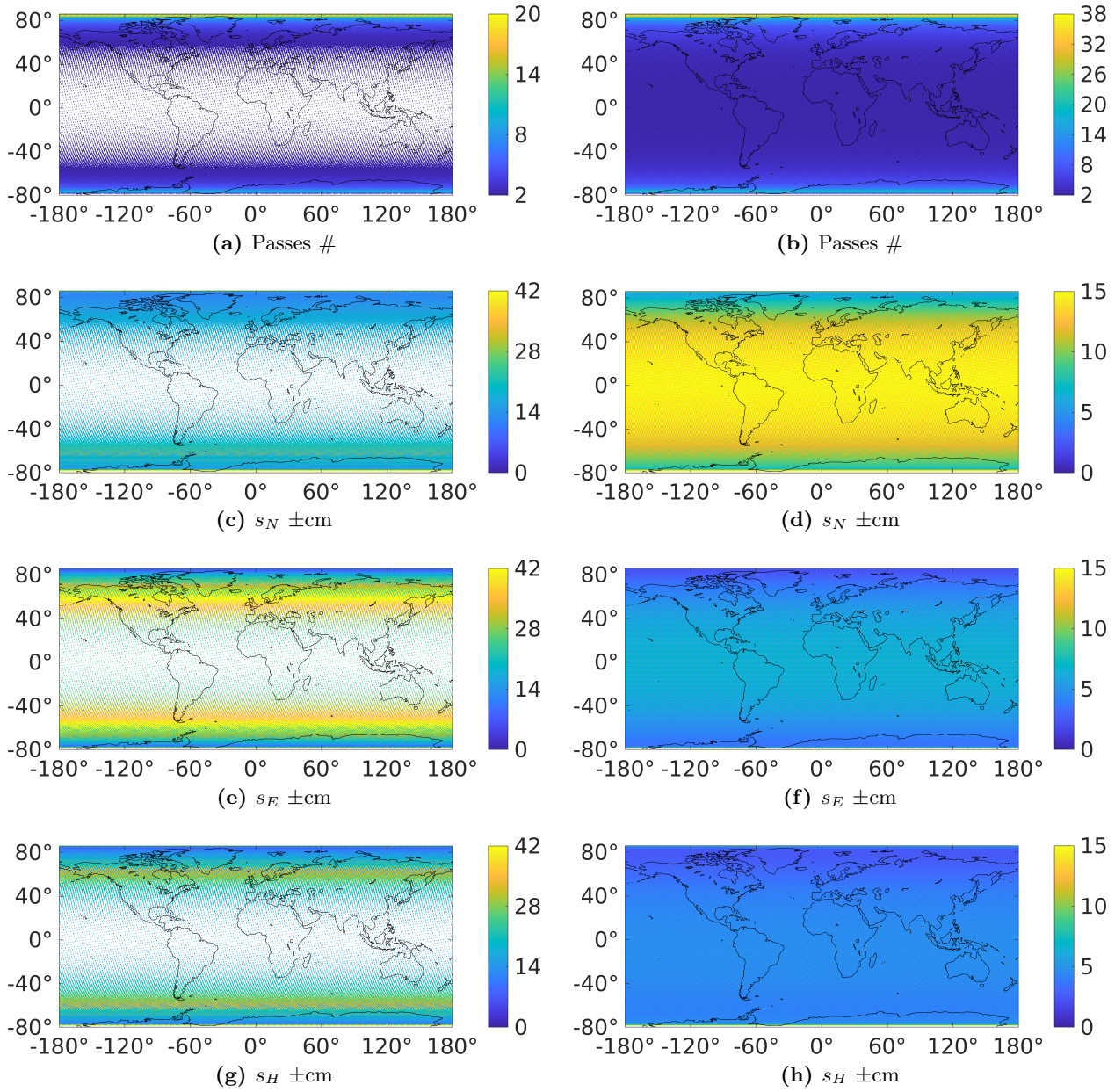

(a) Passes # **(b)** Passes # **(c)** s_N ±cm **(d)** s_N ±cm **(e)** s_E ±cm **(f)** s_E ±cm **(g)** s_H ±cm **(h)** s_H ±cm

Fig. 3.3: Simulation of Sentinel-1 positioning errors (1σ) for the accessible IW observations of a single 12 days orbit repeat cycle. Assumed observation standard deviations: 5 cm (range) and 25 cm (azimuth). Results for ascending passes only (left) and the combination of ascending and descending passes (right). Note different colour scales.

Such a global coverage is realized by Sentinel-1, which supports continuous instrument operation of 25 minutes per orbit for the standard IW mode (Torres et al., 2012). Therefore, the access range modelled for the Sentinel-1 simulation was defined according to the 250 km swath width of IW, which is designed to cover the entire equator during one orbit cycle. This also means minimum swath overlap at the equator and therefore a Sentinel-1 ascending only configuration cannot achieve positioning solutions for every location between ±60 ° latitude (cf. blank regions, Fig. 3.3a). The error distribution across north, east and height coordinates is similar to TerraSAR-X, but the numbers are significantly larger due to the standard deviations assumed for the range and azimuth observations (Fig. 3.3c; Fig. 3.3e;

Fig. 3.3g). Because of the steeper range geometry, the height coordinate can be measured more reliably, whereas the north coordinate is obviously limited by azimuth observation due to the 22 m azimuth resolution of the IW product. Once more, the combination of both pass directions doubles the number of acquisitions per location, but in the case of Sentinel-1 this additionally enables the seamless global positioning (Fig. 3.3b). With estimated errors of up to 15 cm, the north coordinate (Fig. 3.3d) still differs by a factor of ten from the predicted results of TerraSAR-X. The east and height coordinates are more reliably determined. With error estimates of 3-5 cm for the height coordinate, the difference to TerraSAR-X is not as large as for the horizontal coordinates.

It is important to note that in Europe the Sentinel-1 mission indeed provides the single cycle coverage as shown in Fig. 3.3b (CSC Mission Management Team, 2018). With the addition of the second spacecraft Sentinel-1B in 2016, the European pattern is now regularly covered and the global Sentinel-1 observation scenario also enables one ascending and one descending geometry for other regions of interest (e.g., regions with active tectonics or agricultural production areas). Therefore, several hundreds of SAR observations per location will be acquired for many areas during the Sentinel-1 mission lifetime, which will lead to high redundancy in the position estimation and thus a significant reduction of the stochastic positioning errors by the least squares approach.

Repeating the measurements with each orbit cycle reduces the random observation errors by the number of used cycles. For instance, a number of 30 Sentinel-1 orbit cycles (1 year) for the combined ascending and descending configuration predicts a stochastic positioning error close to the 1 cm level for the east and height coordinates and 2 cm for the north coordinate. The same applies to TerraSAR-X, for which a small number of about 3-4 cycles at a selected test site would be sufficient to achieve similar results, because the mission can take advantage of the high-resolution imaging modes that enable SAR measurements with 1-2 cm standard deviation, as assumed in the simulation. However, the synthetic simulations shown in Fig. 3.2 and Fig. 3.3 do not account for the spatial error variation of the SAR observations which is driven by the quality of the atmospheric path delay corrections, and small residual biases (atmosphere, orbit, system electronics) will remain which cannot be mitigated by redundant observations. These biases will set a limit to the attainable positioning quality, but approaching centimeter or even millimeter level coordinates seems feasible with repeated observations for regions that either support accurate atmospheric corrections because of complementary GNSS observations or benefit from a generally less perturbed atmosphere that favours atmospheric models, e.g., dry deserts. Furthermore, the combination of independent SAR missions is readily possible, because passive reflectors of adequate dimension enable consistent observations for sensors with different radar frequencies and different SAR modes. For instance, a combination of TerraSAR-X and Sentinel-1 would increase both the number of acquisitions and the diversity of the acquisition geometries, which should further reduce the positioning error.

In conclusion, the SAR positioning will not be able to provide the flexibility of PPP with GNSS. However, for specific scenarios involving long-term position monitoring accurate results could be achieved with SAR in future. Mixed networks with GNSS receivers and SAR reflectors are also conceivable. While GNSS offers instantaneous position solutions for each observation epoch as well as highly accurate PPP solutions for daily estimates, the receivers require constant power supply and data forwarding for processing. These limits do not apply to SAR when using passive reflectors, but not all CR designs are suitable for unattended operation. Rain may flood reflectors without sufficiently dimensioned drainage holes or snow can accumulate in CRs installed at locations experiencing winter season (Garthwaite, 2017). Adaptations in the design (e.g., mesh surfaces) or the usage of radar transparent covers against rain and snow, see for instance Lauknes (2010), could enable permanent SAR monitoring markers at remote locations like the Antarctic mainland or volcanic islands. The CR dimension is of course an important element in all these considerations and should be selected large

enough to avoid limitations in the envisaged SAR observations. For reference markers at geodetic stations or elaborate long-term monitoring networks like Australian CR array, large 1.5 m reflectors can be justified in order to support reliable measurements even with the Sentinel-1 IW products. Other application may demand for smaller reflectors that are easier to handle and offer more flexibility with the installation. A size reduction without degrading the observations quality is possible for the high-resolution SAR imaging mode of TerraSAR-X, as demonstrated in P-II, whereas for Sentinel-1 active transponders could offer a practicable solution (Mahapatra et al., 2014). They require power supply, but these shoe box sized devices can offer an RCS of up to meter-sized CRs in C-band SAR. Further investigations regarding the long-term stability and the calibration of the internal delays are planned to assess their feasibility for positioning with Sentinel-1.

Aside from the artificially created markers, SAR positioning can be also performed for large numbers of opportunistic scatterers when using high-resolution X-band data of urban areas (Montazeri et al., 2018). Even with a generally reduced positioning accuracy of 10-15 cm these points represent valuable ground control points that can be used to geocode optical images by identifying common features in both image types, e.g. lamp poles (Montazeri et al., 2018). A measurement of these features with GNSS can provide more reliable coordinates, but this would involve considerable effort and time to collect the observations. The most precise of these opportunistic scatterers as determined with SAR positioning are of particular interest for the phase-based SAR techniques PSI and TomoSAR because they enable accurate geocoding and the fusion of results without the need for on-site terrestrial measurements (P-VI).

Passive ground infrastructure for accurate observations and the exploitation of opportunistic signals are the main advantages of SAR positioning. The data collection is slower than with GNSS and bound to the configuration of the SAR mission (orbit type, SAR mode, number of spacecraft), but over time consistent observations with centimeter or even millimeter precision can be acquired. The need for *a priori* atmospheric path delay is another small disadvantage compared to GNSS, which can eliminate or estimate these path delays from the observations. However, with future advancements in atmospheric modelling this aspect can be expected to become less critical. Like the PPP of GNSS, the SAR positioning can be carried out on a global scale. It offers the interesting property of providing highest positioning accuracy in the near polar regions because of the commonly used sun-synchronous orbits. All these features could make SAR positioning a useful addition to the existing geodetic methods.

3.2 SAR Ranging versus SLR

The range measurements of SLR and SAR are based on similar principles. It is therefore interesting to compare both types of range measurements, also because of the capabilities of current SAR missions to provide more precise range observations than azimuth observations. Missions that support global or regional monitoring (e.g., Sentinel-1) tend to use SAR modes that trade azimuth resolution for larger swaths on ground, which result in less precise azimuth observations (cf. the Sentinel-1 IW product; P-III), and even for TerraSAR-X the range observations were found to be more accurate (P-V). Such range observations of permanently installed CRs move SAR towards the methods applied by SLR, especially if the ranges are used to analyse the orbit of a SAR mission, as it was demonstrated in P-IV.

The use of laser pules to measure the distance to orbiting satellites was pioneered by NASA in the 1960s and soon became an important space geodetic technique. Among the first tracked satellites was the Geodetic Earth Observation Satellite 1 (GEOS-1) launched in 1965, which helped to develop

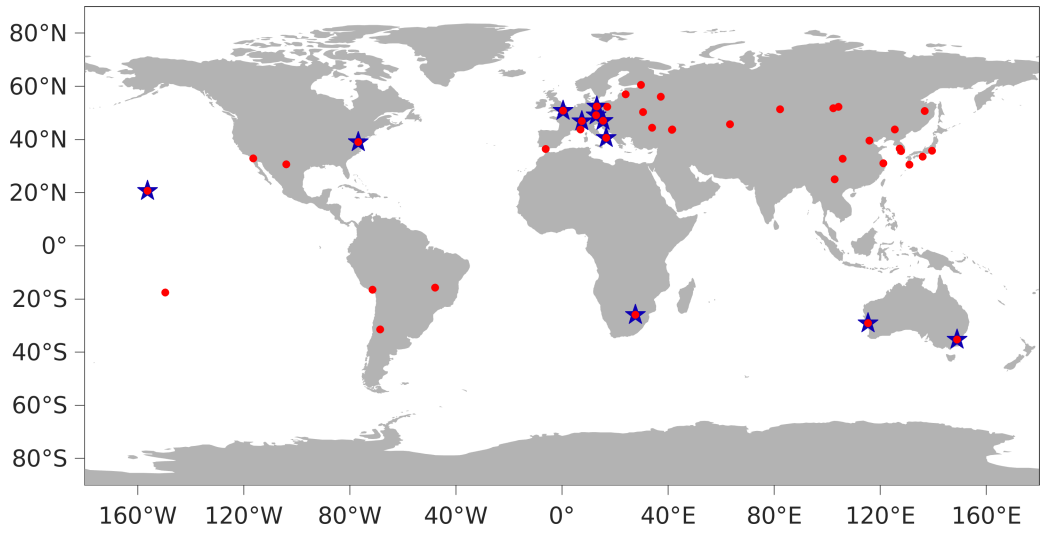

Fig. 3.4: SLR stations contributing to the global ILRS network (January 2019). The stations marked in blue were considered as high-quality stations in the SLR studies discussed in text.

the method and to derive a more precise Earth gravity field model (Combrinck, 2010). In 1976, the passive SLR probe LAser GEOdynamics Satellite (LAGEOS) was placed into an orbit with 6000 km altitude (Smith and J., 1980). It is still in orbit and regularly observed by SLR stations to monitor geodynamic processes and the long wavelength gravity field components. Over the years, the satellites supporting SLR observations and the number of SLR stations steadily increased. Today, a global network of 45 active stations (Fig. 3.4) under the umbrella of the International Laser Ranging Service (ILRS)[1] extensively contributes to global gravity field determination, the realization of the ITRF solutions, and the precise orbit determination and orbit validation of a large number of satellites with laser retro-reflector payloads (Noll and Pearlman, 2012; Arnold et al., 2018; Wilkinson et al., 2018). The satellites are tracked according to an ILRS priority list and involve the passive SLR satellites like LAGEOS, Earth observation satellites (e.g., Cryosat-2, Sentinel-3a, TerraSAR-X), and GNSS satellites. In addition to these standard operations, SLR also supports other activities like lunar laser ranging as well as the emerging techniques of space debris tracking, highly accurate time transfer at the pico seconds level, and deep space laser ranging to selected spacecraft in the solar system (Wilkinson et al., 2018).

SLR is carried out in the optical regime using monochromatic lasers with wavelengths of 535-1064 nm. A laser pulse is directed through a telescope towards a satellite equipped with a retro-reflector and backscattered photons are registered at an aligned receive telescope coupled with a detector and an event timer. In modern SLR systems the transmit and receive paths may share the same telescope optics (Wilkinson et al., 2018). Typical pulse lengths are between 10-100 ps. The duration varies with the pulse repetition rate which is on the order of a few kHz for the latest generation of SLR stations (Wilkinson et al., 2018). The time of transmit and the receive event yield the two-way round trip time and ultimately the distance to the satellite (Combrinck, 2010; Wilkinson et al., 2018). As in the case of SAR, the transmit and receive events are managed by a timing system that consists of a very precise short-term stable interval counter and an additional source providing an absolute time standard (Combrinck, 2010). The latter is the UTC realized by the station's GNSS receiver that is also used to maintain the long-term stability of the timing system, comparable to the calibration data takes carried out with TerraSAR-X (cf. oscillator drift in section 2.3.3).

[1]For the current status of the ILRS network see: https://ilrs.cddis.eosdis.nasa.gov/network/

The range model of SLR comprises of the atmospheric delay, the CoM correction, the relativistic effect of the Shapiro delay, contributions from retro-reflector payload, and the range and time biases (Combrinck, 2010; Arnold et al., 2018):

- The atmospheric path delays are modelled based on the temperature, pressure, and relative humidity recorded at the station. This is sufficient to obtain the zenith delay with an accuracy of better than 1 mm because compared to microwave signals the water vapour has only a small impact for the visible wavelengths used by SLR (Mendes and Pavlis, 2004). However, the atmosphere is dispersive for visible wavelengths and it is therefore important to adapt the correction for a given laser wavelength. The mapping to slant range uses an isotropic mapping function, which can lead to errors of 5 cm at low elevation in the presence of atmospheric gradients, but in general the accuracy of the mapped delay is on the order of a few millimeters (Combrinck, 2010).
- The correction of the CoM is identical to other on-board payloads (e.g., GNSS or SAR) and requires the attitude and the offset between CoM and the retro-reflector. Models defined for the different retro-reflector payloads account for delays of the prism glass and prism offsets from the computational reference point according to the orientation of the payload (Arnold et al., 2018).
- The range bias is station dependent and comprises the residual effects of the atmospheric model, the modelling of the station coordinates, the eccentricity of the telescope with respect to the geometrically defined reference point, and the system delays. The time bias denotes the offset to the absolute time standard affecting the time tags of the observations. Both biases are monitored with stable terrestrial calibration targets (Kodet et al., 2018), but they can be further refined by using the measured SLR residuals and applying least squares parameter estimation (Combrinck, 2010; Arnold et al., 2018).

A comparison of this SLR range model with the model of the SAR range measurements (section 2.3) reveals many similarities. However, a discussion of the differences and observation accuracies is useful to assess the potential of SAR ranges and azimuth observations for geodetic applications.

The SLR station can track every satellite within its field of view and may provide range measurements for the entire pass from horizon to horizon. The ability to carry out observations depends on the weather, as clouds obstruct the laser pulses, and daytime SLR operation is not readily possible. This is because of the greater difficulty to identify a satellite in the telescope and the increase in background noise during daylight observations, which require adaptations in the software and advanced narrow band filters tailored to the laser wavelength (Wilkinson et al., 2018). In recent years a high degree of automation could be achieved for many SLR stations, but at least one operator is still required at most stations to schedule the targets, ensure the on-sky laser safety requirements, refine the tracking, and inspect and forward the measured data. So far only the SLR station at Mount Stromlo, Australia, has managed a fully autonomous operation (Wilkinson et al., 2018). Finally, establishing the co-location of a SLR station with other space geodetic equipment is complicated because the reference point, i.e. the intersection of the two mount axes defining the rotation invariant point of the telescope, is not directly measurable by terrestrial survey (Combrinck, 2010; Poyard, 2017). Establishing the local ties with better than 5 mm is crucial when combining the space geodetic techniques for terrestrial reference determination (Altamimi et al., 2016; Poyard, 2017).

SAR enables observations under all weather and daytime conditions, but for a single CR there is only one range and azimuth observation per pass. The measurable pass geometries are limited by the access range of the instrument (see simulations in section 3.1). An arbitrary number of CRs can be placed in the swath which increases the number of nearly simultaneous measurements. Appropriate CR installations could provide a regular stream of observations along the orbit trajectory. Acquisition

patterns and data forwarding can be automated and coordinated by a single ground segment, and the same holds true for the image generation and the PTA to extract the SAR range and azimuth observations. The survey of local ties for co-located CRs requires less effort as the point of reference (i.e. the intersection of the trihedral surfaces) can be accessed directly. This greatly simplifies the co-location with a GNSS receiver or the integration into a geodetic reference station.

The assessment of the single-shot accuracy of SLR is challenging because there are no redundant range observations that can be compared with the measured SLR ranges. Theoretical estimates based on the station parameters (pulse width, detector jitter, event timer precision) indicate a one-way precision of 20-25 mm RMS for the 10 Hz systems still in use at many of the SLR stations, and 5-10 mm for the more advanced stations that support kHz tracking (Wilkinson et al., 2018). Although full-rate data is available for many stations, the most used SLR observation type is the so-called normal point, which already involves a temporal averaging of single measurements to achieve a precision of 1 mm (Noll and Pearlman, 2012). The averaging varies according to the orbit height of the tracked satellite and the number of usable returns registered by the SLR system. For a low Earth orbiting satellite like TerraSAR-X, a bin size of 5 s is proposed[1].

Apart from the theoretical error modelling, the accuracy can be also evaluated by comparing the normal point observations applying the range model of SLR with a precise orbit solution. For the altimetry satellite Jason-2, which provides one of the most accurate orbit solutions because of the GPS and DORIS payloads that are used for the POD, such a comparison for the normal point data of 2016 yields SLR residuals with a standard deviation of 25.3 mm (Arnold et al., 2018). A reduction of the residuals for a subset of 12 high quality stations, i.e. the stations that are known to have better control of the systemic biases (Fig. 3.4), improves the standard deviation to 12.5 mm (Arnold et al., 2018). On the one hand, these empirical results agree with the theoretical considerations on the different quality level among the SLR systems. On the other hand, it is difficult to form a definite conclusion whether the results achieved with the best quality stations are indeed the accuracy of SLR as a measurement system or if the 12 mm mark an accuracy limit of the underlying reference frames and the Jason-2 orbit solution.

The TerraSAR-X mission offers the unique possibility to compare SLR residuals and SAR range residuals (P-IV). The SLR analysis spanning six years was performed with the same selection of high quality stations that is proposed in Arnold et al. (2018), see Fig. 3.4. The SLR results of 11.4 mm and 12.5 mm standard deviation for TSX and TDX when using the latest experimental orbit solutions are perfectly in line with the results cited for Jason-2. The SAR ranging results of TSX and TDX as computed for the five reference CRs yield standard deviations of 12.5 mm and 14.9 mm, respectively. These findings indicate a remarkably close agreement for the accuracy of both techniques within the framework of the ITRF. There is of course a large difference in the number of observations, i.e. almost 400,000 SLR normal points versus 950 SAR ranges for both spacecraft combined. SLR is also more sensitive to the 3-D errors of the orbit because of the greater variety of observed pass geometries. Nevertheless, such a SAR ranging accuracy opens up new possibilities for SAR satellites without SLR retro-reflectors. Unlike the radar altimeter missions, for which the requirement of POD and orbit validation is one of the drivers when designing the satellite, the SAR satellites have so far rarely carried any other POD payload than the on-board GPS receiver. In fact, only the multi-payload SAR missions Seasat, ERS-1/2 and Envisat were equipped with laser retro-reflectors (Stewart, 1988; Duchossois and Zobl, 1995; Louet, 2001), and the TerraSAR-X satellites are currently the only orbiting SAR satellites with such a payload. For other SAR satellites, the SAR instrument could offer a way to evaluate their own orbits, provided that the instrument supports accurate SAR ranging.

[1]Bin recommendations of the ILRS: https://ilrs.cddis.eosdis.nasa.gov/missions/NPT_BinSize_Recommendations.html

These consideration also raise the intriguing question if such SAR observations would support the POD and if they possibly even can contribute to the terrestrial reference frame, as it is already the case with SLR (Altamimi et al., 2016). The SAR ranges, and depending on the selected SAR imaging mode also the azimuth measurements, could support observations with more homogeneous spatial and temporal coverage than the existing SLR network (Fig. 3.4), but this comes at the expense of fewer observations per single site. From the total number of SLR normal points of the TerraSAR-X mission, it can be concluded that the subset of high quality SLR stations can provide approximately 30,000 normal points per year for a single low Earth orbiting satellite (P-IV). However, the number of observations contributed by the individual stations will differ a lot, because SLR stations with favourable atmospheric conditions (e.g., Yarragadee, Australia) commonly provide major portions of the total number of normal points (P-IV Noll and Pearlman, 2012; Arnold et al., 2018). Moreover, such an amount of observations involves a very high ILRS tracking priority, whereas satellites with lower priority naturally will have fewer measurements. On the other hand, a single Sentinel-1 satellite could in theory measure about 4,000 SAR ranges per year, when assuming the 45 SLR stations each having installed two CRs that allow observations from ascending and descending passes (Fig. 3.3b). An optimization of the CR distribution, e.g. by co-location with suitable IGS stations (Fig. 3.1), would further improve this number. Therefore, synthetic studies with hypothetical CR networks are proposed as future research to gain first insight if a SAR satellite with fewer observations per individual CR but with an advantage in spatio-temporal sampling can sustain a precise orbit. The next step would be an analysis if combined orbit and CR position solutions can make contributions to the terrestrial reference frame. The examination of such possibilities is considered important to further advance SAR imaging geodesy. It has been demonstrated in this work that the technique can meet the standards defined by GNSS and SLR, and at the same time it also provides unique features of its own for future applications that involve positioning and ranging.

4 Summary and Future Directions

The work presented in this thesis provides a comprehensive summary of SAR as an emerging geodetic technique with the primary goal to retrieve global coordinates with SAR observations. The thesis is based on six papers that provide the individual elements of the proposed methods termed SAR imaging geodesy. The core elements of the technique are the SAR observation model, the corresponding observation equations, and the least-squares approach to solve these equations for 3-D positions or the geometrical calibration parameters.

The development was inspired by the first successful tests with TerraSAR-X which demonstrated centimeter level precision for range and azimuth measurements of purposefully installed CRs. In the subsequent research, range and azimuth were further refined and turned into SAR observations enabling the novel positioning and ranging applications. The versatility of the proposed systems approach was analyzed and verified in experiments with SAR data from the currently operating missions TerraSAR-X and Sentinel-1. The results of these experiments are reported in the papers.

The SAR observation model was mainly developed based on TerraSAR-X, but in principle it is independent of the SAR sensor. The model comprises the given satellite orbit defining the datum (section 2.3.2), the mitigation of SAR hardware effects (section 2.3.3), the SAR images providing the range and azimuth observation (section 2.1), and the correction of the errors in the observation (sections 2.3.3 and 2.3.4):

- The precise orbit determination has to comply with the standards of the global geodetic reference frames to maintain a consistent datum for the SAR observations. The accuracy of the orbit solution is the main driver for the measurement accuracy that can be obtained with the corrected and calibrated observations. Consequently, the demand is for an orbit solution with centimeter or even millimeter stability.

- The hardware effects address the onboard timing system of the SAR. During mission lifetime, the short-term stable oscillator driving the SAR payload undergoes slow frequency variations that have to be monitored or may require a switch to an independent redundant unit. Moreover, the precision of the azimuth measurements should not be limited by the synchronization between the SAR payload and the absolute time provided by the on-board GPS. Analyzing the sequences of the SAR PRF along with the GNSS time can reduce this limitation, as demonstrated with TerraSAR-X.

- The SSC images generated by the SAR processor have to be rigorously processed and annotated for the orthogonal zero-Doppler geometry. Each pixel is supposed to refer to the time of closest approach (i.e. azimuth) and the two-way time of flight (i.e. range) at the time of closest approach. This requires a careful consideration of the motion effects (bistatic effects in azimuth, Doppler shifts in range) during the image generation using spectral processing methods. Otherwise, additional corrections are required, as shown for the Sentinel-1 IW products. The properly focussed SSC images make sure that range and azimuth of a point target signature can be extracted with sub-pixel precision.

- The correction of the range and azimuth observations include the atmospheric path delays and the geometric calibration constants. The calibration constants mainly account for the signal delays of the SAR hardware but also comprise other systematic errors as they are inferred from SAR measurements. The atmospheric path delays are modelled according to the GNSS standards that distinguish between ionospheric and tropospheric path delays. GNSS-based products (global ionospheric maps; receiver-based zenith tropospheric delays) and tropospheric path delays derived from operational weather models are determined as reliable sources for correcting the atmospheric path delays.

The range-Doppler equations were identified as the basic SAR observation equations, which describe the relation between the satellite trajectory, the range and azimuth observations, and the position of a point target in the global ITRF frame (section 2.3.1). The definition of target coordinates in the ITRF demands the usage of the geodynamic models associated with the reference frame. These geodynamic models describe the non-linear displacements due to tidal deformation and tectonic processes (section 2.3.5). The corresponding position model with six parameters (position vector, velocity vector) allows for the joint processing of the SAR observations that are collected on a pass-by-pass basis over time spans of months or even years. The range and azimuth calibration constants are included as additional parameters to define a comprehensive equation system for SAR geometric calibration and SAR positioning.

The solution of the non-linear range-Doppler equations applies the least squares method *adjustment of conditions with additional parameters*. However, after performing the linearization of the equations following this method, the problem can be transformed into an ordinary Gauss-Markoff model by exploiting block diagonal structures in the equation system. This simplifies the computation of the final least squares solution (section 2.4). In addition, VCE was integrated into the solution process to provide the computation with the flexibility to account for the accuracy difference of the range and azimuth observations.

The applications of SAR imaging geodesy can be derived from this least squares solution by selecting the appropriate parameter vector and re-arranging the design matrix, as discussed in the sections 2.4.1 to 2.4.3:

- The geometrical SAR calibration uses stable targets with known ITRF coordinates to estimate the range and azimuth calibration constants. Once these constants have been determined, the adjustment may be defined as an *adjustment of observations only* to analyse the residuals of range and azimuth measurements or to quantify the impact of different orbit solutions.
- The SAR positioning uses the calibrated observations of different pass geometries for the same target to estimate the coordinates in the ITRF. The solution also includes the variance-covariance matrix that describes the quality of the positioning solution. A combination of SAR observations provided by different products or payloads is readily possible.
- The differential SAR positioning resolves the difference vectors between a reference target with known ITRF coordinates and other targets contained in the same image (mutual observations at the same epoch). Depending on the spatial distance of the targets, the differential observations may reduce the need for corrections and can eliminate residual systematic biases.

The calibration of the TerraSAR-X mission and the analysis of the range and azimuth residuals are shown in P-V. After the recalibration of TSX and TSX using 7 years of high-resolution spotlight data, the SAR observations are confirmed accurate within 1-2 cm for the five CRs installed at the three geodetic observatories. The estimated standard deviations (1σ) for the range and azimuth observations read 0.9-1.5 cm and 1.5-2.5 cm, respectively. These results represent the total error budget

of the TerraSAR-X measurements and thus point out the very high quality of the SAR instrument and the underlying precise orbit solution. The findings are supported by the independent SLR validation of the orbit that covers the same period (P-IV). For the science orbit distributed with the SAR image products, the SLR residuals display a standard deviation of only 1.7 cm, and the experimental orbit solution with fixed GPS ambiguities further improves the standard deviation to 1.2 cm.

The versatility of the processing to analyse range and azimuth observations is demonstrated in P-III. The paper not only presents the applicability for different TerraSAR-X imaging modes by confirming the centimeter level accuracy for the stripmap and ScanSAR products, it also confirms an equal applicability for the Sentinel-1 mission and the IW products. Furthermore, the analysis of the Sentinel-1 measurements for the Australian CR array clarified the methods required to correct the sub-pixel distortions caused by the SAR processing effects (section 2.3.3). By additionally applying these corrections, the precision of Sentinel-1 could be assessed with 6 cm and 26 cm in range and azimuth, respectively. Provided that a recalibration of the Sentinel-1 mission can achieve the same consistency as TerraSAR-X, a global ranging accuracy of 6 cm could become possible for the Sentinel-1 IW products and CRs with 1.5 m edge-size.

Positioning results with TerraSAR-X and the CRs installed at the geodetic observatories are presented in P-I, P-II and P-V. The least squares adjustment involving VCE retains the quality of the corrected and calibrated SAR observations, which yield accurate position estimates when using the experimental TerraSAR-X orbits. On average, the results differ by 0.9 cm (north), 1.5 cm (east), and 0.8 cm (height) from the ITRF coordinates given by the terrestrial survey (P-V). The anisotropy of these remaining differences is mainly due to the geometric positioning configuration of conventional trihedral CRs that are only accessible from adjacent ascending or descending passes. The small multi-directional reflectors used in the differential positioning experiments (P-II) and the global simulations (section 3.1) clearly show the advantages when combining measurements from ascending and descending passes. The same holds true for opportunistic PS in high-resolution SAR images, albeit with a reduction in the positioning quality, commonly by a factor of 2-3 (P-I). However, they can be readily processed by the proposed methods and in future may provide the positions of point targets that are also usable as ground control points (P-I; P-VI)

The results achieved with TerraSAR-X and Sentinel-1 gradually moves SAR imaging geodesy towards a space geodetic technique. The discussion in chapter 3 point out similarities and differences between SAR, GNSS and SLR. The main assets of SAR are the all-weather and all daytime capability, the global coverage with favourable geometric configurations above 60 ° latitude, the passive ground infrastructure, the two independent observations range and azimuth, and a payload which provides these observations through images that at the same time can serve a multitude of applications in many different disciplines. While GNSS offers greater flexibility in obtaining rapid position fixes and achieves higher positioning accuracy when applying PPP, the remote sensing approach and the additional access to opportunistic PS make SAR imaging geodesy a useful addition for long-term monitoring and urban applications. Regarding the SLR, a station can in principle track every pass of TerraSAR-X. However, this is only possible if the satellite has a high SLR tracking priority and most stations will perform much less observations because of the weather dependency of the SLR technique. Therefore, regular measurements of SAR satellites of CRs co-located with geodetic stations could offer means to validate the orbit by the SAR missions themselves. This is particularly useful for SAR missions without laser retro-reflector payloads (e.g., Sentinel-1 or Radarsat-2) and with limited GNSS accuracy, e.g. single frequency receivers in low cost New Space missions.

TerraSAR-X defined the standards of SAR imaging geodesy and can be used to refine the technique and demonstrate applications as long as the mission stays operational. For future long-term applications, however, the Sentinel-1 mission offers an even more promising perspective, as most requirements for

SAR imaging geodesy are now confirmed and continuous data acquisition is ensured by the mission operation plan. Therefore, further assessments of the Sentinel-1 SAR processing effects analyzed in P-III should be performed with different SAR products, and missing elements like the CoM correction and potential limitations of the on-board time synchronization could be investigated. Of very high importance is the research on how to compute reliable atmospheric path delay corrections with a spatio-temporal resolution that allows SAR to exploit the full potential of the range and azimuth observations at a global scale. With two missions offering accurate observations, a joint processing of Sentinel-1 and TerraSAR-X can further extend the scope of SAR imaging geodesy and the design of suitable weather-resistant targets is proposed to facilitate the global applicability.

All these developments could pave the way towards SAR as a fifth independent geodetic technique, which might be able to contribute to the realization of the terrestrial reference frame next to SLR, VLBI, DORIS and GNSS. A theoretical analysis investigating this potential is therefore of interest to geodetic science. With Sentinel-1A&B in operation and the successors C&D already in preparation, this mission alone could provide a substantial amount of SAR measurements. Further candidates are Radarsat Constellation (C-band, 3 spacecraft; Lisle et al., 2018), COSMO-SkyMed Second Generation (X-band, 2 spacecraft; Sverva et al., 2015), the Gaofen-3 mission (C-band, currently 1 spacecraft; Liu et al., 2017), and a potential successor to the TerraSAR-X mission, which in principle could all contribute to such a SAR-based frame realization and enable multi-mission SAR imaging geodesy.

5 Publications

5.1 P-I: Precise Three-Dimensional Stereo Localization of Corner Reflectors and Persistent Scatterers With TerraSAR-X

Citation

C. Gisinger, U. Balss, R. Pail, X. X. Zhu, S. Montazeri, S. Gernhardt, M. Eineder, "Precise Three-Dimensional Stereo Localization of Corner Reflectors and Persistent Scatterers With TerraSAR-X", in *IEEE Transactions on Geoscience and Remote Sensing*, vol. 53, no. 4, pp. 1782–1802, April 2015. doi: 10.1109/TGRS.2014.2348859

Copyright

Summary

Spaceborne SAR allows the direct retrieval of point target coordinates, also termed 3-D localization, when using its inherent absolute ranging capability. The paper presents the methods for SAR data reduction, the requirements for SAR image processing, and the algorithm developed for positioning, which applies least squares estimation methods to solve arbitrary stereo configurations. Data from the TerraSAR-X mission is used for practical demonstration.

Starting with the radar timings range and azimuth extracted from the SAR images, the observations for the 3-D positioning algorithm are obtained by correcting both timings for the errors induced by the atmospheric delay and the tidal dynamics of the solid Earth. Moreover, the need for consistent SAR processing, which avoids generally applied approximations during the image generation, and a careful geometrical calibration are discussed and demonstrated with the results. Precise orbit determination of the SAR satellite is also considered important because the proposed positioning method relies on the direct usage of the orbit trajectory together with the corrected range and azimuth observations.

Removing the errors caused by the atmosphere and the geodynamic Earth is the key to achieve precise positioning solutions. The paper outlines the use of complementary GNSS observations or GNSS-based products to eliminate the atmospheric path delay from the SAR observations for both the ionosphere and the troposphere. The handling of the geodynamic displacement is in line with the standards of the ITRF listed in the IERS conventions. All the displacement effects are shortly described and taken into account as part of the computations.

The results show positioning solutions for TerraSAR-X at several locations and with different configurations. Analyses from three test sites with large 1.5 m and 0.7 m trihedral CRs, i.e. the geodetic

stations Wettzell, GARS O'Higgins, and Metsähovi, confirm that the procedure allows to retrieve coordinate solutions with an estimated precision of 4-5 cm (95% confidence level). Moreover, the stations Wettzell and Metsähovi provide millimeter level reference coordinates for the CRs from a terrestrial survey of the local ties. After geometrical recalibration of the SAR systems, the comparison with these independent reference coordinates shows differences at the 2-3 cm level. This underlines the potential of SAR for direct 3-D coordinate determination.

In principle, the method is equally applicable to opportunistic PSs, but the example given for the city of Berlin shows that the typical positioning quality is a factor of 2-3 worse when compared to the ideal case CRs. An interesting possibility, however, are the scatters (e.g., lamp poles) providing multi-directional backscatter. They allow the combination of ascending and descending passes and in principle a very high precision for the estimated position. These PSs became part of the TomoSAR study presented in P-IV.

The paper concludes with a discussion on the application of such SAR-based coordinates, either stemming from artificially installed CRs or opportunistic PSs, which may be used in future to geocode SAR data, fuse the results of the relative phase-based SAR methods (PSI, TomoSAR), or support the integration of SAR into GNSS networks.

Declaration of contributions

The idea of using SAR for precise point positioning was proposed by C. Gisinger. He developed the SAR positioning algorithm and carried out the implementation along with the correction scheme to fully correct the SAR data for all external error sources according to the geodetic standards of the IERS. The study sites hosting the corner reflectors were established as part of the DLR and TUM cooperation DLR@Uni, managed by M. Eineder in order to analyze the geometrical quality of the TerraSAR-X mission and its potential for geodetic applications. The preprocessing of the SAR data was performed by U. Balss, who also contributed the section III-A on the systematic satellite effects. S. Montazeri and X. Zhu suggested the testing of the method for PS at the Berlin test site, and S. Montazeri conducted the manual extraction of the raw SAR observations from the image stacks, with support in the data preparation given by S. Gernhardt. The publication including the graphics and the tables was compiled by C. Gisinger, with the co-authors contributing through feedback and the discussion of the results. The draft manuscript was finalized by C. Gisinger taking into account the detailed comments and corrections given by R. Pail and M. Eineder.

5.2 P-II: Differential geodetic stereo SAR with TerraSAR-X by exploiting small multi-directional radar reflectors

Citation

C. Gisinger, M. Willberg, U. Balss, T. Klügel, S. Mähler, R. Pail, M. Eineder, "Differential geodetic stereo SAR with TerraSAR-X by exploiting small multi-directional radar reflectors", in *Journal of Geodesy*, vol. 91, no. 1, pp. 53–67, 2017. doi: 10.1007/s00190-016-0937-2

Copyright

Summary

Similar to the concept of differential GNSS, the publication reports on the use of differential stereo SAR methods to determine the coordinates of point targets. To test this novel differential approach, a positioning experiment was performed at Wettzell geodetic observatory, Germany, using small multi-directional radar reflectors and the staring spotlight mode of TerraSAR-X offering a very high resolution of 0.6 m by 0.24 m in range and azimuth. The small of-the-shelf reflectors, referred to as octahedrons, are diamond-shaped arrangements of eight trihedral CRs (edge of 0.23 m) grouped around a common phase center.

The algorithm on absolute SAR positioning originally presented in P-I is briefly recapped and extended for the differential case. The differential case requires multiple reflectors in the SAR scene and a priori known reference coordinates for at least one of the reflectors, which enables the differential positioning for the remaining reflectors by solving a modified stereo problem to estimate the 3-D difference vectors. The major advantage compared to standard SAR position is the cancellation of the errors in the differential SAR measurements (system biases, atmospheric path delay, solid Earth geodynamic signals), for which spatial correlation is assumed within the limited ground coverage (5-10 km) of high-resolution SAR scenes. Mathematically speaking, the differential case is the application of the difference operator on the linearized system of SAR range-Doppler equations. Thus, the methods used to solve the standard positioning case can be also applied to the differential approach.

Four octahedrons were placed at Wettzell from July 2015 to November 2015. With their reference coordinates known from on-site terrestrial survey, SAR-based solutions of their coordinates were determined with TerraSAR-X with the standard and the differential positioning method. One of the large 1.5 m CRs permanently installed at Wettzell was included for comparison. For the experiment TerraSAR-X acquired 12 images (4 staring spotlight, 8 high-resolution spotlight), which comprise three geometries and both pass directions (ascending & descending).

The positioning results with the standard method using the a priori corrected SAR observations (path delays, geodynamic displacements, geometrical calibration) confirm the advantage of multi-directional octahedrons over common CRs. Although the precision of the SAR observation is less for the smaller octahedrons (e.g., for staring spotlight the estimated precision reads ±1.3 cm vs. ±0.9 cm in range and ±3.3 cm vs. ±2.6 cm in azimuth), the estimation of the coordinates is more reliable. Because of the combination of both pass directions, the octahedron coordinates are estimated with a uniform precision

(95 % confidence) of 2-3 cm, while for the CR and the given amount of data the precision is only at the decimeter level, with the height component showing the largest value. The accuracy derived from the comparison with the reference coordinates matches the precision save for a significant 4 cm offset found in the height component of the octahedrons for which no concluding cause was identified.

The differential method omitting the *a priori* corrections improves in the observation precision and the height offset is removed by the differential configuration introducing a known reference reflector. The coordinates found for the remaining three octahedrons have less than 3 cm difference to the reference values and the precision estimates do not exceed ±2.2 cm. The results confirm the applicability of the differential stereo SAR method and demonstrate the usefulness of variance component estimation for radar data. It allows not only for the proper weighting of the range and azimuth observations but also for the different SAR imaging modes, e.g., the staring spotlight and high-resolution spotlight used in the experiment.

In its conclusions, the paper emphasizes the flexibility of the least squares based approach for different SAR positioning methods and the octahedron design is recommended for positioning applications. If reliable reference coordinates are available in a multi-reflector network, the differential approach should be considered as an alternative, in particular for configurations that combine radar reflectors with permanent GNSS.

Declaration of contributions

The experiment of testing the small octahedron reflectors with TerraSAR-X was jointly devised by DLR (M. Eineder, U. Balss) and TUM (R. Pail, C. Gisinger). M. Willberg performed the installation and processed the standard case during his master thesis under the supervision of C. Gisinger. On-site maintenance and terrestrial survey of the reflectors was carried out by T. Klügel and S. Mähler, respectively. M. Willberg was supported in the data preprocessing (extraction of the radar timings) by U. Balss. C. Gisinger extended the positioning algorithm for the differential case and devised the scope of the publication. The writing, the compilation of the results, and the analysis were all done by C. Gisinger, with the co-authors contributing during the process through discussions and clarifications. M. Eineder and R. Pail revised and commented the draft manuscript before submission.

5.3 P-III: In-Depth Verification of Sentinel-1 and TerraSAR-X Geolocation Accuracy using the Australian Corner Reflector Array

Citation

C. Gisinger, A. Schubert, H. Breit, M. Garthwaite, U. Balss, M. Willberg, D. Small, M. Eineder, N. Miranda, "In-Depth Verification of Sentinel-1 and TerraSAR-X Geolocation Accuracy using the Australian Corner Reflector Array", in *IEEE Transactions on Geoscience and Remote Sensing*, accepted December 2019, in publication, 2019.

Copyright

Summary

The publication addresses the 2-D geolocation analysis of Sentinel-1A/B based on the Australian CR array in Queensland, Australia, that consists of 40 individual reflectors with a dimension of 1.5 m or larger. Based on the consistent description of the geometric SAR processing methods and standards, particularly the Sentinel-1 specific requirements, the analysis was performed by groups of DLR/TUM and UZH using their own software implementations. This allowed the cross-comparison of independently generated results. The study additionally involves the TerraSAR-X mission, which was already verified and calibrated in earlier studies (see P-I and P-V), and thus enabled an independent validation for the CR installations and the presented methods. The TerraSAR-X results not only provide a direct comparison for the outcomes achieved with Sentinel-1. At the same time, the results also demonstrate the practical application for absolute SAR range and azimuth processing.

Besides a summary of the geolocation procedure describing the steps – reflector selection, installation and survey, point target analysis, atmospheric path delay computation, geodynamic signal correction, prediction of reference timings, and geolocation analysis – the methodological part mainly focuses on the bistatic SAR effects associated with the movement of satellite during signal transmission and echo reception. These effects are ideally compensated for by the SAR processor when forming the level 1b images, which is the case for TerraSAR-X. For Sentinel-1 the corrections need to be applied in post-processing when using the standard IW product. These specific Sentinel-1 bistatic corrections comprise the bistatic azimuth effects and the Doppler shift in range. Moreover, potential azimuth shifts due to the mismatch of the azimuth Doppler FM rate during focusing have to be taken into account. The paper presents comprehensive derivations of the three correction formulas as well as their computation in practice using the Sentinel-1 product annotations.

The SAR data sets used in the study consist of TerraSAR-X stripmap and ScanSAR images as well as Sentinel-1 IW images, which were acquired during October 2014 and March 2018. Moreover, the 40 CR installations are documented in detail, addressing key aspects like long-term stability, boresight orientation, or the survey of the CR phase centers with GNSS. The latter was performed in an indirect manner, which requires an additional transformation to compute the phase center reference coordinates from the surveyed coordinates. The verification of the transformations, which have been

inferred from engineering drawings of the mounts and the alignments of the CRs, was one of the motivations to use TerraSAR-X in the study.

The TerraSAR-X geolocation results with stripmap confirm the applicability of the CR phase center transformations. The results with and without correcting the reference coordinates are in line with the expectations. With the surveyed coordinates systemic biases remain in range that differ with respect to CR size and the imaging geometry. They are reliably removed when applying the transformations. The corresponding numbers (mean and standard deviation, 1σ) for the 11 CRs tested with TerraSAR-X stripmap read -0.9 $\pm$ 3.5 cm in range and -2.4 $\pm$ 3.4 cm in azimuth. The additional validations performed across the whole array using the TerraSAR-X ScanSAR data confirm the high quality of the overall array installation. The total geolocation result (40 CRs) was determined with 0.9 $\pm$ 4.6 cm (range) and 0.4 $\pm$ 10.0 cm (azimuth). A small systematic distortion in the order of a few centimeters was found in the azimuth residuals of TerraSAR-X ScanSAR across the different CRs, which depends on the location of the CR in the ScanSAR burst and is related to the TerraSAR-X product itself. The cause could not be identified within the study, therefore this effect is subject to further investigations.

In comparison to SAR geolocation verification using only small numbers of reflectors, an entire CR array enables a detailed experimental analysis for the geolocation quality of SAR products. Therefore, the three Sentinel-1 specific corrections could be directly assessed on behalf of the S1B data, for which the corrections are demonstrated to precisely replicate the systematic distortions and swath-dependent biases found in the Sentinel-1 azimuth and range residuals. Removal of the effects in the geolocation processing leads to improvements in the standard deviations of range and azimuth by factors of four and two, respectively. This yields a geolocation precision for the Sentinel-1 IW product of 6 cm in range and 26 cm in azimuth. Moreover, the bistatic corrections in azimuth remove the 2-3 m biases in the azimuth residuals. Ultimately, there remain offsets at the centimeter to decimeter level in azimuth and range for S1A and S1B. If proven stable and site independent, these offsets can be adjusted by satellite specific calibration constants that account for uncompensated contributions in the SAR systems, e.g., the internal signal delays of SAR electronics.

The Sentinel-1 geolocation computed by DLR/TUM and UZH are in close agreement. The only substantial difference is found in the average range offsets which differ by approximately 13 cm for both S1A and S1B. Their cause lies in the different methods for correcting the atmospheric path delay used by the two groups, specifically the mapping of the ionosphere delay. Additional Sentinel-1 findings discussed in the paper include the differences found for the images acquired in VV and HH polarization and the impact of the electronic failure of the S1A SAR antenna tile #11 in June 2016 on the geolocation results of S1A.

The paper concludes with a theoretical assessment of the individual error contributions in the TerraSAR-X and Sentinel-1 SAR systems. In range, both missions are considered close to the limit defined by the path delay corrections and the SCR of the reflectors in the given products. Regarding the azimuth, the main limitation stems from the SCR and the coarser azimuth resolution of ScanSAR and IW products. Small room for improvement potentially remains in the orbits (for TerraSAR-X, see P-IV), as well as in a few of the CR reference coordinates. Five reflectors with average range offsets larger than the 4 cm accuracy estimated from the GNSS survey could be commonly identified in the results of both missions. The final conclusions emphasize the progress made in geolocation with the Sentinel-1 products, the abilities of SAR geolocation as an absolute measurement technique, and the unique possibilities given by the Australian CR array.

Declaration of contributions

The study presented in the paper was part of the project "Fiducial Reference Measurements for SAR Geometric Calibration and Performance Assessment" commissioned by ESA and supervised by N. Miranda (ESA Contract No. 4000119113/16/I-EF). The scope of the project was jointly conceived by DLR, TUM, and UZH and involved close cooperation with Geoscience Australia (GA) responsible for the array installation. The design of the study is the joint work of all authors.

N. Miranda commissioned the reprocessing of the Sentinel-1 data used in the study. The installation of the array was supervised by M. Garthwaite, who provided the reference coordinates of the CRs. H. Breit and U. Balss conceived the theory behind the Sentinel-1 specific corrections. C. Gisinger computed the TerraSAR-X results with support given by U. Balss and the DLR/TUM results of Sentinel-1 including the analysis of the Sentinel-1 specific processing effects. Support in the implementations regarding Sentinel-1 was given by U. Balss and M. Willberg. The Sentinel-1 result of UZH were computed by A. Schubert.

C. Gisinger integrated the overall manuscript and prepared several parts of the text, specifically the introduction, most of the geolocation procedure, the description of the data sets, as well as most of the writing in the result and discussion section. The general aspects of CR installations were described by A. Schubert and D. Small, along with contributions in the geolocation procedure and in the discussion of the Sentinel-1 results. H. Breit and U. Balss prepared the section on the motion-related effects in SAR data processing. M. Garthwaite contributed the documentation of the Australian reflector array. All authors contributed in the finalization of the manuscript prior to submission, notably M. Garthwaite and M. Eineder, who provided detailed revisions and comments to the draft manuscript.

5.4 P-IV: Long-Term Validation of TerraSAR-X and TanDEM-X Orbit Solutions with Laser and Radar Measurements

Citation

S. Hackel, C. Gisinger, U. Balss, M. Wermuth, O. Montenbruck, "Long-Term Validation of TerraSAR-X and TanDEM-X Orbit Solutions with Laser and Radar Measurements", in *Remote Sensing*, vol. 10, no. 5, pp. 1–20, 2018. doi: 10.3390/rs10050762

Copyright

Summary

The publication reports on the evaluation of enhanced TSX and TDX orbit solutions over a period of six years. The newly generated orbit solutions involve updates in the dynamic force modeling (satellite macro model, usage of atmospheric density and wind models) as well as the estimation of integer ambiguities in the processing of the on-board GPS observations. The GPS and the dynamic models are combined in a reduced dynamic orbit determination (RDOD) approach. Compared to the presently available Precise Science Orbits (PSOs), the enhanced orbits are considered a substantial improvement and therefore the paper focuses on independent orbit validation using the two different techniques SLR and SAR. The re-determination of the TerraSAR-X orbits was motivated by the advancements made in the range and azimuth measurements (see P-I and P-II), which demand for very high orbit accuracy and thus have become sensitive enough to enable an independent orbit analysis, a first regarding the use of SAR data. In addition, the well-established technique of SLR was used for the detailed assessment of both the standard PSOs and the enhanced orbit solutions. The SAR data comprises more than 1000 radar scenes from five different corner reflectors located at three geodetic stations, whereas for the SLR the TerraSAR-X mission benefits from the high tracking priority within the ILRS. During the six years study period, a total amount of approximately 200,000 normal points per spacecraft was collected by the eleven SLR stations selected for the analysis.

The validation results of both methods confirm the improvement achieved with the latest enhanced orbit solution. Based on the normal point statistics across all stations, the SLR shows a reduction in standard deviation (1σ) from 16.9 mm to 11.4 mm (TSX) and from 17.5 mm to 12.5 mm (TDX) when using the new orbits. The corresponding mean values do not exceed 1.7 mm which is a testimony to the consistency of SLR and the underlying ITRF. The outcomes of SAR agree with the findings of the SLR. The standard deviations in the SAR ranges decrease from 15.1 mm to 12.5 mm (TSX) and from 16.9 mm to 14.9 mm (TDX). The same behavior applies to SAR azimuth, but because of the larger azimuth noise level the results are scaled by roughly a factor of 1.6 when compared to the range. As for the mean offsets that are driven by the SAR payload calibration constants, both satellites achieve higher consistency with the enhanced orbit solutions for which the offsets remain below 5 mm (range) and 7 mm (azimuth).

Moreover, the decomposition of the SLR residuals into monthly radial, along-track and across-track orbit position offsets reveals that the improvement of the enhanced solutions is mostly stemming

from the cross-track component. Compared to the PSOs, the cross-track offsets are reduced from approximately -11 mm to less than 1 mm for both TSX and TDX. Because of the limitations of the permanently right-looking geometry and the considerably smaller number of observations, the SAR residuals could not be reliably processed for monthly position offsets. However, the monthly range and azimuth analysis presented in the paper remains in line with the SLR assessment.

In the final conclusions, the paper points out the successful validation of the enhanced orbit solution with two independent techniques, which confirm the very high accuracy of the solutions. This makes the enhanced orbit a reliable basis for TerraSAR-X SAR applications using direct range and azimuth observations.

Declaration of contributions

S. Hackel and C. Gisinger devised the idea for a comparative SLR and SAR-based orbit analysis of the latest TerraSAR-X orbit solutions computed by S. Hackel. The SAR results using the different orbit solutions were computed by C. Gisinger. The manuscript was jointly prepared by S. Hackel and C. Gisinger, for which C. Gisinger contributed the SAR-related parts, including the corresponding figures and tables. Specifically, C. Gisinger wrote parts of the introduction, the entire sections 4.2 and 5.2, and he contributed parts of the result discussion and the conclusions. He also provided comments and corrections for the overall manuscript.

5.5 P-V: Measurements on the Absolute 2-D and 3-D Localization Accuracy of TerraSAR-X

Citation

U. Balss, C. Gisinger, M. Eineder, "Measurements on the Absolute 2-D and 3-D Localization Accuracy of TerraSAR-X", in *Remote Sensing*, vol. 10, no. 4, pp. 1–21, 2018. doi: 10.3390/rs10040656

Copyright

Summary

Following the methods first published in detail in P-I, the paper presents the latest results in 2-D and 3-D localization with TSX and TDX. The main focus lies on the 2-D geolocation validation, which makes use of the largely increased amount of SAR data for the three TerraSAR-X test sites – Wettzell, GARS O'Higgins, and Metsähovi – that have become available since the initial results for these test sites were reported in P-I in 2015. In total, the data set used in this paper comprises more than 1000 high-resolution spotlight images that were acquired over a period of 7 years and contains 12 different imaging geometries.

With the reference coordinates of all the five CR now given by terrestrial geodetic survey, the 2-D geolocation could be analyzed with respect to incidence angles, temporal stability, and consistency of geometrical calibration constants. For the latter, the impact of polarization was experimentally quantified, showing differences of 4 cm in range between the images acquired in HH and VV channels, which match the staggered SAR antenna structures containing the HH and VV transmit/receive elements. Regarding the incidence angles, no obvious patterns were identified for the measurement series of the different geometries. Almost all the range and azimuth offsets remain within 1-2 cm, whereas the corresponding standard deviations vary between 0.9 cm and 1.9 cm for range and 1.5 cm and 2.5 cm for azimuth. The larger values were mostly determined for GARS O'Higgins and are related to the smaller CR size of 0.7 m. The CRs at the other test sites have sizes of 1.5 m. In order to assess the temporal stability, a linear model was estimated for the SAR residuals of each site. Small trends of 3-5 mm/y could be determined in range and azimuth for which the results in range are considered significant. Isolating the cause becomes difficult because several effects might contribute at this level. Since the SLR validation confirmed the long-term stability of the TerraSAR-X orbit product and the CR installations are assumed stable, the SAR payloads themselves are named as the most plausible cause.

In terms of the 3-D positioning of the CRs with stereo SAR, reliable ITRF coordinate solutions could be determined, which show estimated standard deviations (95% confidence) of 1-4 cm. As expected, the larger standard deviations are driven by the stereo geometry and are found for the CRs that are captured in same side dual-geometry instead of same side triple-geometry. Moreover, the comparison of the SAR-based coordinates with the independently determined reference coordinates confirms the 3-D positioning to be accurate within 2-4 cm.

In the result discussion, the paper quantifies the individual error contributions stemming from the clutter, the troposphere, the ionosphere, the on-board timing system, and the orbit. The science orbit annotated to the SAR products is considered a possible source for larger error contribution. However, given the experimentally obtained geolocation results, the impact can not be larger than 1-2 cm, whereas the other effects are expected to contribute at the millimeter level. Indications for the impact of the orbit are given by the results using the new enhanced TerraSAR-X orbit (see P-IV). When looking at the larger 1.5 m CRs, the 2-D geolocation demonstrates an improvement of 15 % in azimuth and 28 % in range compared to the science orbits. For the 3-D positioning, particularly the height estimation can benefit from the improvement achieved in the range measurements. These findings mark the best absolute measurements presently achievable with the TerraSAR-X system, and the overall conclusions emphasize the very high quality of the mission for applications like the generation of ground control points or the synergetic use with the phase-based methods, e.g., SAR tomography.

Declaration of contributions

C. Gisinger contributed the parts of paper that are related to 3-D localization. This include the theory, the computation of the results, and the result discussion, along with the corresponding figures and tables. Moreover, he prepared the corrections (atmospheric path delays, geodynamic signals) used in the processing of both the 2-D geolocation validation and the 3-D localization. Prior to submission, C. Gisinger performed revisions and corrections throughout the entire draft manuscript.

5.6 P-VI: Geodetic SAR Tomography

Citation

X. X. Zhu, S. Montazeri, C. Gisinger, R. F. Hanssen, R. Bamler, "Geodetic SAR Tomography", in *IEEE Transactions on Geoscience and Remote Sensing*, vol. 54, no. 1, pp. 18–35, 2016.
doi: 10.1109/TGRS.2015.2448686

Copyright

Summary

Phase-based SAR methods like PSI and TomoSAR require at least one PS with a priori known reference coordinates. Insufficient knowledge of the reference PS limits the coordinate quality of the PS point clouds (imprecise geocoding) and leads to errors when combining PS point clouds from different image stacks. On the other hand, the geodetic stereo SAR outlined in P-I allows for the direct retrieval of absolute ITRF coordinates of PS. The combination of this method with the TomoSAR should improve the geocoding and at the same time resolve the fusion of PS point clouds originating from different geometries. In the publication this novel approach was tested with four TerraSAR-X data stacks acquired for the city of Berlin. A lamp pole visible in all the stacks was identified and its coordinates were retrieved by stereo SAR with an estimated 3-D precision (1σ) of 1 cm and an assumed accuracy of 10 cm. The latter needs to be assumed because the unknown diameter of the lamp pole was neglected in computation of the stereo SAR solution, and was only approximately compensated for in post-processing. Nevertheless, the well-determined reference point enabled the computation of corrections for the geocoding of the TomoSAR solutions, which resulted in a high-quality fusion of the four point clouds.

The results shown in the paper present the global coordinates of approximately 63 million PSs that give a detailed representation of the Berlin city center and cover an area of 10 km by 5 km. The comparison with a laser scanning (LiDAR) digital surface model with a reported 3-D accuracy of about 10cm shows a horizontal accuracy for the SAR solution in the order of 20-30 cm and a vertical accuracy at the meter level. This is typical for the phase-based TomoSAR. Overall, the results confirm the effectiveness of the proposed method. In the outlook the publication recommends additional research in the efficient detection multi-direction PSs serving the stereo SAR and the TomoSAR PS cloud fusion, as well as further cross-validations of these points using GNSS.

Declaration of contributions

Parts of the study as presented in the publication were conceived by C. Gisinger in the discussions with X. Zhu during the joint supervision of the Master Thesis of S. Montazeri. For the publication, C. Gisinger performed the stereo SAR processing of the PS candidates identified and prepared by S. Montazeri for absolute positioning. The section II of the paper was written by C. Gisinger and he provided figures and tables to the manuscript which was prepared and integrated by X. Zhu.

Acknowledgments

This thesis would not have been possible without the support of the many people who accompanied me during the years it took to complete this work. They contributed to the final outcome in a large variety of ways, not only by sharing knowledge or providing support with data and methods, but also by giving inspiration and motivation, by sharing activities that had absolutely nothing to do with work but created the much needed diversion from the daily business, and by simply making this research an interesting and worthwhile journey. My first thanks go to Roland Pail and Michael Eineder who gave me the opportunity to delve into this topic, first in the joint project work at TUM and later as a researcher at DLR, and who supervised this thesis and provided guidance and support when it finally was about time to bring the material into publishable shape. I would like to thank Hannes Raggam from Joanneum Research who unknowingly laid the foundations for my thesis by passing on his knowledge on SAR and radargrammetry in his lectures at Technical University of Graz, which inspired the methods that are at the core of this work. Many thanks go to the colleagues and people at TUM-APG, TUM-FSG and TUM-LMF. Especially to Urs Hugentobler, who answered many questions on the details of GNSS and whose enthusiasm in research and teaching is an inspiration to countless students, to Peter Steigenberger for giving insight into Bernese and GNSS processing, to Anja Schlicht for the motivation through the bi-weekly research discussions and the astronomic endeavors in our preparation of the geodetic Astronomy lecture, and to Stefan Auer and Stefan Gernhardt for our joint study at TUM campus in which we discovered the challenges of SAR with seemingly simple buildings. A special thanks goes to Christian Ackermann, who shared the office with me for several years as well as my passion for photography, which led to the discovery of many hidden places at TUM campus and in the city of Munich and its surroundings. Furthermore, I would like to thank Ulrich Balss for his infinite patience in explaining the details of SAR processing in extensive email conversations, and the ordering and distribution of large a number of TerraSAR-X images, and Helko Breit for the numerous discussions about the uncharted depths of SAR focussing algorithms. I thank Stefan Hackel from GSOC who confirmed and enhanced the quality of the TerraSAR-X orbit, which provide the basis for all the results. Also many thanks to all the colleagues from SAR-MF, particularly those who share the daily lunch and coffee breaks, which often bring up fancy discussions across a large variety of subjects. The experiments of this work rely on high quality ground infrastructure and scientific cooperation, which is only possible because of the commitment of many people in different institutions around the world. Therefore, my thanks go to Thomas Klügel and Svetlana Mähler from BKG at Wettzell, to Markku Poutanen and Jyri Näränen from NLS-FGI, to the colleagues at the GARS O'Higgins Antarctic station, and to Matt Garthwaite and his colleagues from Geoscience Australia, who share our view on the potential of SAR in geodesy and invested many hours of work to establish and maintain some of the best SAR calibration sites currently available. I also thank Adrian Schubert and David Small from University of Zurich for the cooperation in our investigation of the Sentinel-1 data, and Nuno Miranda from ESA who recognizes the value of science for the Sentinel-1 mission. This work was part of the DLR@Uni Munich Aerospace project 'High-Resolution Geodetic Earth Observation' funded by the German Helmholtz Association and the project 'FRM4SAR' funded by ESA, for which I want to express my thanks to both organizations. Finally, I would like to thank my family, my parents Norbert and Karin who supported me throughout all my years of study, first in Graz and then in Munich, and who encouraged me to pursue a career in scientific research, and my sister Sonja who also works in science at DLR and shares many of my free time activities, and who is above all an invaluable bicycle mechanic for several people at DLR, myself included.

List of Figures

Bibliography

M. M. Alizadeh, D. D. Wijaya, T. Hobiger, R. Weber, and H. Schuh. *Ionospheric Effects on Microwave Signals*, pages 35–71. in Atmospheric Effects in Space Geodesy, Böhm, J. and Schuh, H. (Editors), Springer-Verlag Berlin Heidelberg, 2013. doi: 10.1007/978-3-642-36932-2_2.

Z. Altamimi, P. Rebischung, L. Métivier, and X. Collilieux. ITRF2014: A new release of the International Terrestrial Reference Frame modeling nonlinear station motions. *Journal of Geophysical Research*, 121(8):6109–6131, 2016. doi: 10.1002/2016JB013098.

Z. Altamimi, L. Métivier, P. Rebischung, H. Rouby, and X. Collilieux. ITRF2014 plate motion model. *Geophysical Journal International*, 209(3):1906–1912, 2017. doi: 10.1093/gji/ggx136.

D. Arnold, O. Montenbruck, S. Hackel, and K. Sośnica. Satellite laser ranging to low Earth orbiters: orbit and network validation. *Journal of Geodesy*, Online First, 2018. doi: 10.1007/s00190-018-1140-4.

ASI. COSMO-SkyMed Mission - COSMO SkyMed SAR PRODUCTS HANDBOOK. Italian Space Agency (ASI), ASI Technical Note, Doc. ASI-CSM-ENG-RS-092-A, Rev. A, Date 30.04.2007, 2007.

U. Balss, X. Y. Cong, R. Brcic, M. Rexer, C. Minet, H. Breit, M. Eineder, and T. Fritz. High Precision Measurement on the Absolute Localization Accuracy of TerraSAR-X. In *Proceedings of IGARSS'12 Conference, July 22–27, Munich, Germany*, pages 1625–1628, 2012. doi: 10.1109/IGARSS.2012.6351217.

U. Balss, C. Gisinger, X. Y. Cong, R. Brcic, P. Steigenberger, M. Eineder, R. Pail, and U. Hugentobler. High Resolution Geodetic Earth Observation with TerraSAR-X: Correction Schemes and Validation. In *Proceedings of IGARSS'13 Conference, July 21–26, Melbourne, Australia*, pages 4499–4502, 2013. doi: 10.1109/IGARSS.2013.6723835.

U. Balss, H. Breit, T. Fritz, U. Steinbrecher, C. Gisinger, and M. Eineder. Analysis of internal timings and clock rates of TerraSAR-X. In *Proceedings of IGARSS'14 Conference, July 13–18, Quebec City, Canada*, pages 2671–2674, 2014. doi: 10.1109/IGARSS.2014.6947024.

R. Bamler and M. Eineder. Accuracy of Differential Shift Estimation by Correlation and Split-Bandwidth Interferometry for Wideband and Delta-k SAR Systems. *IEEE Geoscience and Remote Sensing Letters*, 2(2):151–155, 2005. doi: 10.1109/LGRS.2004.843203.

R. Bamler and P. Hartl. Synthetic aperture radar interferometry. *Inverse Problems*, 14:1–54, 1998. doi: 10.1088/0266-5611/14/4/001.

D. Bilitza and B. W. Reinisch. International Reference Ionosphere 2007: Improvements and new parameters. *Advances in Space Research*, 42:599–609, 2008. doi: 10.1016/j.asr.2007.07.048.

J. Böhm and H. Schuh, editors. *Atmospheric Effects in Space Geodesy*. Springer-Verlag Berlin Heidelberg, 2013. doi: 10.1007/978-3-642-36932-2.

J. Böhm, B. Werl, and H. Schuh. Troposphere mapping functions for GPS and VLBI from ECMWF operational analysis data. *Journal of Geophysical Research*, 111(B02406), 2006. doi: 10.1029/2005JB003629.

J. Böhm, D. Salstein, M. M. Alizadeh, and D. D. Wijaya. *Geodetic and Atmospheric Background*, pages 1–33. in Atmospheric Effects in Space Geodesy, Böhm, J. and Schuh, H. (Editors), Springer-Verlag Berlin Heidelberg, 2013. doi: 10.1007/978-3-642-36932-2_1.

M. Bourbigot, H. Johnsen, and R. Piantanida. Sentinel-1 Product Definition. Technical note by Sentinel-1 Mission Performance Center (MPC), Doc. S1-RS-MDA-52-7440, Iss. 2, Rev. 6, Date 22.07.2015, Available: https://sentinel.esa.int/web/sentinel/user-guides/document-library, 2015.

M. Bourbigot, H. Johnsen, and Piantanida R. Sentinel-1 Product Specification. Technical note by Sentinel-1 Mission Performance Center (MPC), Doc. S1-RS-MDA-52-7441, Iss. 3, Rev. 3, Date 14.10.2016, Available: https://sentinel.esa.int/web/sentinel/user-guides/document-library, 2016.

H. Breit, T. Fritz, U. Balss, M. Lachaise, A. Niedermeier, and M. Vonavka. TerraSAR-X SAR Processing and Products. *IEEE Transactions on Geoscience and Remote Sensing*, 48(2):727–740, 2010. doi: 10.1109/TGRS.2009.2035497.

C. Bruyninx, A. Araszkiewicz, E. Brockmann, A. Kenyeres, J. Legrand, T. Liwosz, P. Mitterschiffthaler, R. Pacione, W. Söhne, and Völksen. EUREF Permanent Network Technical Report 2017. *in IGS Technical Report 2017, Villiger, A. and Dach, R. (Editors), Bern Open Publishing*, pages 105–115, 2017. doi: 10.7892/boris.116377.

S. Buckreuss, B. Schättler, T. Fritz, J. Mittermayer, R. Kahle, E. Mauer, J. Böer, M. Bachmann, F. Mrowka, E. Schwarz, H. Breit, and U. Steinbrecher. Ten Years of TerraSAR-X Operations. *Remote Sensing*, 10(873):1–28, 2018. doi: 10.3390/rs10060873.

S. Byram, C. Hackman, and J. Tracey. Computation of a High–Precision GPS–Based Troposphere Product by the USNO. Proceedings of the 24th Int. Technical Meeting of The Satellite Division of the Institute of Navigation (ION GNSS 2011), Portland, OR, 2011.

D. Calabrese, C. Germani, A. Torre, D. Rizzato, S. Federici, R. Formaro, G. Natale, and C. Facchinetti. CSG Status and New Solutions to Increase the Product Portfolio. In *Proceedings of EUSAR 2018 Conference, June 04-07, Aachen, Germany*, pages 300–305, 2018.

M. Chabot, D. Decoust, C. Lambert, P. Rolland, P. Ledantec, and D. Williams. RADARSAT-2 System Operations and Performance. In *Proceedings of IGARSS'15 Conference, July 26–31, Milan, Italy*, pages 1512–1515, 2015. doi: 10.1109/IGARSS.2015.7326067.

P. H. Chen and I. J. Dowman. Space Intersection from ERS-1 Synthetic Aperture Radar Images. *Photogrammetric Record*, 15(88):561–573, 1996. doi: 10.1111/0031-868X.00064.

P. H. Chen and I. J. Dowman. SAR Image Geocoding using a Stereo-SAR DEM and Automatically Generated GCPs. *International Archives of Photogrammetry and Remote Sensing*, XXXIII:38–45, 2000.

P. H. Chen and I. J. Dowman. A Weighted Least Squares Solution for Space Intersection of Spaceborne Stereo SAR Data. *IEEE Transactions on Geoscience and Remote Sensing*, 39(2):233–240, 2001. doi: 10.1109/36.905231.

A. Coletta, G. Angino, F. Battazza, F. Caltagirone, F. Impagnatiello, G. Valentini, A. Capuzi, S. Fagioli, and R. Leonardi. Cosmo-SkyMed Pogramm: Utilization and Description of an Advanced Space EO Dual-Use Asset. In *Proceedings of Evisat Symposium 2007, April 23-27, Montreux, Switzerland*, pages 1–6, 2007.

L. Combrinck. *Satellite Laser Ranging*, pages 301–338. in Sciences for Geodesy I, Xu, G. (Editor), Springer Berlin Heidelberg, 2010. doi: 10.1007/978-3-642-11741-1_9.

L. Combrinck. *General Relativity and Space Geodesy*, pages 53–95. in Sciences for Geodesy II, Xu, G. (Editor), Springer Berlin Heidelberg, 2013. doi: 10.1007/978-3-642-28000-9_7.

X. Cong, U. Balss, M. Eineder, and T. Fritz. Imaging geodesy - Centimeter-Level Ranging Accuracy With TerraSAR-X: An Update. *IEEE Geoscience and Remote Sensing Letters*, 9(5):948–952, 2012. doi: 10.1109/LGRS.2012.2187042.

X. Cong, U. Balss, F. R. Gonzalez, and M. Eineder. Mitigation of Tropospheric Delay in SAR and InSAR Using NWP Data: Its Validation and Application Examples. *Remote Sensing*, 10(1515): 1–21, 2018. doi: 10.3390/rs10101515.

M. Crossetto, O. Monserrat, M. Cuevas-González, N. Devanthéry, and B. Crippa. Persistent Scatterer Interferometry: A review. *ISPRS Journal of Photogrammetry and Remote Sensing*, 115:78–89, 2016. doi: 10.1016/j.isprsjprs.2015.10.011.

CSC Mission Management Team. Sentinel-1 High Level Operations Plan (HLOP). Technical note Copernicus Space Component (CSC) Mission Management, Doc. COPE-S1OP-EOPG-PL-15-0020, Iss. 2, Rev. 2, Date 29.03.2018, Available: https://sentinel.esa.int/web/sentinel/user-guides/document-library, 2018.

I. G. Cumming and F. H. Wong. *Digital Processing of Synthetic Aperture Radar Data.* Artech House, 2005.

J. C. Curlander. Location of Spaceborne SAR Imagery. *IEEE Transactions on Geoscience and Remote Sensing*, GE-20(3):359–364, 1982. doi: 10.1109/TGRS.1982.350455.

J. C. Curlander and R. N. McDonough. *Synthetic Aperture Radar: Systems and Signal Processing.* John Wiley & Sons, Inc, 1991.

R. Dach, S. Schaer, D. Arnold, L. Prange, D. Sidorov, P. Strebler, A. Villiger, and A. Jäggi. CODE final product series for the IGS. Astronomical Institute, University of Bern, 2018.

J. Davis, T. Herring, I. Shapiro, A. Rogers, and G. Elgered. Geodesy by radio interferometry: Effects of atmospheric modeling errors on estimates of baseline length. *Radio Science*, 20(6):1593–1607, 1985.

F. de Zan and A. M. Guarnieri. TOPSAR: Terrain Observation by Progressive Scans. *IEEE Transactions on Geoscience and Remote Sensing*, 44(9):2352–2360, 2006. doi: 10.1109/TGRS.2006.873853.

P. Dheenathayalan, D. Small, A. Schubert, and R. F. Hanssen. High-precision positioning of radar scatteres. *Journal of Geodesy*, 90(5):403–422, 2016. doi: 10.1007/s00190-015-0883-4.

W. R. Dick and D. Thaller, editors. *IERS Annual Report 2016.* Verlag des Bundesamts für Kartographie und Geodäsie. Available: www.iers.org/IERS/EN/Publications/publications.html, 2016.

A. W. Doerry. Reflectors for SAR Performance Testing. Sandia Report, SAND2008-0396, Sandia National Laboratories, Available: http://www.sandia.gov/radar/publications, 2008.

Y. Dong, L. Zhang, T. Balz, H. Luo, and M. Liao. Radargrammetric DSM generation in mountainous aeas through adaptive-window least squares matching constrained by enhanced epipolar geometry. *ISPRS Journal of Photogrammetry and Remote Sensing*, 137:61–72, 2018. doi: 10.1016/j.isprsjprs.2018.01.010.

I. J. Dowman. The geometry of SAR images for geocoding and stereo applications. *International Journal of Remote Sensing*, 13(9):1609–1617, 1992. doi: 10.1080/01431169208904215.

G. Duchossois and R. Zobl, editors. *ERS-2: A Continuation of the ERS-1 Success*. ESA bulletin 83a, Available: https://earth.esa.int/documents/10174/1598482/ESABULL83A.pdf, 1995.

M. Eineder, C. Minet, P. Steigenberger, X. Cong, and T. Fritz. Imaging geodesy - Toward centimeter-level ranging accuracy with TerraSAR-X. *IEEE Transactions on Geoscience and Remote Sensing*, 49(2):661–671, 2011. doi: 10.1109/TGRS.2010.2060264.

A. Einstein. Über das Relativitätsprinzip und die aus demselben gezogenen Folgerungen. Jahrbuch der Radioaktivität und Elektronik 4, 1907.

L. Essen and K. D. Froome. The Refractive Indices and Dielectric Constants of Air and its Principal Constituents at 24,000 Mc/s. *Proceedings of the Physical Society*, 64(10):862–875, 1951.

T. G. Farr, A. Rosen, P, E. Caro, R. Crippen, R. Duren, S. Hensley, M. Kobrick, M. Paller, E. Rodriguez, L. Roth, D. Seal, S. Shaffer, and J. Shimada. The Shuttle Radar Topography Mission. *Reviews of Geophysics*, 45, 2007. doi: 10.1029/2005RG000183.

A. Ferretti, C. Prati, and F. Rocca. Permanent Scatterers in SAR Interferometry . *IEEE Transactions on Geoscience and Remote Sensing*, 39(1):8–20, 2001. doi: 10.1109/36.898661.

A. L. Fey, D. Gordon, and C. S. Jacobs, editors. *The Second Realization of the International Celestial Reference Frame by Very Long Baseline Interferometry*. Verlag des Bundesamts für Kartographie und Geodäsie.
Available: www.iers.org/IERS/EN/Publications/TechnicalNotes/TechnicalNotes.html, 2009.

A. Freeman. SAR Calibration: An Overview. *IEEE Transactions on Geoscience and Remote Sensing*, 30(6):1107–1121, 1992. doi: 10.1109/36.193786.

T. Fritz and M. Eineder. TerraSAR-X Ground Segment Basic Product Specification Document. DLR Technical Note, Doc. TX-GS-DD-3302, Iss. 1.9, Date 09.10.2013, Available: https://tandemx-science.dlr.de/, 2013.

T. Fritz, J. Mittermayer, B. Schättler, W. Balzer, S. Buckreuß, and R. Werninghaus. TerraSAR-X Ground Segment Level 1b Product Format Specification. DLR Technical Note, Doc. TX-GS-DD-3302, Iss. 1.3, Date 10.12.2007, Available: https://sss.terrasar-x.dlr.de/, 2007.

M. C. Garthwaite. On the Design of Radar Corner Reflectors for Deformation Monitoring in Multi-Frequency InSAR. *Remote Sensing*, 9(648):1–23, 2017. doi: doi:10.3390/rs9070648.

C. Gisinger. Atmospheric corrections for TerraSAR-X derived from GNSS observations. M.S. Thesis, Technical University of Munich, Munich, Germany, 2012.

G. Gomba, A. Parizzi, F. de Zan, M. Eineder, and R. Bamler. Toward Operational Compensation of Ionospheric Effects in SAR Interferograms: The Split-Spectrum Method. *IEEE Transactions on Geoscience and Remote Sensing*, 54(3):1446–1461, 2016. doi: 10.1109/TGRS.2015.2481079.

G. Gomba, F. González, and F. de Zan. Ionospheric Phase Screen Compensation for the Sentinel-1 TOPS and ALOS-2 ScanSAR Modes. *IEEE Transactions on Geoscience and Remote Sensing*, 55 (1):223–235, 2017. doi: 10.1109/TGRS.2016.2604461.

S. Hackel, O. Montenbruck, P. Steigenberger, U. Balss, C. Gisinger, and M. Eineder. Model improvements and validation of TerraSAR-X precise orbit determination. *Journal of Geodesy*, 91:547–562, 2017. doi: DOI10.1007/s00190-016-0982-x.

M. Hernández-Pajares, J. M. Juan, J. Sanz, R. Orus, A. Garcia-Rigo, J. Feltens, A. Komjathy, S. C. Schaer, and A. Krankowski. The IGS VTEC maps: a reliable source of ionospheric information since 1998. *Journal of Geodesy*, 83(3-4):263, 2009. doi: 10.1007/s00190-008-0266-1.

T. Hobiger, Y. Kinoshita, S. Shimizu, R. Ichikawa, M. Furuya, T. Kondo, and Y. Koyama. On the importance of accurately ray-traced troposphere corrections for Interferometric SAR data. *Journal of Geodesy*, 84(9):537–546, 2010. doi: 10.1007/s00190-010-0393-3.

B. Hofmann-Wellenhof, H. Lichtenegger, and E. Wasle. *GNSS Global Navigation Satellite Systems*. Springer Wien NewYork, 2008.

R. L. Jordan. The Seasat-A Synthetic Aperture Radar System. *IEEE Journal of Oceanic Engineering*, OE-5(2):154–164, 1980. doi: 10.1109/JOE.1980.1145451.

R. Kahle. TerraSAR-X / TanDEM-X Mission Operations Segment Orbit and Attitude Product Specification. DLR Technical Note, Doc. TX-GS-SP-2601, Iss. 3.4, Date 06.11.2012, 2012.

M. Kobrick, F. W. Leberl, and J. Raggam. Radar Stereo Mapping with Crossing Flight Lines. *Canadian Journal of Remote Sensing*, 12(2):132–148, 1986. doi: 10.1080/07038992.1986.10855105.

K. R. Koch. *Parameter Estimation and Hypotheses Testing in Linear Models*. Springer-Verlag: Berlin Heidelberg, Germany, 1999.

K. R. Koch and J. Kusche. Regularization of geopotential determination from satellite data by variance components . *Journal of Geodesy*, 76:259–268, 2002. doi: 10.1007/s00190-002-0245-x.

J. Kodet, Schreiber K. U., J. Eckl, C. Plötz, S. Mähler, T. Schüler, T. Klügel, and S. Riepl. Colocation of space geodetic techniques carried out at the Geodetic Observatory Wettzell using a closure in time and a multi-technique reference target. *Journal of Geodesy*, 92(9):1097–1112, 2018. doi: 10.1007/s00190-017-1105-z.

W. Koppe, R. Wenzel, S. Henning, J. Janoth, P. Hummel, and H. Raggam. Quality Assessment of TerraSAR-X derived Ground Control Points. *Proceedings of IGARSS'12 Conference, July 22–27, Munich, Germany*, pages 3580–3583, 2012. doi: 10.1109/IGARSS.2012.6350643.

J. Kouba. Implementation and testing of the gridded Vienna Mapping Function 1 (VMF1). *Journal of Geodesy*, 82(4-5):193–205, 2007. doi: 10.1007/s00190-007-0170-0.

J. Kouba, F. Lahaye, and P. Tétreault. *Precise Point Positioning*, pages 723–751. in Springer Handbook of Global Navigation Satellite Systems, Teunissen, P. J. G. and Montenbruck, O. (Editors), Springer International Publishing AG, 2017. doi: 10.1007/978-3-319-42928-1.

G. Krieger, A. Moreira, H. Fiedler, I. Hajnsek, M. Werner, M. Younis, and M. Zink. TanDEM-X: A Satellite Formation for High-Resolution SAR Interferometry. *IEEE Transactions on Geoscience and Remote Sensing*, 45(11):3317–3341, 2007. doi: 10.1109/TGRS.2007.900693.

A. Kult. ASAR PRODUCTS SPECIFICATIONS. ESA & MDA Technical Note, Doc. PO-RS-MDA-GS-2009, Iss. 4, Rev. C, Date 20.01.2012, Available: https://earth.esa.int/web/guest/document-library/, 2012.

D. Landskron and J. Böhm. VMF3/GPT3: refined discrete and empirical troposphere mapping functions. *Journal of Geodesy*, 92(4):349–360, 2018. doi: 10.1007/s00190-017-1066-2.

T. R. Lauknes. Rockslide Mapping in Norway by Means of Interferometric SAR Time Series Analysis. PHD Thesis, University of Tromsø, Department of Physics and Technology, 2010.

F. W. Leberl. *Radargrammetric image processing.* Artech House, 1990.

D. De Lisle, S. Iris, E. Arsenault, J. Smyth, and G. Kroupnik. RADARSAT Constellation Mission Status Update. In *Proceedings of EUSAR 2018 Conference, June 04-07, Aachen, Germany*, pages 300–305, 2018.

J. Liu, B. Han, C. Ding, D. Meng, and F. Li. The preliminary results about positioning accuracy of gf-3 sar satellite system. In *Proceedings of IGARSS'17 Conference, July 23–28, Fort Worth, TX, USA*, pages 6087–6089, 2017. doi: 10.1109/IGARSS.2017.8128398.

J. Louet. The Envisat Mission and System. ESA bulletin 106,
Available: http://www.esa.int/esapub/bulletin/bullet106/bul106_1.pdf, 2001.

F. Lyard, F. Lefevre, T. Letellier, and O. Francis. Modelling the global ocean tides: modern insights from FES2004. *Journal of Geophysical Research*, 56:394–415, 2006. doi: 10.1007/s10236-006-0086-x.

P. S. Mahapatra, S. Samiei-Esfahany, H. van der Marel, and R. F. Hanssen. On the Use of Transponders as Coherent Radar Targets for SAR Interferometry. *IEEE Transactions on Geoscience and Remote Sensing*, 52(3):1869–1878, 2014. doi: 10.1109/TGRS.2013.2255881.

P. S. Mahapatra, H. van der Marel, F. van Leijen, S. Samiei-Esfahany, R. Klees, and R. F. Hanssen. InSAR datum connection using GNSS-augmented radar transponders. *Journal of Geodesy*, 92(1): 21–32, 2017. doi: 10.1007/s00190-017-1041-y.

A. J. Mannucci, B. D. Wilson, D. N. Yuan, C. H. Ho, U. J. Lindqwister, and T. F. Runge. A global mapping technique for GPS-derived ionospheric total electron content. *Radio Science*, 33(3): 565–582, 1998. doi: 10.1029/97RS02707.

MDA. RADARSAT-2 PRODUCT DESCRIPTION. MacDonald, Dettwiler and Associates (MDA), MDA Technical Note, Doc. RN-SP-52-1238, Iss. 1/13, Date 21.03.2016, Available: https://mdacorporation.com/geospatial/international/satellites/RADARSAT-2, 2016.

V. B. Mendes and E. C. Pavlis. High-accuracy zenith delay prediction at optical wavelengths. *Geophysical Research Letters*, 31(14), 2004. doi: 10.1029/2004GL020308.

E. M. Mikhail and F. Ackermann. *Observations and Least Squares.* IEP–Dun-Donnelley, Harper and Row, 1976.

J. J. Mohr and S. N. Madsen. Geometric Calibration of ERS Satellite SAR Images. *IEEE Transactions Geoscience and Remote Sensing*, 39(4):842–850, 2001. doi: 10.1109/36.917909.

S. Montazeri, C. Gisinger, and X. X. Eineder, M. Zhu. Automatic Detection and Positioning of Ground Control Points Using TerraSAR-X Multiaspect Acquisitions. *IEEE Transactions on Geoscience and Remote Sensing*, 56(5):2613–2632, 2018. doi: 10.1109/TGRS.2017.2769078.

O. Montenbruck, M. Wermuth, and R. Kahle. GPS Bbased Relative Navigation for the TanDEM-X Mission - First Flight Results. *Journal of The Institute of Navigation*, 58(4):293–304, 2011. doi: 10.1007/s00190-016-0982-x.

T. Nilsson, J. Böhm, D. D. Wijaya, A. Tresch, V. Nafisi, and H. Schuh. *Path Delays in the Neutral Atmosphere*, pages 73–136. in Atmospheric Effects in Space Geodesy, Böhm, J. and Schuh, H. (Editors), Springer-Verlag Berlin Heidelberg, 2013. doi: 10.1007/978-3-642-36932-2_3.

D. O. Nitti, R. Nutricato, R. Lorusso, N. Lombardi, F. Bovenga, M. F. Bruno, M. T. Chiaradia, and G. Milillo. On the geolocation accuracy of COSMO-SkyMed products. *Proceedings of SPIE*, 9642 (96420D):1–12, 2015. doi: 10.1117/12.2196870.

D. O. Nitti, A. Morea, R. Nutricato, M. T. Chiaradia, C. Mantia, L. Agrimano, and S. Samarelli. Automatic GPC extraction with High Resolution COSMO-SkyMed products. *Proceedings of SPIE*, 10003(1000302):1–12, 2016. doi: doi:10.1117/12.2241281.

C. Noll and M. Pearlman, editors. *International Laser Ranging Service 2009-2010 Report*. Goddard Space Flight Center, Greenbelt, MD 20771, 2012.

H. Peter, A. Jäggi, J. Fernández, D. Escobar, F. Ayuga, D. Arnold, M. Wermuth, S. Hackel, M. Otten, W. Simons, P. N. A. M. Visser, U. Hugentobler, and P. Féménias. Sentinel-1A - First precise orbit determination results. *Advances in Space Research*, 60(5):879–892, 2017. doi: 10.1016/j.asr.2017.05.034.

G. Petit and B. Luzum, editors. *IERS Conventions (2010)*. Verlag des Bundesamts für Kartographie und Geodäsie. Available: http://tai.bipm.org/iers/conv2010/conv2010.html, 2010.

L. Petrov and J. P. Boy. Study of the atmospheric pressure loading signal in very long baseline interferometry observations. *Journal of Geophysical Research*, 109(B03405), 2004. doi: 10.1029/2003JB002500.

R. Piantanida. Sentinel-1 Detailed Algorithm Definition. Technical note by Sentinel-1 Mission Performance Center (MPC), Doc. DI-MPC-IPFDPM, Iss. 2, Rev. 1, Date 31.01.2017, Available: https://sentinel.esa.int/web/sentinel/user-guides/document-library, 2017.

J. C. Poyard. IGN best practice for surveying instrument reference points at ITRF co-location sites. Technical report, 2017.

H. Raggam, K. Gutjahr, R. Perko, and M. Schardt. Assessment of the Stereo-Radargrammetric Mapping Potential of TerraSAR-X Multibeam Spotlight Data . *IEEE Transactions on Geoscience and Remote Sensing*, 48(2):971–977, 2010a.

H. Raggam, R. Perko, K. Gutjahr, N. Kiefl, W. Koppe, and S. Henning. Accuracy Assessment of 3D Point Retrieval from TerraSAR-X Data Sets. In *Proceedings of EUSAR 2010 Conference, June 07-10, Aachen, Germany*, pages 572–575, 2010b.

M. Rodriguez-Cassola, P. Prats, F. de Zan, R. Scheiber, C. Reigber, D. Geudtner, and A. Moreira. Doppler-Related Distortions in TOPS SAR Images. *IEEE Transactions on Geoscience and Remote Sensing*, 53(1):25–35, 2015. doi: 10.1109/TGRS.2014.2313068.

B. Rosich and P. Meadows. Absolute Calibration of ASAR Level 1 Products Generated with PF-ASAR. Technical Note, ESA, Doc. ENVI-CLVL-EOPG-TN-03-0010, Iss. 1, Rev. 5, Date 07.10.2004, Available: https://earth.esa.int/web/guest/document-library/, 2004.

J. Saastamoinen. Contributions to the theory of atmospheric refraction Part II. Refraction corrections in satellite geodesy. *Bulletin Géodésique*, 107(1):13–34, 1973.

S. Schaer. *Mapping and Predicting the Earth's Ionosphere using the Global Positioning System.* Geodaetisch-geophysikalische Arbeiten in der Schweiz, vol. 59. Schweizerische Geodaetische Kommission. Available: http://www.sgc.ethz.ch/publications, 1999.

A. Schubert, M. Jehle, D. Small, and E. Meier. Influence of Atmospheric Path Delay on the Absolute Geolocation Accuracy of TerraSAR-X High-Resolution Products. *IEEE Transactions on Geoscience and Remote Sensing*, 48(2):751–758, 2010. doi: 10.1109/TGRS.2009.2036252.

A. Schubert, M. Jehle, D. Small, and E. Meier. Mitigation of atmospheric perturbations and solid Earth movements in a TerraSAR-X time-series. *Journal of Geodesy*, 86(4):257–270, 2012a. doi: 10.1007/s00190-011-0515-6.

A. Schubert, D. Small, M. Jehle, and E. Meier. COSMO-SkyMed, TerraSAR-X, and Radarsat-2 Geolocation Accuracy after Compensation for Earth-System Effects. *Proceedings of IGARSS'12 Conference, July 22–27, Munich, Germany*, pages 3301–3304, 2012b. doi: 10.1109/IGARSS.2012.6350598.

A. Schubert, D. Small, N. Miranda, D. Geudtner, and E. Meier. Sentinel-1A Product Geolocation Accuracy: Commissioning Phase Results. *Remote Sensing*, 7:9431–9449, 2015. doi: 10.3390/rs70709431.

A. Schubert, N. Miranda, D. Geudtner, and D. Small. Sentinel-1A/B Combined Product Geolocation Accuracy. *Remote Sensing*, 9(607), 2017. doi: doi:10.3390/rs9060607.

H. Schuh and J. Böhm. *Very Long Baseline Interferometry for Geodey and Astrometry*, pages 339–376. in Sciences for Geodesy II, Xu, G. (Editor), Springer Berlin Heidelberg, 2013. doi: 10.1007/978-3-642-28000-9_7.

M. Schwerdt, B. Bräutigam, M. Bachmann, B. Döring, D. Schrank, and J. H. Gonzalez. Final TerraSAR-X Calibration Results Based on Novel Efficient Methods. *IEEE Transactions on Geoscience and Remote Sensing*, 48(2):677–689, 2010. doi: 10.1109/TGRS.2009.2035308.

M. Shimada, O. Isoguchi, T. Tadono, and K. Isono. PALSAR Radiometric and Geometric Calibration. *IEEE T. Geoscience and Remote Sensing*, 47(12):3915–3932, 2009. doi: 10.1109/TGRS.2009.2023909.

D. Small, B. Rosich, A. Schubert, E. Meier, and D. Nüesch. GEOMETRIC VALIDATION OF LOW AND HIGH-RESOLUTION ASAR IMAGERY. In *Proceedings of the 2004 Envisat & ERS Symposium, September 06–10, Salzburg, Austria*, 2004.

D. E. Smith and Dunn P. J. Long term evolution of the Lageos Orbit. *Geophysical Research Letters*, 76(6):437–440, 1980. doi: 10.1029/GL007i006p00437.

F. Spataro, P. Pavia, S. Barrasso, R. Roscigno, F. Sabbioni, R. Torres, S. Lokas, S. Osborne, P. Snoeij, and D. Geudtner. Sentinel-1C&D System. In *Proceedings of EUSAR 2018 Conference, June 04-07, Aachen, Germany*, pages 646–650, 2018.

S. Stein. Algorithms for Ambiguity Function Processing. *IEEE Transactions on Acoustics, Speech, and Signal Processing*, ASSP-29(3):588–599, 1981.

R. H. Stewart. Seasat: Results of the Mission. *Bulletin American Meteorological Society (BAMS)*, 69 (12):1441–1447, 1988. doi: 10.1175/1520-0477(1988)069⟨1441:SROTM⟩2.0.CO;2.

S. Suzuki, Y. Osawa, Y. Hatooka, Y. Kankaku, and T. Watanabe. Overview of Japan's Advanced Land Observing Satellite-2 mission. In *Proceedings of SPIE 7474, August 31 – September 3, Berlin, Germany*, 2009. doi: 10.1117/12.831340.

S. Sverva, C. Fiorentino, and F. Cavello. The cosmo-skymed seconda generazione key improvements to respond to the user community needs. In *Proceedings of IGARSS'15 Conference, July 26–31, Milan, Italy*, pages 219–222, 2015. doi: 10.1109/IGARSS.2015.7325739.

P. J. G. Teunissen and O. Montenbruck, editors. *Springer Handbook of Global Navigation Satellite Systems*. Springer International Publishing AG, 2017. doi: 10.1007/978-3-319-42928-1.

R. Torres, P. Snoeij, D. Geudtner, D. Bibby, M. Davidson, E. Attema, P. Potin, B. Rommen, N. Floury, M. Brown, I. N. Traver, P. Deghaye, B. Duesmann, B. Rosich, N. Miranda, C. Bruno, M. L'Abbate, R. Croci, A. Pietropaolo, M. Huchler, and F. Rostan. GMES Sentinel-1 mission. *Remote Sensing of Environment*, 120:9–24, 2012. doi: 10.1016/j.rse.2011.05.028.

T. Toutin and R. Chénier. 3-D Radargrammetric Modeling of RADARSAT-2 Ultrafine Mode: Preliminary Results of the Geometric Calibration. *IEEE Geoscience and Remote Sensing Letters*, 6(3): 611–615, 2009. doi: 10.1109/LGRS.2009.2024391.

F. T. Ulaby and M. C. Dodson. *Handbook of radar scattering statistics for terrain*. Artech House, 1989.

P. W. L. van Barneveld, O. Montenbruck, and P. N. A. M. Visser. Epochwise prediction of GPS single differenced ionospheric delays of formation flying spacecraft. *Advances in Space Research*, 44: 987–1001, 2009. doi: 10.1016/j.asr.2009.07.006.

M. Villano, G. Krieger, and A. Moreira. Staggered SAR: High-Resolution Wide-Swath Imaging by Continuous PRI Variation. *IEEE Transactions on Geoscience and Remote Sensing*, 52(7):4462–4479, 2014. doi: 10.1109/TGRS.2013.2282192.

A. Villiger and R. Dach, editors. *International GNSS Service Technical Report 2017*. IGS Central Bureau and University of Bern; Bern Open Publishing, 2018. doi: 10.7892/boris.116377.

R. Werninghaus and S. Buckreuss. The TerraSAR-X Mission and System Design. *IEEE Transactions on Geoscience and Remote Sensing*, 48(2):606–614, 2010. doi: 10.1109/TGRS.2009.2031062.

B. Wessel. TanDEM-X Ground Segment DEM Products Specification Document. DLR Technical Note, Doc. TD-GS-PS-0021, Iss. 3.2, Date 07.05.2018, Available: https://tandemx-science.dlr.de/, 2018.

M. Wilkinson, U. Schreiber, I. Procházka, C. Morre, J. Degnan, G. Kirchner, Z. Zhongping, P. Dunn, V. Shargorodskiy, M. Sadovnikov, C. Courde, and H. Kunimori. The next generation of satellite laser ranging systems. *Journal of Geodesy*, Online First, 2018. doi: 10.1007/s00190-018-1196-1.

Y. Yoon, M. Eineder, N. Yague-Martinez, and O. Montenbruck. TerraSAR-X Precise Trajectory Estimation and Quality Assessment. *IEEE Transactions on Geoscience and Remote Sensing*, 47(6): 1859–1868, 2009. doi: 10.1109/TGRS.2008.2006983.

X. X. Zhu and R. Bamler. Tomographic sar inversion byl_1-norm regularization—the compressive sensing approach. *IEEE Transactions on Geoscience and Remote Sensing*, 48(10):3839–3846, 2010. doi: 10.1109/TGRS.2010.2048117.

J. F. Zumberge, M. B. Heflin, D. C. Jeffereson, M. M. Watkins, and F. H. Webb. Precise point positioning for the efficient and robust analysis of GPS data from large networks. *Journal of Geophysical Research*, 102(B3):5005–5017, 1997.

F. Zus, D. Galin, J. Dousa, and J. Wickert. Systematic errors of mapping functions which are based on the VMF1 concept. *GPS Solutions*, 19(2):277–286, 2015.